2016

Design and modification of cathode materials for high-performance lithium-sulfur and lithium-selenium batteries

Hongqiang Wang
University of Wollongong

UNIVERSITY OF WOLLONGONG

Design and Modification of Cathode Materials for High-Performance Lithium-Sulfur and Lithium-Selenium Batteries

This thesis is presented as part of the requirements for the

Award of the Degree of

Doctor of Philosophy

from the

University of Wollongong

by

Hongqiang Wang, B. Eng., M. Eng.

Department of Institute for Superconducting and Electronic Materials,

Faculty of Engineering and Information Sciences

March 2016

CERTIFICATION

I, Hongqiang Wang, declare that this thesis, submitted in fulfilment of the requirements for the award of Doctor of Philosophy, in the Institute for Superconducting & Electronic Materials, Faculty of Engineering and Information Science, University of Wollongong, is wholly my own work unless otherwise referenced or acknowledged. This document has not been submitted for qualifications at any other academic institution.

Hongqiang Wang

March 2016

DEDICATION

To my lovely wife, and parents, who have always been there when I needed them.

ACKNOWLEGEMENTS

I would like to take this opportunity to express my utmost gratitude to my supervisor, Prof. Zaiping Guo, for her academic guidance, invaluable advice, and constant encouragement and understanding throughout the whole course of my research and study. I also wish to thank Prof. Hua Kun Liu for her guidance and supervision. I would like to offer my special thanks to Dr. Tania Silver, who always helped to do the critical reading on my manuscripts and thesis.

I would also like to thank the Australian government and the University of Wollongong for my awards of an International Postgraduate Research Scholarship and Australian Postgraduate Awards.

I also would like to express my thanks to my former and present colleagues during my PhD study at ISEM for sharing their knowledge and for helpful discussion with me, creating an excellent working environment. These include Dr. Peng Zhang, Dr. Chaofeng Zhang, Dr. Jianfeng Mao, Dr. Sha Li, Dr. Dan Li, Dr. Qing Meng, Dr. Li Li, Dr. Shudi Min, Dr. Yunxiao Wang, Mr. Kan Huang, Mr. Ruixiang Yu, Mr. Wenchao Zhang, Mr. Tengfei Zhou, Mr. Sujith Kalluri, Ms. Hong Gao, and Ms. Qing Zhang. Also, many thanks are extended to a number of staff members in the University of Wollongong for their valuable assistance. These include Dr. Zhixin Chen and Dr. Gilberto Casillas-Garcia (TEM), Dr. Kosta Konstantinov (TGA), Dr. Dongqi Shi (XPS), Dr. Tony Romeo (FESEM), Dr. Germanas Peleckis (XRD), Ms. Jinyan Xiong (UV-Vis), Ms. Yajie Liu (Raman), Ms. Joanne George (Laboratory and Safety

Operation Officer), Mrs. Crystal Mahfouz, and Mrs. Narelle Badger (Administrative Assistant).

Finally, I would like to express my deep appreciation and love to my family, including my parents, my brother, and my nephew for their understanding and support. My special thanks to my wonderful wife, Yingying Song, who has always been understanding and encouraging during my difficult times.

ABSTRACT

Lithium-sulfur (Li-S) batteries have been considered as most promising candidates for the next generation lithium-ion batteries, as sulfur features high theoretical capacity (1675 mAh g^{-1}), high specific energy density (2600 Wh kg^{-1}), cost effectiveness, and nontoxicity. However, the broad application of Li-S batteries is limited by several persistent problems, such as the low electrical conductivity of sulfur and its discharge product, the high solubility and diffusivity of polysulfide intermediates in organic electrolytes, and the related side reaction "shuttle effect", as well as large volume change caused by the intercalation of Li into the sulfur. Therefore, improving the conductivity of the sulfur cathode, enhancing the tolerance for volume change, maintaining the soluble polysulfides within the cathode region, and limiting polysulfide diffusion are the key points for the development of Li-S batteries. In this doctoral work, a series of nanostructured sulfur-based materials were prepared for Li-S batteries, including TiO_2-coated hierarchically ordered porous sulfur composite, porous carbon-sulfur composite derived from cotton, and ordered mesoporous-carbon-fiber–sulfur cathode material, as well as a novel design for an integrated flexible sulfur cathode for Li-S batteries. On the other hand, selenium, as a congener of sulfur, possesses similar chemical behaviour and could react with lithium to form selenides. The theoretical volumetric capacity of selenium (3253 mAh cm^{-3}) is comparable to that of sulfur (3467 mAh cm^{-3}). A novel type of one-dimensional organic selenium-containing fiber was synthesized for lithium-selenium (Li-Se) and sodium-selenium (Na-Se) batteries.

A three-dimensional (3D) hierarchically ordered mesoporous carbon-sulfur composite coated with a thin TiO_2 layer has been synthesized by a low-cost process and investigated as a cathode for Li-S batteries. The TiO_2-coated carbon-sulfur composite works as a suitable cathode material for lithium-sulfur batteries. The hierarchical architecture provides a 3D conductive network for electron transfer, open channels for ion diffusion, and strong confinement of soluble polysulfides. Meanwhile, the TiO_2 coating layer could further effectively prevent the dissolution of polysulfides and also improve the strength of the entire electrode, thereby enhancing the electrochemical performance. As a result, after TiO_2 coating, the electrode demonstrates excellent cycling performance, with a discharge capacity of 608 mAh g^{-1} at the 0.2 C current rate and 500 mAh g^{-1} at the 1 C current rate after 120 cycles, respectively.

A new type of low-cost activated micro-macroporous carbon suitable for mass production that is derived from cotton was successfully prepared by using potassium hydrate in a chemical activation method. The activated carbon exhibits a hierarchically porous microstructure and high specific surface area (989 m^2 g^{-1}). The micro-macroporous structure allows a large amount of sulfur (68%) to be infiltrated into the micropores of the host. This unique micro-macroporous structure is found to be directly related to the battery performance. The macroporous structure of this carbon provides channels for sulfur to be loaded into the micropores and enhances fast transport of electrons/ions and electrolyte, while the microporous structure can trap elemental S and lithium polysulfides during cycling. When evaluated as a cathode for lithium-sulfur batteries, the hierarchically porous carbon-sulfur composite

electrode exhibits excellent cycling stability and good performance. The resulting composite electrode possesses a reversible capacity of 760 mAh g^{-1} after 200 cycles at current density of 0.2 C.

One-dimensional ordered mesoporous carbon fiber has been prepared via the electrospinning technique, using resol as the carbon source and triblock copolymer Pluronic F127 as the template. Sulfur is then encapsulated in these ordered mesoporous carbon fibers by a simple thermal treatment. The interwoven fibrous nanostructure has favourable mechanical stability and can provide an effective conductive network for sulfur and polysulfides during cycling. The ordered mesopores can also restrain the diffusion of long-chain polysulfides. All these features lead to excellent electrochemical performance. The ordered mesoporous-carbon-fiber -sulfur (OMCF-S) composite with 63% S exhibits high reversible capacity, good capacity retention, and enhanced rate capacity when used as cathode in rechargeable lithium-sulfur batteries. The OMCF-S electrode maintains a stable discharge capacity of 690 mAh g^{-1} at 0.3 C, even after 300 cycles. In particular, the OMCF can be mass produced in a simple way at low cost, which makes our sulfur-based electrode highly promising for practical application in lithium-sulfur batteries.

A strategy for configuration of an integrated sulfur cathode is presented, which is composed of an integrated carbon/sulfur/carbon sandwich structure on polypropylene separator that is produced via the simple doctor blade technique. The integrated electrode exhibits excellent flexibility and high mechanical strength. The top and bottom carbon layers of the sandwich-structured electrode not only work as double

current collectors, which effectively improve the conductivity of the electrode, but also serve as good barriers to suppress the diffusion of the polysulfides and buffer the volume expansion of the active materials, leading to suppression of the shuttle effect and low self-discharge behaviour. The integrated sulfur cathode delivered a high reversible capacity of 730 mAh g^{-1} over 500 cycles, with capacity decay as small as 0.058% per cycle and a low self-discharge constant of 0.0293 per week.

Organic selenide fibers composed of carbonized polyacrylonitrile/selenium (CPAN/Se) have been synthesized by heating polyacrylonitrile-selenium (PAN-Se) fibers via the electrospinning technique at 600 ^{o}C. The Se molecules are confined by N-containing carbon ring structures in the form of energy-storing selenium side chains in the carbonized PAN matrix. This unique stable chemical structure with a conductive carbon skeleton connected to the selenium side chains and excellent mechanical stability can allow the CPAN/Se composite cathodes to be charged and discharged in a low-cost carbonate-based electrolyte with excellent long cycling stability and quite good rate performance. The superior electrochemical performance of the CPAN/Se electrodes has been demonstrated in both lithium-ion and sodium-ion batteries, where it has delivered a high capacity of nearly 600 mAh g^{-1} for 500 cycles in lithium-selenium (Li-Se) batteries and 410 mAh g^{-1} for 300 cycles in sodium-selenium (Na-Se) batteries at 0.3 C.

TABLE OF CONTENTS

LIST OF PUBLICATIONS

1. **Hongqiang Wang**, Wenchao Zhang, Huakun Liu, Zaiping Guo, A strategy for configuration of an integrated flexible sulfur cathode for high-performance lithium-sulfur batteries, Angewandte Chemie International Edition, 2016, 55, 3992-3996.

2. **Hongqiang Wang**, Chaofeng Zhang, Zhixin Chen, Hua Kun Liu, Zaiping Guo, Large-scale synthesis of ordered mesoporous carbon fiber and its application as cathode material for lithium-sulfur batteries, Carbon, 2015, 81, 782-787.

3. **Hongqiang Wang**, Sha Li, Dan Li, Zhixin Chen, Hua Kun Liu, Zaiping Guo, TiO_2 coated three-dimensional hierarchically ordered porous sulfur electrode for the lithium/sulfur rechargeable batteries, Energy, 2014, 75, 597-602.

4. **Hongqiang Wang**, Sha Li, Zhixin Chen, Hua Kun Liu, Zaiping Guo, A novel type of one-dimensional organic selenium-containing fiber with superior performance for lithium-selenium and sodium-selenium batteries, RSC Advances, 2014, 4, 61673-61678.

5. **Hongqiang Wang**, Zhixin Chen, Hua Kun Liu, Zaiping Guo, A facile synthesis approach to micro-macroporous carbon from cotton and its application in the lithium-sulfur battery, RSC Advances, 2014, 4, 65074-65080.

6. Xi Lin*, **Hongqiang Wang***(co-first author), Haiwei Du, Xinrui Xiong, Bo Qu, Zaiping Guo, Dewei Chu, Growth of lithium lanthanum titanate nanosheets and their application in lithium ions batteries, ACS Applied Materials & Interfaces, 2016, 8, 1486-1492.

7. Mohammad Ihsan*, **Hongqiang Wang*** (co-first author), Siti R. Majid, Jianping Yang, Shane J. Kennedy, Zaiping Guo, Hua Kun Liu, $MoO_2/Mo_2C/C$ spheres as anode materials for lithium ion batteries, Carbon, 2016, 96, 1200-1207.

8. Dan Li, **Hongqiang Wang**, Huakun Liu, Zaiping Guo, A new strategy for achieving a high performance anode for lithium ion batteries-encapsulating germanium nanoparticles in carbon nanoboxes, Advanced Energy Materials, 2016, 6, 1501666.

9. Ihsan Mohammad, Qing Meng, Li Li, Dan Li, **Hongqiang Wang**, Kuok Hau Seng, Zhixin Chen, Shane Kennedy, Zaiping Guo, Huakun Liu, V_2O_5/mesoporous carbon composite as a cathode materials for lithium-ion batteries. Electrochimica Acta, 2015, 173, 172-177.

10. Shudi Min, Chongjun Zhao, Peiwen Ju, Tengfei Zhou, Hong Gao, Yang Zheng, **Hongqiang Wang**, Guorong Chen, Xiuzhen Qian, Zaiping Guo, Facile synthesis of nickel-foam-based nano-architectural composite as binder-free anodes for high capacity Li-ion batteries. J Power Sources, 2016, 304, 311-318.

LIST OF FIGURES

LIST OF TABLE

NOMENCLATURE

List of Abbreviations

Abbreviation	Full name
Li-S	Lithium-sulfur
Li-Se	Aluminium foil
Na-Se	Sodium-selenium
PVDF	Polyvinylidene difluoride
NMP	1-methyl-2-pyrrolidinone
3D	Three dimensional
1D	One dimensional
EC	Ethylene carbonate
DEC	Diethyl carbonate
DOL	1,3-dioxolane
DME	Dimethoxyethane
DMF	N,N-Dimethylformamide
PAN	Polyacrylonitrile
PVB	Polyvinyl butyral
PP	Polypropylene
SEM	Scanning electron microscopy
TEM	Transmission electron microscopy
HRTEM	High-resolution transmission electron microscopy

SAED	Selected area electron diffraction
XRD	X-ray diffraction
TGA	Thermogravimetric Analysis
BET	Brunauer Emmett Teller
FTIR	Fourier Transform Infrared Spectroscopy
UV-Vis	Ultraviolet-visible spectroscopy
XPS	X-ray photoelectron spectroscopy
EIS	Electrochemical Impedance Spectroscop
CV	Cyclic voltammetry
LIBs	Lithium ion batteries
XRD	X-ray diffraction

1 INTRODUCTION

With the rapid economic growth, energy production and consumption are becoming one of the major challenges to the humanity. The increasing consumption of limited fossil fuels and the related environmental impact, including emissions of pollutants and greenhouse gases, has prompted the development of clean energy technologies. Among various forms of renewable energy storage systems, such as for wind and solar power, which are limited by natural conditions, lithium-ion batteries (LIBs) are the primary candidate for electrical vehicles (EVs) and many portable electronic devices due to their high energy density and power density.

A LIB cell includes a cathode and an anode soaked in an electrolyte solution, which enables lithium ion transfer between the two electrodes during the charge-discharge process. The two electrodes are separated by a porous membrane separator. Currently, anode materials, such as silicon (Si), germanium (Ge), and phosphorus (P) could deliver satisfactory specific capacity of 3000 mAh g^{-1}, 1200 mAh g^{-1}, and 1600 mAh g^{-1}, respectively. The development of cathode materials with high capacity, however, is far behind that of anode materials. The $LiCoO_2$ cathode materials used in commercial LiBs show limited specific capacity (140 mAh g^{-1}). Therefore, developing a new cathode material with high capacity is the key to ensuring capacity matching in the anode/cathode pairs for LiBs. Sulfur, as one of most promising cathode materials, has gained much attention in the past few years, because it has a theoretical specific capacity of 1675 mAh g^{-1} and a theoretical energy density of 2567

Wh kg^{-1} when paired with Li metal anodes. Furthermore, it features cost effectiveness, abundance, and nontoxicity, all of which make it a promising candidate for next-generation batteries.

A typical lithium-sulfur (Li-S) battery consists of four components, including the lithium metal anode, separator, electrolyte, and sulfur cathode. In an organic liquid electrolyte, the discharge of the sulfur cell operates by the reduction of S at the cathode on discharge to form various polysulfides and to ultimately produce Li_2S, after reaction with Li through multiple steps. In spite of its high theoretical energy density, practical application of the Li-S battery is hindered by low sulfur utilization and unsatisfactory capacity retention. In the past decade, many approaches have been used to improve the electrochemical performance of Li-S batteries in the following directions:

1. Development of sulfur cathodes with favourable nanostructures by employing different architectures for the matrix.

2. Investigation of the electrochemical performance of Li-S batteries with different types of electrolyte.

3. Functionalization of the separator by surface coating, such as with carbon and polymer.

4. Modification of the lithium anode so as to prevent degradation and to permit utilization of the protected lithium anode, and the preparation of alternative Li/M (M = Si, Sn, C) alloys.

5. Exploring new types of binders for Li-S batteries.

6. Other strategies, control of charge-discharge voltage window and novel cell configurations (interlayers, integrated electrode).

In my doctoral work, the main goal has been to improve the electrochemical performance of Li-S batteries through construction of various kinds of nanostructured sulfur cathodes and novel configuration methods for the sulfur cathode. The effect of nanostructures and of morphology, physical and chemical properties, and novel configuration methods on electrochemical performance was investigated.

A brief overview of the chapters in this thesis:

Chapter 2 presents a literature review on Li-S batteries, including a brief history of Li-S batteries, the working mechanisms of Li-S batteries, and their advantages, challenges, solutions, and future development directions.

Chapter 3 presents the experimental, characterization, and testing methods used in this thesis, including chemicals, preparation techniques, and physical and electrochemical testing methods.

Chapter 4 investigates the electrochemical performance of TiO_2 coated three-dimensional (3D) hierarchically ordered porous carbon-sulfur composite cathode for Li-S batteries. The 3D hierarchically ordered porous carbon was synthesized through an evaporation-induced coating and self-assembly method using foam as template. The hierarchical architecture provides a 3D conductive network for electron transfer, open channels for ion diffusion and strong confinement of soluble polysulfides. Meanwhile, a TiO_2 coating layer could further effectively prevent the

dissolution of polysulfides and also improve the strength of the entire electrode, thereby enhancing the electrochemical performance.

Chapter 5 investigates the electrochemical performance of sulfur cathodes produced by employing two typical kinds of nanoporous carbon derived from cotton as matrix. Compared to the pure microporous structure, a hierarchically porous structure with a micro-macropore framework is highly desirable for high-performance electrode materials. The macroporous structure of this carbon provides channels allowing sulfur to be loaded into micropores and promotes fast transport of electrons/ions and electrolyte. The microporous structure can trap elemental S and Li polysulfides during cycling. As a result, the composite electrode exhibits an excellent capacity of 760 mAh g^{-1} after 200 cycles and good rate capability.

Chapter 6 investigates the synthesis of ordered mesoporous carbon fibers prepared by the electrospinning technique and its application as cathode material for lithium-sulfur batteries. Not only can the ordered mesoporous structure ensure good electrical pathways for the active sulfur, it can also effectively trap soluble polysulfide intermediates during charge-discharge processes. In addition, the ordered mesoporous cabon fiber-sulfur (OMCF-S) composite has excellent mechanical stability during the charge-discharge process. The resulting OMCF-S composite with 63% S exhibits high reversible capacity, good capacity retention, and enhanced rate capacity when used as cathode in rechargeable lithium-sulfur batteries.

Chapter 7 presents a novel strategy for configuration of an integrated flexible sulfur cathode for high-performance lithium-sulfur batteries. A unique flexible cathode

architecture was developed consisting of a carbon/sulfur/carbon (CSC) sandwich structure coated directly on a polypropylene (PP) separator via the doctor blade method. The CSC@separator cathode delivered a high reversible capacity of 730 mAh g^{-1} over 500 cycles, with capacity decay as low as 0.058% per cycle and a low self-discharge constant of 0.0293 per week. The improved performance is attributed to the enhanced electronic conductivity, toleration of volume expansion, and control of the polysulfide diffusion in the unique integrated sandwich-structured electrode. Together with the simple and scalable nature of its fabrication, our integrated sandwich structured electrode is highly promising for practical application in Li-S batteries.

Chapter 8 presents a novel type of one-dimensional organic selenium-containing fiber with superior performance for lithium-selenium (Li-Se) and sodium-selenium (Na-Se) Batteries. The organic selenide fibers composed of carbonized polyacrylonitrile/selenium (CPAN/Se) were synthesized by heating polyacrylonitrile-selenium (PAN-Se) fibers via the electrospinning technique at 600 ^{o}C. The Se atoms are confined by N-containing carbon ring structures in the form of energy-storing selenium side chains in the carbonized PAN matrix. Such a unique chemical structure not only enhances the electrical conductivity, but also can confine selenium during the charge and discharge processes, leading to superior long-term cycling stability and good rate performance. The CPAN/Se electrodes could retain a reversible capacity of 600 mAh g^{-1} over 500 cycles in the Li-Se battery and 410 mAh g^{-1} over 300 cycles in the Na-Se battery.

Chapter 9 contains the general conclusion of this thesis and a discussion of possible future directions for Li-S batteries.

2 LITERATURE REVIEW

Nowadays, the consumption of non-renewable fossil fuels is continuously rising with the development of society, resulting in global warning and air pollution. Developing alternative and renewable energy sources, such as wind power, wave power, and solar power systems, therefore, will become more important in the future than at any time in the past. These energy resources are intermittent, however due to their natural limitations. The rechargeable lithium-ion battery system as an alternative energy resource is one of the most viable options for energy storage, because of its high operating voltages, high energy density, and absence of a memory effect.

Li-ion batteries have a major advantage over any other rechargeable battery system (lead-acid, nickel-cadmium, nickel metal hydride systems) with regards to their specific energy density, and they have dominated the rechargeable battery market for electronic devices over the past two decades. Nevertheless, the commercial lithium-ion batteries typically contain a lithium transition-metal (M) oxide cathode ($LiCoO_2$, $LiMn_2O_4$, and $LiFePO_4$) and a graphite anode, which have insufficient energy densities (in practice, 100-220 Wh kg^{-1}) to fulfil the needs of power-intensive applications such as electric vehicles [1].

Therefore, developing novel electrode materials possessing high gravimetric and volumetric capacity is necessary. Lithium-sulfur batteries have gained much attention in the past few years. Coupled with a lithium metal anode, the theoretical energy density of the Li-S battery is about 2600 Wh kg^{-1} or 2800 Wh L^{-1}, which is much higher than for the commercial $LiMO_2$-graphite system (Figure 2.1).

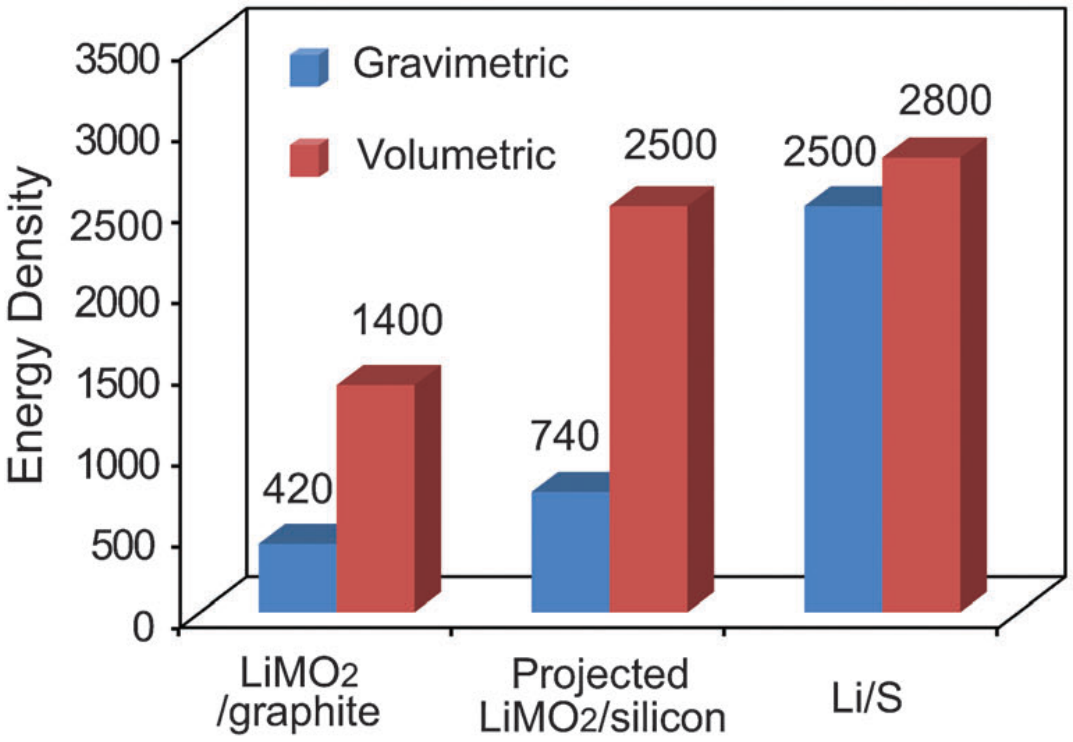

Figure 2.1 The theoretical energy density of different rechargeable battery systems based on active materials only. The units are Wh kg^{-1} and Wh L^{-1} for gravimetric and volumetric energy density, respectively. M= $Ni_{1/3}Mn_{1/3}Co_{1/3}$ for the $LiMO_2$–graphite system. For projected $LiMO_2$–silicon cell, the specific capacity for the cathode and anode are 250 and 3000 mAh g^{-1}, respectively. The density is 4.8 g cm^{-3} for $LiMO_2$, and the capacity per volume is 2200 mAh L^{-1} for silicon after considering the necessary space for volume expansion [2].

2.1 Introduction to lithium/sulfur batteries

Sulfur is one of the most abundant elements on the Earth, offering a series of advantages, including ultra-high energy density of 2567 Wh kg^{-1} and high theoretical specific capacity of 1675 mAh g^{-1}. These features make it one of the most promising

cathode candidates for the next generation of batteries [3-6]. Herbet and Ulam first introduced the concept of utilizing sulfur as a cathode material in 1962 [7]. A schematic diagram of the components in Li-S cell is displayed in Figure 2.2 The traditional Li-S cell system composes a sulfur cathode, a metallic lithium anode, and the electrolyte. The operation of a Li-S cell should start with discharge, as sulfur is in the charged state. During the first discharge, the sulfur is reduced to generate lithium sulfide (Li_2S) by accepting electrons and lithium ions, while lithium metal is oxidized to produce lithium ions and electrons. In the flowing charge process, Li_2S is converted to sulfur through the formation of a series of intermediate lithium polysulfides.

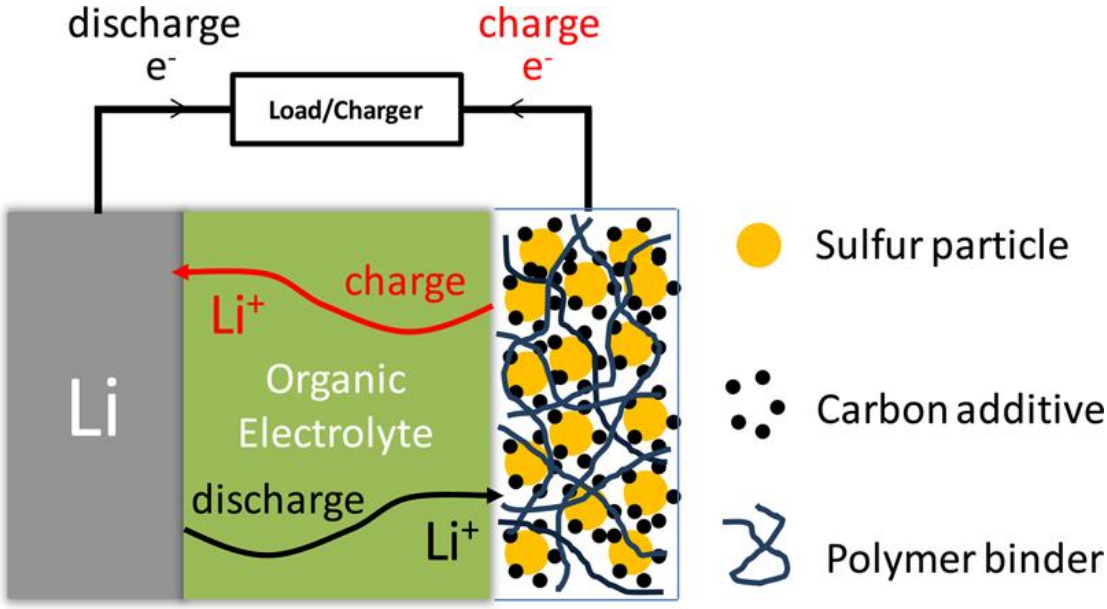

Figure 2.2 Schematic diagram of a Li-S cell with its charge/discharge operations [8].

The electrochemical reaction of Li-S system is complicated. In an organic liquid electrolyte, the discharge of the sulfur cell operates by reduction of S at the cathode on discharge to form various polysulfides and to ultimately produce Li_2S [9,10]. The

reaction includes multiple processes associated with lithium polysulfides with different chain lengths:

$S_8 + 2e^- \longrightarrow S_8^{2-}$

$3S_8^{2-} + 2e^- \longrightarrow 4S_6^{2-}$

$2S_6^{2-} + 2e^- \longrightarrow 3S_4^{2-}$

$S_4^{2-} + 4Li^+ + 2e^- \longrightarrow 2Li_2S_2$

$Li_2S_2 + 2Li^+ + 2e^- \longrightarrow 2Li_2S$

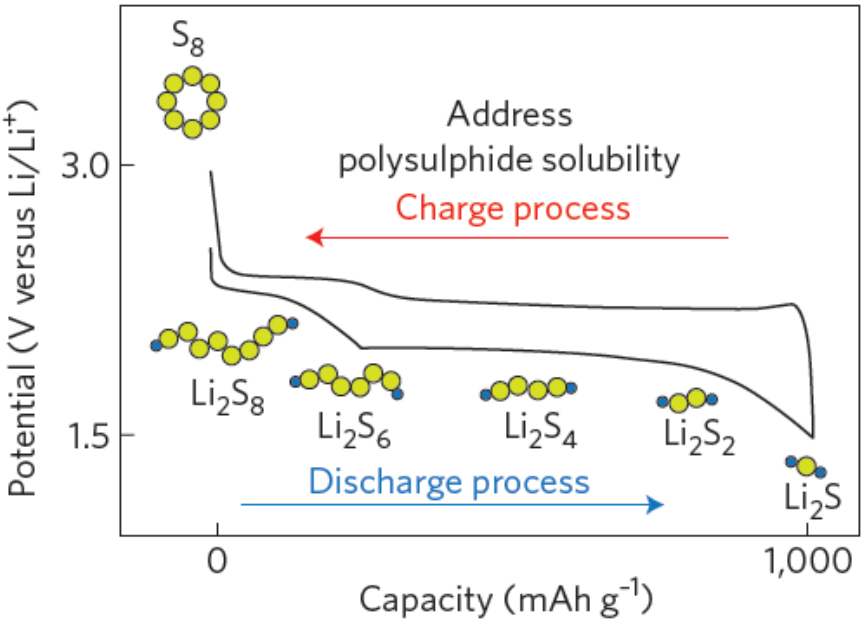

Figure 2.3 Voltage profile of Li-S cell [11].

The voltage profiles of a Li-S cell are shown in Figure 2.3 [11]. There are two discharge plateaus at 2.3 and 2.1 V in the voltage profiles. The high plateau corresponds to the first three conversion steps from S_8 to Li_2S_4, and the high-order lithium polysulfides produced in these steps are soluble in the electrolyte. The lower plateau represents the conversion of Li_2S_4 to Li_2S, and the resulting products (Li_2S_2, Li_2S) are insoluble in the electrolyte [12].

2.2 Technical Challenges of Li-S batteries

Although Li-S batteries have many advantages, in order to commercialize the Li-S batteries, many challenges have to be overcome.

2.2.1 Poor electrical conductivity of S and its discharge product Li_2S

The first challenge is the low electrical conductivity of sulfur (5×10^{-30} S cm^{-1}) and its discharge products in the form of intermediate polysulfides, which impedes their acceptance of electrons from the current collector, leading to low electrochemical accessibility and low utilization of the sulfur. As a result, various kinds of conductive framework need to be added into the sulfur cathode, so as to enhance the conductivity of the whole electrode.

2.2.2 Volume Expansion

Volume changes of sulfur take place during the cycling. The density of sulfur and Li_2S is 2.03 g cm^{-3} and 1.66 cm^{-3}, respectively. The volume expansion is as large as 80% when the sulfur is completely converted to Li_2S, breaking down the intimate connect among the active sulfur materials, binder, additive carbon, and aluminium current collector. This results in the pulverization of the sulfur cathode materials and fast capacity fading.

2.2.3 Dissolution of polysulfides and the related shuttle effect

The high diffusivity and solubility of the intermediate lithium polysulfides is the main challenge that needs to be overcome. During charge-discahrge process, sulfur is firstly converted to the soluble long-chain polysulfides, which can diffuse from the cathode and react with the lithium anode to generate insoluble short-chain polysulfides in the

form of Li_2S or Li_2S_2, leading to the precipitation of these species on the surface during cycling processes, leading to both the loss of active materials and an increase in impedance. In addition, the dissolution and diffusivity of polysulfides leads to the so-called shuttle effect as well. The long-chain polysulfides diffuse through the separator, reaching anode side and are reduced to short-chain polysulfides, and then the short-chain polysulfides travel back to the cathode region and are oxidized to long-chain polysulfides. This continuous process generate an internal so-called "shuttle effect", which decreases the utilization of the sulfur material and the Coulombic efficiency.

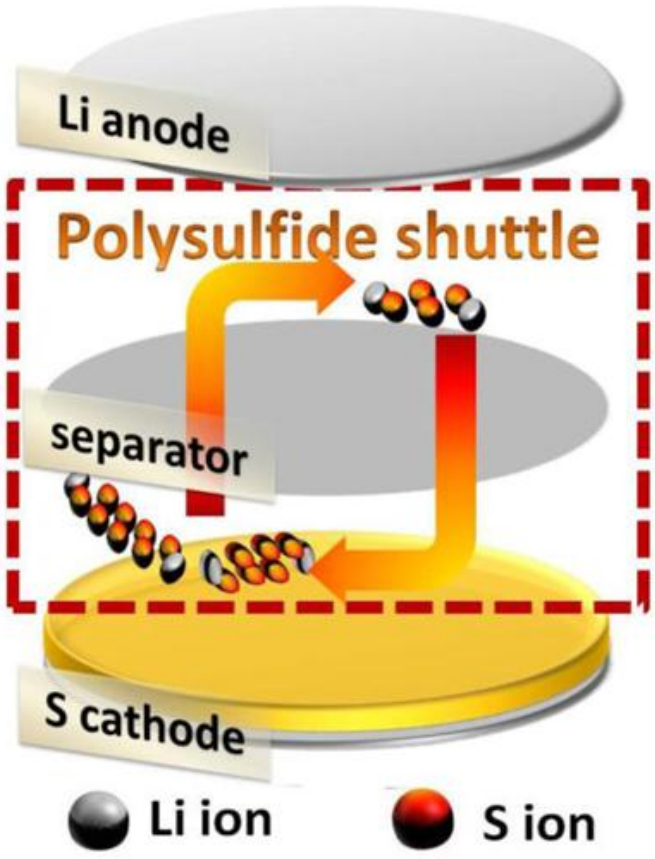

Figure 2.4 Illustration of the shuttle mechanism occurring in a Li-S cell [8].

2.2.4 Self-discharge

Self-discharge is another important criterion to assess the practicality of the energy-storage devices. However, Li-S batteries suffer from sever self-discharge behaviour. The severe self-discharge behaviour mainly arises from the dissolution of sulfur/high-order polysulfides in the electrolyte during long-term storage. The dissolved sulfur-based species could migrate to the anode side and convert to polysulfides, leading to a decrease in the open-circuit voltage and discharge capacity.

2.3 Solutions

In the past decade, many approaches have been used to overcome the challenges of Li-S batteries, including construction of sulfur cathodes with favourable nanostructures, modification of the electrolyte, binder and lithium anode, functionalization of the separator, novel cell configurations, changing the voltage window, and using novel sulfur cathodes.

2.3.1 Construction of nanostructured sulfur cathode

In the past few years, the major stream of Li-S research has been focusing on designing sulfur cathodes with different nanostructures, constraining active sulfur materials within various kinds of porous matrices, including porous carbon or graphene, polymer, metal oxide. Another way is to apply surface coatings of conductive polymer or metal oxides (TiO_2 or Al_2O_3) to confine sulfur in order to achieve stable performance. The additional matrix not only greatly improves the conductivity of the whole electrode, but also plays an important role in terms of suppression of the shuttle effect and toleration of the volume changes during the

charge-discharge process. Tremendous progress has been made on improving the electrochemical performance of Li-S batteries. Basically, the development of sulfur cathodes can be divided into several classes in terms of composition and structure, including porous carbon-sulfur composites, graphene (oxide)-sulfur composites, polymer-sulfur composites, and metal oxide-sulfur composite.

2.3.1.1 Sulfur-porous carbon composites

Porous carbons can be classified into three categories according to the pore size (diameter, *D*), including microporous ($D < 2$ nm), mesoporous (2 nm < D < 50 nm), and macroporous ($D > 50$ nm). Both the microporous [13-16] and mesoporous [17-21] carbons have been demonstrated to provide an ideal confinement matrix for encapsulating sulfur, and electrodes containing them demonstrate higher utilization and retention rate of sulfur, resulting in good electrochemical performance. Macroporous pores, mainly derived from interwoven network of carbon nanotubes, can supply channels for electrolyte transport and store more sulfur compared to microporous and mesoporous carbon.

Wang et al. [22] conducted pioneering work on loading sulfur into porous carbon with a pore size of 2.5 nm by ae thermal treatment method and used sulfur-carbon composite as a cathode material. Their composite with 30 wt.% sulfur content exhibited high capacity of 800 mAh g^{-1} in the first cycle and reversible capacity of 440 mAh g^{-1} after 25 cycles. Recently, Ji et al. [21] reported the ordered mesoporous carbon CMK-3 as an improved matrix to trap polysulfides. CMK-3 mesoporous carbon consists of hollow 6.5 nm thick carbon tubes separated by channel voids 3-4

nm wide (Figure 2.5). The composite was prepared by simply heating a mixture of sulfur and CMK-3 in a mass ratio of 7 : 3 at 155 ^{o}C. The CMK-3 sulfur composite electrode containing 59% S exhibited high discharge capacity up to 1005 mAh g^{-1}, which was further improved to 1320 mAh g^{-1} by connecting the carbon surfaces with polyethylene glycol. Guo et al. [14] prepared chainlike sulfur molecules within a conductive microporous carbon matrix and found that the confined S_{2-4} molecules can fully avoid the transition from S_8 to S_4^{2-} during the charge-discharge process, thereby preventing the formation of soluble polysulfides and minimizing the shuttle effect. The as-prepared S_{2-4}/carbon electrode shows a high reversible capacity of 1149 mAh g^{-1} after 200 cycles.

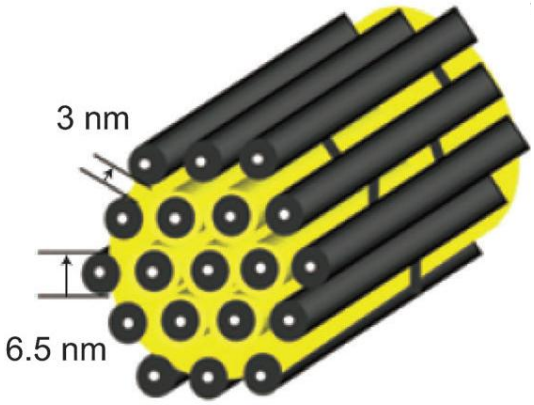

Figure 2.5 A schematic diagram of sulfur (yellow) confined within the interconnected pore structure of mesoporous carbon (CMK-3) formed from carbon tubes that are held together by carbon nanofibers [21].

In addition, hollow carbon spheres, including single-shelled hollow carbon spheres and double-shelled hollow carbon spheres, were also used as matrix to confine sulfur to achieve high-performance lithium-sulfur batteries [23-27]. Usually, the hollow

carbon spheres were prepared by the hard template method. When the metal oxide nanoparticles functioning as cores were removed, hollow carbon spheres can be obtained. Archer's group [24] reported a kind of hollow carbon sphere with a diameter of about 200 nm and wall thickness of 40 nm (Figure 2.6), and then used it as a carbon matrix to take up sulfur (with 70% content of sulfur in the composite) for lithium-sulfur batteries. The as-prepared sulfur cathode delivered excellent cycling performance, maintaining high capacity of 974 mAh g^{-1} at 0.5 C after 100 cycles.

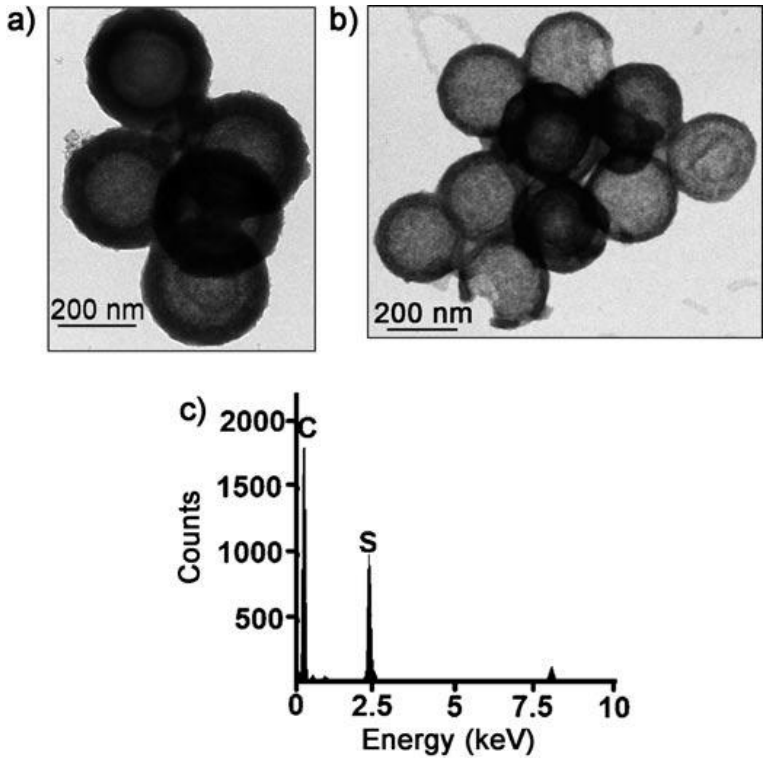

Figure 2.6 TEM images of a) mesoporous carbon hollow spheres b) C@S nanocomposite and c) EDX analysis of C@S nanocomposite showing the presence of sulfur [24].

One dimensional carbon materials, such as carbon nanotube (CNTs) and carbon nanofibers, were also used to confine sulfur and demonstrated improved cycling life.

CNTs have several advantages, including good mechanical strength and high conductivity. In the early research, Han et al. [28] used a multi-wall CNT composite containing 50% sulfur as cathode material, and it showed improved cycling and rate performance. The CNTs can form a three-dimensional (3D) network with high conductivity, as well as having a high surface area, which enhanced their capability of absorbing polysulfides. Afterwards, many advanced sulfur cathode materials based on CNTs were prepared to obtain satisfactory electrochemical performance [29-35]. Recently, Jin et al. [36] prepared a very interesting nanostructured carbon nanotube-sulfur composite, in which small carbon nanotubes with diameter of about 20 nm and sulfur were packed inside the large nanotubes (diameter of 200 nm). This tube in tube nanostructured sulfur composite showed high sulfur utilization, high discharge capacity and high rate performance due to its unique structure, along with high electrical conductivity, structural stability, and suppressed dissolution of polysulfides.

Similar to the CNTs, the carbon nanofibers (CNFs) are also widely used in preparing sulfur composite materials due to their high electrical conductivity and structural stability [37-44]. Zhang et al. [40] prepared polyaniline-decorated hollow carbon nanofiber (HCNF@PANI) and used it as a conductive matrix to confine sulfur for use as a cathode material. The as-prepared HCNF@PANI composite exhibited enhanced electrochemical performance, which is attributed to the unique nanostructure and the good dispersion of sulfur in the composite. Ji et al. [42] designed a porous carbon nanofiber-sulfur composites, which showed high discharge capacity and improved

rate performance. The carbon fibers with porous structure not only improve the electrical conductivity, but also could immobilize the polysulfides during the charge-discharge process.

2.3.1.2 Sulfur-graphene (oxide) composites.

Graphene is a two dimensional (2D) one-atom-thick planar carbon nanosheet with high surface area, very good stable chemical properties, flexibility and ultra-high electronic conductivity [45]. All these features make it an excellent matrix to link electrode materials for energy storage applications. Graphene oxide (GO) is oxidized graphene, which contains oxygen bonds, such as -OH, C-O-C, and C=O. These functional groups could play an important role as immobilizers to confine any polysulfides and prevent them from dissolving [46-48].

Early work on graphene-sulfur composite materials for Li-S batteries was reported by Wang et al. [49] using the thermal treatment method. The composite with only 17.6 wt % sulfur showed severe capacity fading in the first cycle, however, it was demonstrated that this method is not an effective way to confine polysulfides due to the open structure of the composite. Therefore, the solution method is widely used to synthesize sulfur composite with a closed structure by dissolving sulfur in an organic solvent. Cao et al. [50] prepared a functionalized graphene sheet-sulfur (FGSS) nanocomposite with a sandwich-type architecture, which was further coated with a thin layer of cation exchange Nafion polymer film. The obtained composite electrode exhibited enhanced cycling performance with 75% capacity retention after 100 cycles.

Furthermore, graphene-oxide-sulfur composites have also been investigated to improve the electrochemical performance of Li-S batteries [51-54]. Li et al. [52] used a chemical method to immobilize sulfur and lithium polysulfides through the reactive functional groups on the graphene oxide. They used a chemical-reaction-deposition approach to coat a thin layer of sulfur on graphene oxide sheets. The GO in the composite had good conductivity and high specific area, and the functional groups on the surface of the GO play a critical role in immobilizing polysulfides so as to prevent them from dissolving and maintaining intimate contact between the matrix and the sulfur, leading to excellent capacity stability of 1000 mAh g^{-1}.

In addition, graphene is easily stacked, which will decrease the conductivity of chemically derived graphene due to the introduction of structural defects. Recently, Zhao et al. [55] reported a novel kind of unstacked double-layer templated graphene synthesized through template-directed chemical vapour deposition. The as-prepared graphene consists of two unstacked graphene layers separated by mesosized protuberances and is then used as a conductive matrix to load sulfur for lithium-sulfur batteries. This uniquely structured material exhibits excellent electrochemical performance. Even at the high rates of 5 C and 10 C, it still delivered high capacities of 1034 mAh g^{-1} and 734 mAh g^{-1}, respectively.

2.3.1.3 Polymer-sulfur composites

Polymers play an important role in Li-S batteries and polymer-sulfur composites, so they have been investigated along with their carbon counterparts. Compared to the carbon architectures, polymer-based processing takes place below 100 ^{o}C, which

makes it possible to synthesize structures that are difficult to realize as carbon-sulfur composites, such as coatings of conductive polymer layers to trap polysulfides. In addition, chemical method should be a more efficient strategy to confine the sulfur and polysulfides compared to physical methods, as it involves functional groups and the unique chemical structure which have strong interaction with polysulfides, yielding excellent stability and activity.

Indeed, conductive polymers, including polythiophene, polypyrrole, and polyaniline, have been used as a matrix to physically absorb and hold sulfur [56-60]. A sulfur/polythiophene composite with a core/shell structure was constructed via an in situ oxidative polymerization method by Wu et al. [57]. The conductive polythiophene plays the role of a conductive matrix and porous adsorbing agent, leading to Li-S batteries with improved electrochemical performance. As a result, capacity of 830.2 mAh g^{-1} can be retained after 80 cycles. Wang et al. [59] synthesized sulfur-polypyrrole composite cathodes material by a chemical polymerization method. The surfaces of the sulfur powder were coated with nanosized polypyrrole particles, thereby improving the electrical conductivity and cycling stability. The initial discharge capacity was increased from 1100 mAh g^{-1} to 1280 mAh g^{-1} for the sulfur electrode after coating with polypyrrole. Recently, Liu et al. reported the synthesis of polyaniline nanotubes that were suitable for sulfur loading by a soft approach [60]. Three-dimensional (3D), cross-linked, structurally-stable sulfur-polyaniline nanotubes were formed by heating the sulfur and polymer at 280 ^{o}C. This well-designed framework provides strong physical and

chemical confinement of the sulfur and polysulfides. The resultant electrode could retain a high reversible discharge capacity of 837 mAh g^{-1} after 100 cycles at a current density of 0.1 C.

Furthermore, polyacrylonitrile (PAN) could react with sulfur at a high calcination temperature to form a heterocyclic polymer linking sulfur molecules on its side chains. [61-67] This sulfur composite with a unique chemical structure displayed excellent electrochemical performance. Wang et al. [61] was the first to report this structure, which was prepared by mixing elemental sulfur and PAN via heat treatment at 280-300 ^{o}C. The composite showed an initial capacity of 850 mAh g^{-1} and retained capacity of 600 mAh g^{-1} after 50 cycles. Recently, Wei et al. [66] investigated the form of the sulfur in the sulfur/PAN composite. It was found that the sulfur in the composite exists as S_3/S_2 units covalently linked to a carbon main chain containing N groups through spectroscopic and electrochemical methods. The phenomenon of polysulfide dissolution and the shuttle effect can be completely eliminated due to the unique chemical structure. The sulfur/PAN cathode can deliver a high capacity of 1000 mAh g^{-1} even after 1000 cycles.

2.3.1.4 Metal oxide-sulfur composite

Besides conductive polymer, other materials including metal oxides have also been applied in sulfur-based composites. The role of alternative additives is to serve as an absorbing agent to confine the polysulfides. The adsorption materials proposed in the relevant publications include silica, aluminium oxide, and transition metal oxides [68-70]. Song et al. added $Mg_{0.6}Ni_{0.4}O$ nanosized particles into sulfur electrodes as an

adsorbing material to suppress polysulfide migration and diffusion [68]. A good electrochemical performance with capacity retention of up to 85% over 50 cycles can be obtained. Furthermore, Al_2O_3 nanoparticles were also utilized as a similar adsorbing agent and had a similar effect. The composite electrode with 10 wt% Al_2O_3 could deliver a discharge capacity of 660 mAh g^{-1} [69].

Recently, metal oxides have been regarded as reacting with lithium polysulfides to from surface-bound intermediates, mitigating the dissolution of the polysulfides and thus improving the electrochemical performance of the lithium-sulfur batteries. [71-73] Nazar's group [71] reported a strategy to trap polysulfides by using Ti_4O_7 as the sulfur host material. Physical and electrochemical testing indicated that surface interactions play an important role in polysulfide dissolution. The Ti_4O_7/S electrode delivered a high discharge capacity of 1070 mAh g^{-1} at 0.2 C. Subsequently, they also used another metal oxide (manganese dioxide nanosheet) as the matrix to prepare sulfur cathode material. A new mechanism is proposed. The active polythionate complex acts as a transfer and anchor mediator to prevent the dissolution of polysulfides and control the deposition of Li_2S_2 and Li_2S [72].

Another attractive method is to create a physical barrier to prevent soluble polysulfides from dissolving into the organic electrolyte through a metal oxide thin film coating on the surface of the active material. Such metal oxide barrier materials include TiO_2 [74], Al_2O_3 [75], SiO_x, and VO_x [76]. Compared with a polymer coating, a metal oxide coating layer could almost completely block out-diffusion of the polysulfides and enhance the strength of the entire electrode to withstand structural

damage during long cycle testing. Seh et al. [74] prepared a TiO_2-sulfur yolk-shell composite through a chemical method. The resulting composite exhibited excellent cyclability over 1000 cycles. This can be attributed to its unique nanoarchitecture with internal void space to tolerate the volume changes and the TiO_2 shell to avoid the dissolution issue. In addition, Kim et al. [75] proposed the use of a thin layer of aluminium oxide on the surface of the electrode where it can be grown by rapid plasma enhanced atomic layer deposition (PEALD). After the PEALD alumina was coated on the composite, the electrodes exhibited enhanced electrochemical performance with a capacity exceeding 600 mAh g^{-1} after 300 charge-discharge cycles. Energy dispersive spectroscopy (EDS) results of the electrode confirmed that the PEALD alumina coating significantly reduced dissolution issue of sulfur from the cathodes, as the outside alumina layer could well confine the polysulfides within inside.

2.3.2 Lithium sulfide cathode

Lithium sulfide (Li_2S), as the final lithiation product of sulfur, has a high specific capacity of 1166 mAh g^{-1}, and it is more suitable as the sulfur cathode material because it allows other safe anodes (such as silicon and tin) to replace the lithium anode [77-79]. Nevertheless, many challenges need to be overcome before its commercial application can be realized, including low electronic and ionic conductivity, sensitivity to air, dissolution of polysulfides, and shuttle effect problems. To improve the conductivity of Li_2S, the most widely used approach is to prepare Li_2S-carbon composite. The addition of carbon can greatly improve the electronic

conductivity of the composite, as well as playing a role in inhibiting the dissolution of the polysulfides during the charge-discharge process.

Early work was focused on balling method to synthesize Li_2S-carbon composite [78,80]. Cai et al. synthesized Li_2S-carbon composite via a high-energy ball-milling method using micrometer-sized Li_2S particles and carbon black as starting materials. The composite (Li_2S content, 67.5%) showed an initial capacity of 1144 mAh g^{-1} and retained 411 mAh g^{-1} after 50 cycles at 0.1 C. The chemical vapour deposition (CVD) carbon coating method can also be used in preparing Li_2S-carbon composite, as Li_2S has a high decomposition temperature above 900 ^{o}C. Nan et al. [81] successfully synthesized carbon-coated Li_2S core-shell particles for the first time through the CVD method (Figure 2.7). Firstly, sulfur was dissolved in toluene, and then the solution was added into lithium triethylborohydride in tetrahydrofuran to obtain Li_2S particles. The particle size of Li_2S is controlled by the reaction time. After that, the as-prepared Li_2S spheres were heated and coated with carbon by CVD. The stable carbon shell not only can enhance the electrical conductivity of the composite, but also can help to prevent polysulfides from dissolving into the electrolyte, thereby inhibiting the shuttle effect and improving the electrochemical performance of the cathode. The Li_2S@C core-shell particles delivered a high initial discharge capacity of 1394 mAh g^{-1}, retaining capacity of 1056 mAh g^{-1} after 100 cycles at 0.2 C. Hwa et al. [82] developed core-shell nanostructures (Li_2S/GO@C) consisting of Li_2S nanospheres with an embedded graphene oxide (GO) sheet as the core and a conformal carbon layer as the shell by the CVD method. The excellent electrochemical performance is

attributed to several reasons: the carbon shell of the composite could maintain its structural stability during the cycling and improve the electrical conductivity; the GO sheet serves as a second physical and chemical barrier to supress the dissolution of polysulfides. The resulting Li_2S/GO@C cathode displayed a specific capacity of 699 mAh g^{-1} (calculation based on Li_2S) after 400 cycles at 0.05 C.

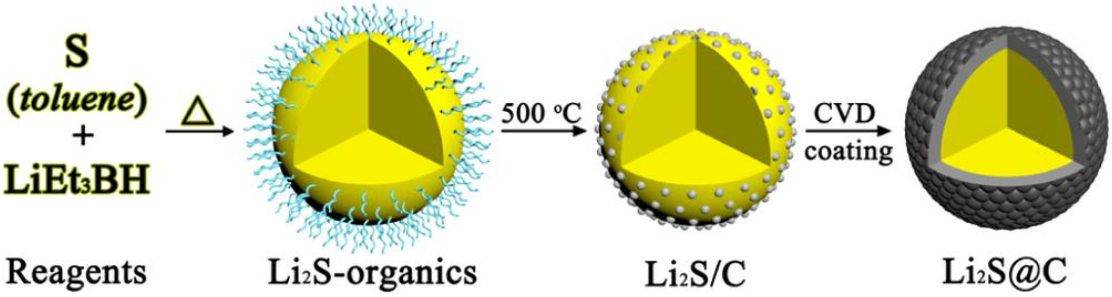

Figure 2.7 Schematic of the coating process for the Li_2S@C spheres [82].

In addition, several kinds of chemical synthesis methods have been applied to prepare Li_2S-carbon composite. [83-89] Cui Yi's group reported Li_2S-polypyrrole (Li_2S-PPy) composite cathode for lithium-sulfur batteries. The Li_2S-PPy structure is synthesized through polymerization of pyrrole on Li_2S in anhydrous methyl acetate solvent. The introduction of N atoms in PPy enables PPy to have strong interactions with Li_2S, thus constraining intermediate polysulfides during the charge-discharge process. On the other hand, PPy as a conducting polymer can enhance the electrical conductivity. The as-prepared Li_2S–polypyrrole composite delivered high discharge capacity of 785 mA h g^{-1} of Li_2S with stable cycling over 400 cycles. Another type of nanostructure, Li_2S-CMK-3, was prepared by Yang et al. [85] via chemically lithiating sulfur-CMK-3 composite with n-butyllithium. After the lithiation process, over 90% of sulfur was converted to Li_2S. The Li_2S-CMK-3 composite cathode delivered an

initial discharge capacity of 573 mAh g^{-1}. Guo et al. [87] synthesized a novel Li_2S-carbon composite via a high temperature carbonization technique, in which PAN was used as the carbon source. Firstly, lithium sulfide was mixed with PAN in dimethyl formamide (DMF) solvent. The Li_2S can interconnect the PAN network via lithium sulfide net-nodes. After drying, the resulting material was heated at 300 ^oC and then at 600 ^oC under argon atmosphere. As a result, a Li_2S-carbon composite was obtained, in which N-containing carbon ring structures encapsulate lithium sulfide species (Figure 2.8). At the current density of 200 mA g^{-1}, the composite cathode delivered stable capacity of 500 mAh g^{-1}. Recently, Seh et al. [88] reported a smart design for Li_2S cathode materials, with the Li_2S encapsulated by two-dimensional layered transition metal disulfides (TiS_2). The obtained $Li_2S@TiS_2$ core-shell nanoarchitecture was prepared by a simple but smart method. The ball-milled commercial Li_2S particles were dispersed in anhydrous ethyl acetate, and then $TiCl_4$ precursor was added to react with Li_2S on the surface to form a TiS_2 coating layer. The transition metal disulfide (TiS_2) layer not only improved the electrical conductivity of the composite, but also showed strong binding with Li_2S, according to the results of ab initio simulations. A high capacity of 503 mAh g^{-1} could be obtained at the high rate of 4 C.

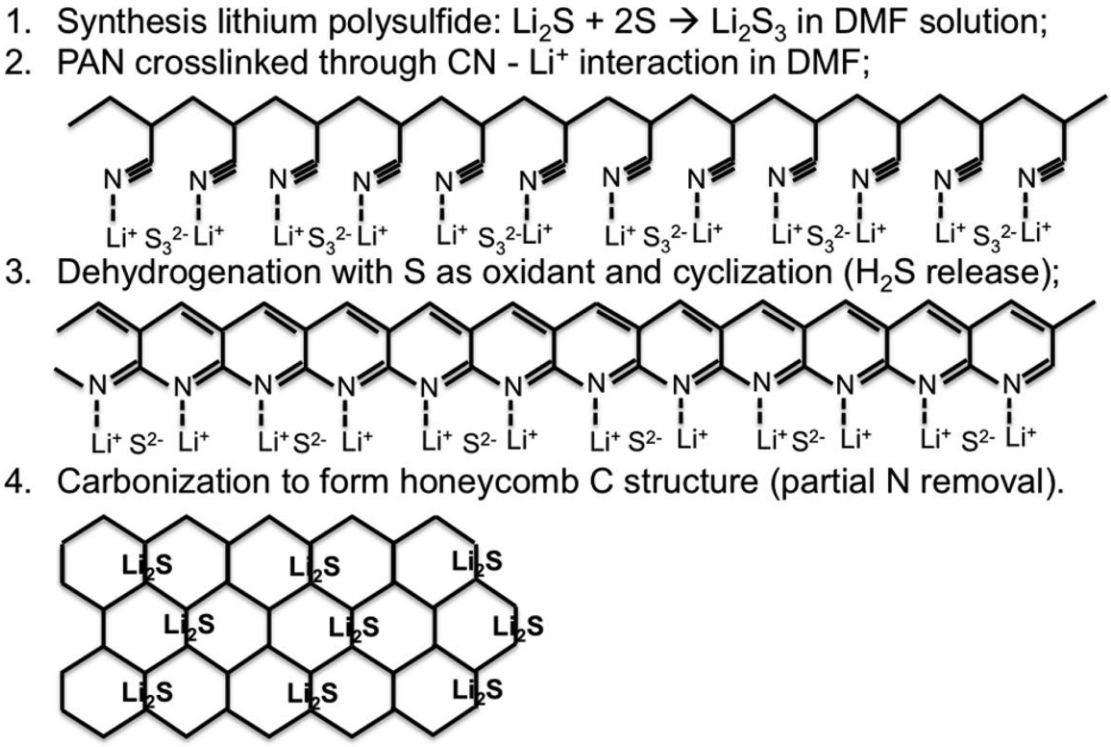

Figure 2.8 Proposed synthesis route for creating Li_2S-carbon cathode materials [87]**.**

To further explore new synthesis methods, some efforts have been devoted to preparing free-standing Li_2S cathode [90-94]. Wang et al. [90] prepared Li_2S/reduced graphene oxide (Li_2S/rGO) free-standing paper as cathode for lithium-sulfur batteries through a liquid-infiltration-evaporation coating method. The preparation process is shown in Figure 2.9. It was found that Li_2S particles with diameters around 100 nm were uniformly distributed on the surfaces of graphene oxide. The obtained Li_2S/rGO paper can work directly as a free-standing cathode, showing good flexibility as well as excellent electrochemical performance due to the improved electrical conductivity and strong absorption of graphene oxide. Manthiram's group [91] recently designed three-dimensional Li_2S-coated B- or N-doped graphene aerogel cathodes via a similar method to the one mentioned above. Enhanced electrochemical performance of the free-standing cathode has been obtained. On the one hand, doped graphene has a

strong interaction with polysulfide species, thus alleviating the dissolution of polysulfides. On the other hand, the three-dimensional porous structure could facilitate the transport of electrons and ions, and also accommodate the volume expansion during cycling.

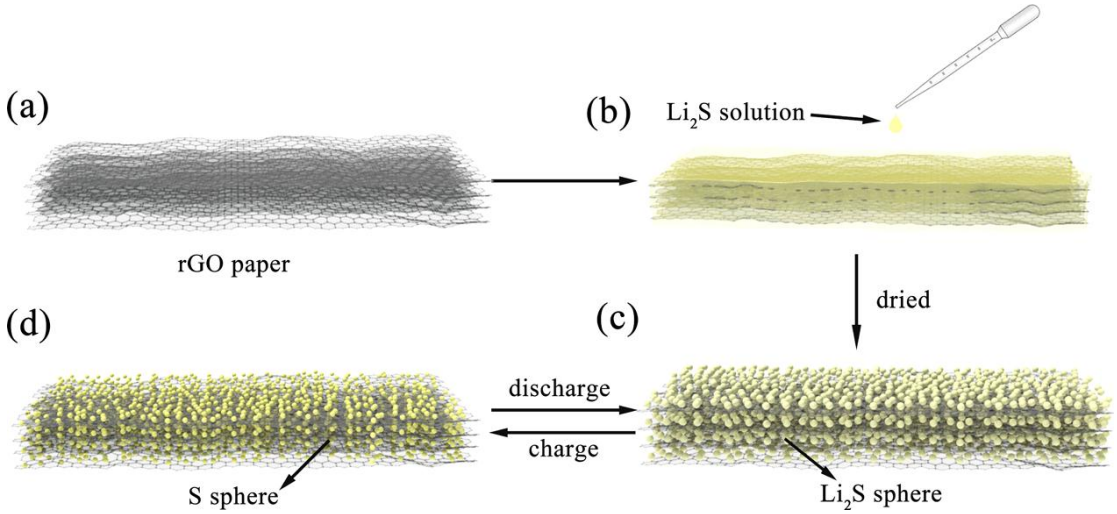

Figure 2.9 Schematic illustration of the material preparation processes of the nano-Li_2S/rGO paper and structure changes during cycling of nano-Li_2S/rGO paper. (a) The rGO paper was obtained by freeze-drying of GO suspension in water at -50 ℃ first and then reduced by heat treatment under 5% H_2/Ar atmosphere, and the rGO paper is flexible and has good in-plane electrical conductivity (3.07 × 104 S/m). (b) Drop coating of the rGO paper by the solution of Li_2S in anhydrous ethanol in the glovebox. Moisture and oxygen in the glovebox were less than 1 ppm. (c) The final product, nano-Li_2S/rGO paper, after removing the free and crystallized ethanol by vacuum heating at 300 ℃ for 2 h. Li_2S particles were uniformly distributed throughout the rGO paper. (d) Schematic shows the possible charge situation of the nano-Li_2S/rGO paper; sulfur is smaller than Li_2S [90].

2.3.3 Electrolyte

Another important component in the lithium sulfur batteries is the electrolyte, since the electrolyte acts as the ion transport pathway in the cell system. Various kinds of electrolytes, including carbonates, ether, ionic liquids, and sulfone with different viscosities, have been widely used to enhance the electrochemical performance of the sulfur electrodes. Generally, ether solvents, including 1,3-dioxolane (DOL), 1,2-dimethoxyethane (DME) [95], and tetra(ethylene glycol) dimethyl ether (TEGDME) [96], have a series of advantages, such as the higher solubility of polysulfides, higher ionic conductivity and lower viscosity. In contrast, while carbonate based electrolytes commonly are not suitable for the Li-S batteries due to the nucleophilic attack on the carbonyl groups [97]. Chang et al. investigated a mixed electrolyte of TEGDME and DOL in a lithium-sulfur battery. The role of TEGDME is to readily solvate the lithium salt and DOL reduces the viscosity of the electrolyte. It was found that shorter polysulfides are preferentially formed in DOL electrolyte in the high discharge voltage plateau, while the sulfur utilization in the lower discharge voltage plateau is determined by the conductivity and viscosity of the electrolyte. [98]

In addition, the most common electrolyte additive widely used in Li-S batteries is $LiNO_3$ [99, 100]. The addition of $LiNO_3$ is conducive to the formation of a protective film on the surface of the lithium anode. This passivation layer could effectively slow down the reduction of polysulfides, which means that the polysulfides in the electrolyte were successfully prevented from coming into direct contact with the lithium by the protective film, resulting in higher Coulombic efficiency.

Using ionic liquid as electrolyte is another research direction. This is because polysulfide species are less insoluble in ionic liquid, providing a new approach to suppressing the shuttle effect. Nevertheless, the application of ionic liquid electrolytes is limited because of their drawbacks, such as high viscosity and lower electrode wettability, as well as high cost. On the other hand, the use of solid-state electrolyte is the only strategy to completely avoid the shuttle effect of polysulfides. Nagata et al. [101] reported all-solid-state lithium-sulfur batteries obtained by using activated-carbon-based composite as cathode, delivering a high reversible capacity of 1600 mAh g^{-1} after 100 cycles at 1 C.

2.3.4 Binders

Binder, even though it is one of the most important components in the Li-S battery, is often overlooked. A suitable binder in the Li-S system should have mechanical stability to ensure good contact between the sulfur-based nanomaterial with conductive carbon and the current collector, and also could help to control polysulfide dissolution and diffusion.

Polyvinylidene fluoride (PVDF) is widely used as an important binder in Li-S batteries. Although it has relatively strong adhesion and can link the sulfur-based active material with the current collector, the polysulfide absorption capability is weak, resulting in poor cycling stability. Poly(ethylene oxide) (PEO) is one of the earliest alternative binders studied in lithium-sulfur batteries [102,103]. Cheon et al. [102] investigated the effects of preparation methods (ball milling and mechanical stirring) on the electrochemical performance of sulfur cathode for binders with

different contents of PEO. The morphology of PEO and the porosity in sulfur cathode are determined by the preparation method and influence the electrochemical performance. Lacey et al. studied the effects of a binder mixture of PEO and poly(vinylpyrrolidone) (PVP) on lithium-sulfur batteries. High reversible capacity of 800 mAh g^{-1} can be retained after 200 cycles at 1 C, which is attributed to the strong interaction between the binder and the intermediate polysulfides. Furthermore, water-soluble binders including gelatin have been used in lithium-sulfur batteries [104-106]. Sun et al. [105] investigated the structure and electrochemical performance of lithium-sulfur batteries using gelatin as binder. The results indicate that the gelatin binder has several functions in the sulfur cathode. It has the properties of strong adhesion and good dispersion, as well as electrochemical stability.

Recently, Li et al. [107] reported a low cost, nontoxic, and natural binder, namely, gum arabic (GA), for lithium-sulfur batteries. Compared to the conventional PVDF binder, the resulting sulfur cathode with GA binder delivers enhanced electrochemical performance in terms of both ion cycling and rate properties. The S@GA cathode (75%, sulfur content) retained high capacity of 841 mAh g^{-1} after 500 cycles at the current density of 0.2 C. The exceptional performance is attributed to several reasons. The good mechanical stability allows it to buffer the volume changes during the charge-discharge process and maintain the integrity of the whole electrode. On the other hand, the functional groups in the binder can form chemical bonds with polysulfide species and thus control them within the cathode area, minimizing the shuttle phenomenon.

2.3.5 Cell configuration

Recently, several novel configurations for Li-S cells have proved to be crucial for enhancing the electrochemical performance of Li-S batteries. These include the use of a conductive interlayer, porous current collectors, and sandwich structures.

Manthiram's group were the first to introduce the concept of inserting a bifunctional interlayer between the cathode and the separator to suppress the diffusion of polysulfides [108-110]. This novel design for the cell configuration can effectively decrease the resistance of the sulfur cathode as an upper current collector, since the inserted layer offers additional electron pathways covering the top surface of the cathode, enhancing its conductivity. Furthermore, the bifunctional interlayer could capture the migrating polysulfides, leading to improved long-term cycle stability. The inserted layer needs to possess suitable properties. Firstly, it must have a porous structure for immobilizing the active materials and limiting the soluble polysulfides that are shuttling into the electrolyte [111,112]. In addition, the interlayer must have high electrical conductivity. The conductive interlayer matrix should freely transport the electrons into the trapped polysulfides where they can react with them. Thirdly, the porous interlayer should consist of interwoven fibers or tubes, which can act as the host for accommodating and constraining the polysulfides by means of its high electrolyte absorptivity [108]. Thereafter, many advanced interlayers were fabricated from carbon nanotube, carbon nanofiber, graphene, and carbonized paper [113-116].

Besides interlayers, several advanced cell configurations have been used in lithium-sulfur batteries [117-121]. Manthiram's group reported a novel

sandwich-structured electrode architecture composed of a bifunctional interlayer on the top, the Li_2S powder in the middle and porous current collector at the bottom [117]. Excellent cycling performance can be obtained, which can be attributed to the unique sandwich structure, which not only facilitates the transport of ions and electrons, but also traps the soluble polysuifides products. They also reported a facile and unique layer-by-layer approach to achieving sulfur electrode with high-areal-capacity [118]. The electrode consists of commercial sulfur in the sulfur layers and porous carbon nanofibers in the carbon layers. The carbon layers act as current collectors to facilitate transport of electrons and improve the active materials utilization. This unique layer-by-layer cathode with high sulfur loading (11.4 mg cm^{-2}) and high sulfur content (56.3%) can deliver a high areal capacity of 11.4 mAh cm^{-2} at current density of 0.1 C, which is attributed to the stacked nanostructures and strong absorption properties of the carbon nanofiber paper. Xiao et al. [119] prepared a lightweight TiO_2/graphene layer directly coated on the sulfur cathode by doctor blade method. The TiO_2/graphene layer accounts for only 7.8 wt% of the whole electrode but plays an important role in improving the electrochemical performance of lithium-sulfur batteries. The light coating layer not only offers an additional electrically conductive network covering the whole cathode, but also acts as a physical barrier to trap intermediate polysulfdies. The addition of TiO_2 in the coating layer further constrains the dissolution of polysulfides in the electrolyte, thus greatly eliminating the shuttle effect. The cathode with a coated TiO_2/graphene layer delivered a high capacity of 1040 mAh g^{-1} after 300 cycles at 0.5 C. Zhou et al. [121]

developed a flexible integrated sulfur cathode, in which an integrated structure consisting of sulfur and graphene was directly coated on a polypropylene (PP) separator (Figure 2.10).

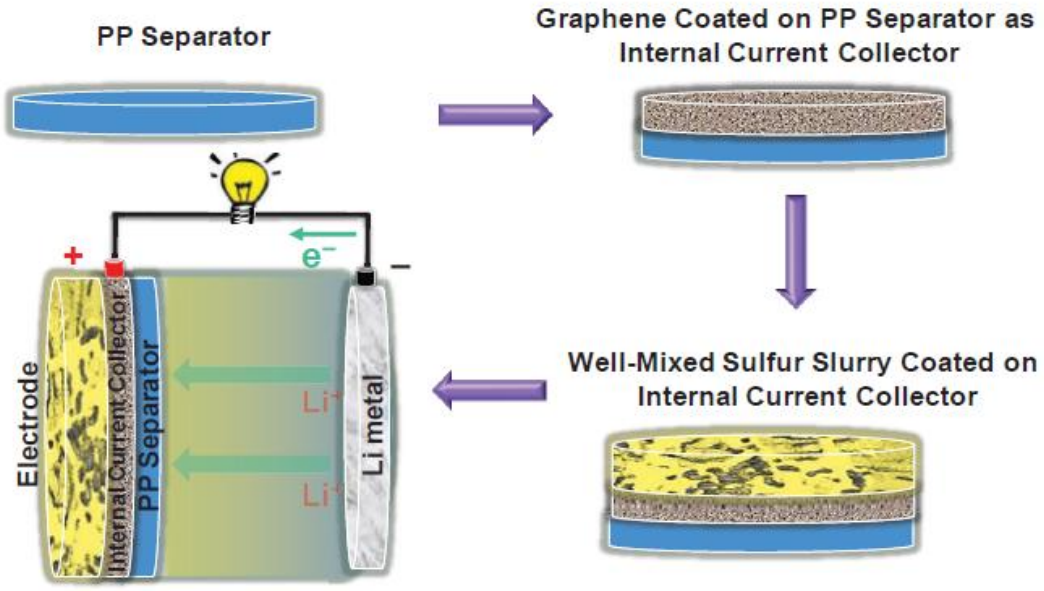

Figure 2.10 Schematic of the electrode confi guration using an integrated structure of sulfur and G@PP separator and the corresponding battery assembly [121].

The sulfur and graphene layers are directly coated on the separator without any need for Al foil as substrate, which can significantly reduce the weight of the whole electrode. Also, the excellent flexibility and high mechanical strength give the integrated electrode good flexibility and mechanical strength. More importantly, the graphene layer next to the separator can provide additional electron pathways and act as a good barrier to trap the dissolved intermediate polysulfides. The integrated electrode delivered 663 mAh g^{-1} after 500 cycles at current density of 1.5 A g^{-1} with a small capacity decay of 0.064% per cycle.

2.3.6 Functionalization of Separator

Another effective route to prevent the diffusion of polysulfides through the separator is to functionalize the separators in Li-S batteries. It is easy to realize by introduction of a coating layer on the cathode side of separator, such as with carbon-coated, polymer-coated, and ceramic-coated separator [122-130]. If the diffusion of polysulfides can be localized in the cathode region, the cycling stability and rate capability will be significantly improved.

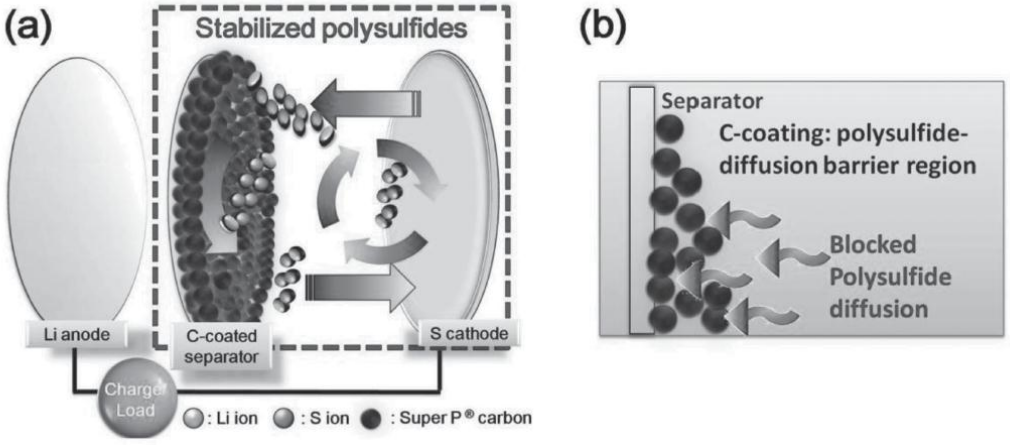

Figure 2.11 Schematic cell configuration modification of Li-S cells. a) Schematic configuration of a Li-S cell with the C-coated separator and b) the polysulfide-diffusion barrier region [122].

Chung et al. [122] prepared a Super P carbon coated separator for lithium-sulfur batteries through the tape-casting approach (Figure 2.11). Overall, the carbon coating layer on the separator plays two important roles. On the one hand, the conductive carbon coating layer can facilitate the transport of electrons as an upper current collector, which can decrease the internal charge transfer resistance and improve the utilization of sulfur. On the other hand, the carbon coating layer can suppress the

diffusion of polysulfides, confining the polysulfides within the cathode region and improving the cycling stability. Also, the cell employing the carbon-coated separator exhibited low self-discharge behaviour, as the carbon coating layer acts as a protective layer to prevent the dissolution of sulfur into the electrolyte during resting periods. Balach et al. [123] developed a functional mesoporous carbon-coated separator to achieve long-life and high-energy lithium-sulfur batteries. They used mesoporous carbon with high surface area (843 m^2 g^{-1}) to prepared the carbon-coated separator. As a result, the electrochemical performance of their lithium-sulfur batteries featured high capacity, long life, and good stability. It was also found that the thickness of the carbon coating layer on the separator is related to the electrochemical performance of the lithium-sulfur battery. Decreased thickness can reduce the sulfur content in the electrode but improve the capacity of the electrode.

Apart from porous carbon, polymer is also used for coating the separator. Chung et al. [124] developed a functional separator with a polyethylene glycol (PEG)-supported microporous carbon coating for lithium-sulfur batteries. The PEG polymer not only acts as a binder to improve the adhesion strength, but also can trap polysulfides by chemical interaction. The addition of microporous carbon serves as a physical barrier to further supress the diffusion of the polysulfides. Excellent electrochemical performance with high sulfur utilization (80%), long life (500 cycles), and a low decay rate (0.11% per cycle) can be obtained. Huang et al. [126] prepared a Nafion-coated separator, as Nafion film can allow the transport of Li^+ ions but prevent the transport of polysulfide species through the separator. The stability and coulombic

efficiency of lithium-sulfur batteries using the Nafion-coated separator were improved. The coated Nafion layer works as an electrostatic shield for polysulfides, preventing them from travelling across the separator. In this way, the shuttle effect can be greatly minimized. Stable cycling performance in lithium-sulfur batteries can be achieved, with a low decay rate of 0.08% per cycle. Zhang et al. [127] prepared Al_2O_3-coated separator for lithium-sulfur batteries. An Al_2O_3 coating layer serves as an absorbent layer to block the diffusion of polysulfides, decreasing the shuttle effect and loss of active materials. The as-prepared lithum-sulfur battery with Al_2O_3-coated separator exhibited enhanced electrochemical performance, delivering capacity of 593.4 mAh g^{-1} after 50 cycles, which is much better than for the cell with a conventional separator.

2.3.7 Modification of anode

Anode, as an essential part of the Li-S battery system, plays an important role in the long-term cycling stability of Li-S batteries. Metallic lithium is widely used as anode in Li-S batteries due to its high theoretical capacity (3860 mAh g^{-1}) and low potential. Nevertheless, metallic lithium is unstable in contact with organic electrolyte, leading to a safety issue for the rechargeable Li-S batteries. There are two basic feasible ways to address this problem. One is the utilization of protected lithium anode [131], and the other one is the preparation of alternative Li/M (M = Si, Sn, C, etc.) alloys [132-135].

2.3.8 Voltage window

Commonly, Li-S batteries are tested within the voltage range between 1.5 V and 3 V in order to utilize the full capacity generated by the chemical reaction from elemental sulfur to lithium sulfide. Su et al. [136] reported an applicable way to recharge lithium Li-S batteries by controlling the charging conditions, resulting in a tremendous improvement for various Li-S battery systems. High capacity and long-term cyclability can be obtained by charging the Li-S battery within the lower plateau capacity. A cut-off voltage shift from 1.5 to 1.8 V could avoid the irreversible capacity loss from the $LiNO_3$ additive, and the lower plateau near 2 V involves the reaction that directly forms insoluble Li_2S, which is confirmed by X-ray photoelectron spectroscopy (XPS) analysis. This novel recharge approach not only works well with Li-S cells with an interlayer configuration, but also with dissolved polysulfide systems, which can be widely applied within various kinds of electrodes and can advance the practical application of Li-S batteries for energy storage.

2.4 Lithium-selenium batteries

Selenium, as a similar group element to sulfur, has similar chemical behaviuor and could react with lithium to form selenides. Although selenium has lower theoretical gravimetric capacity of 675 mAh g^{-1} compared to sulfur electrode, its theoretical volumetric capacity (3253 mAh cm^{-3}) is comparable to that of sulfur (3467 mAh cm^{-3}) [137-140]. In addition, the electronic conductivity (1×10^{-3} S m^{-1})of selenium is much higher than that of sulfur [138]. All the features of Se make it a promising candidate cathode material in lithium-ion batteries as well as sodium-ion batteries. However, the

practical application of selenium cathodes also faces great challenges. The main issue is the dissolution problem of high-order polyselenides similar to sulfur, resulting in low utilization of selenium, low Coulombic efficiency of the selenium cathode, and fast capacity fading.

The methods to confine and stabilize sulfur should be useful for selenium as well, as selenium possesses similar chemical reaction with sulfur. Many strategies used in lithium-sulfur batteries have been extended to improve the electrochemical properties of selenium-based cathodes. Amine's group [138] firstly conducted work on Se/CNT composite as a cathode material, and as-prepared Se/CNT composite electrode delivered a capacity of 300 mAh g^{-1} after 100 cycles for lithium-selenium batteries. Afterwards, Guo et al. [139] synthesized Se/CMK-3 composite cathode by using a simple thermal-treatment method, exhibiting a reversible capacity of 600 mAh g^{-1} over 50 cycles. Wang et al. [140] synthesized a nano-Se_8-carbon composite (the content of selenium is 30%), and the obtained Se_8/C composite electrodes displayed superior electrochemical performance with a capacity of 480 mAh g^{-1} in lithium-selenium battery after 1000 cycles, and 340 mAh g^{-1} in sodium-selenium battery after 380 cycles. To date, most of research on selenium composite for energy storage has been focused on "physical" methods, confining the selenium active materials in a matrix to address the dissolution issue [138-143]. It is clear that using such so-called physical method to trap selenium within the porous substrates is an effective way to tackle the dissolution problem. On the other hand, "chemical" method involving functional groups and the unique chemical chain structure of

polymers may be a more efficient strategy to trap the selenium during charge-discharge process compared to the physical method, as it can yield excellent stability and activity [144-147]. Liu et al. [147] reported a novel selenium-carbon fiber composite as cathode for lithium-selenium batteries. After a heat treatment process, the selenium is converted to chainlike Se_n molecules, which can bond with the surfaces of carbon fibers. The selenium is uniformly distributed in the conductive carbon nanofiber matrix. The chemical bonding could also greatly supress the dissolution of intermediate polyselenides. The obtained selenium-carbon composite delivered a high reversible capacity of 400 mA g^{-1} after 2000 cycles at 1 C.

2.5 References

[1] S. G. Zhang, K. Ueno, K. Dokko, M. Watanabe, Advanced Energy Materials, 5 (2015) 1500117.

[2] Y. Yang, G. Y. Zheng, Y. Cui, Chemical Society Review, 42 (2013) 3018-3032.

[3] K. H. Seng, L. Li, D. P. Chen, Z. X. Chen, X. L. Wang, H. K. Liu, Z. P. Guo, Energy, 58 (2013) 707-713.

[4] S. E. Cheon, S. S. Choi, J. S. Han, Y. S. Choi, B. H. Jung, H. S. Lim, Journal of the Electrochemical Society, 151 (2004) A2067-A2073.

[5] R. Xiong, F. C. Sun, H. W. He, T. D. Nguyen, Energy, 63 (2013) 295-308.

[6] J. Shim, K. A. Striebel, E. J. Cairns, Journal of the Electrochemical Society, 149 (2002) A1321-A1325.

[7] L. X. Yuan, H. P. Yuan, X. P. Qiu, L. Q. Chen, W. T. Zhu, Journal of Power Sources, 189 (2009) 1141-1146.

[8] A. Manthiram Y. Z. Fu, S.H. Chung, C.X. Zu, Y.S. Su, Chemical Reviews, 114 (2014) 11751-11787.

[9] Y. V. Mikhaylik, J. R. Akridge, Journal of the Electrochemical Society, 151 (2004) A1969-A1976.

[10] D. Herbert, J. Ulam, U.S. Patent, (1962) 3043, 896.

[11] P. G. Bruce, S. A. Freunberger, L. J. Hardwick, J. M. Tarascon, Nature Materials, 11 (2012) 19-29.

[12] Y. S. Su, Y. Z. Fu, B. Guo, S. Dai, A. Manthiram , Chemistry − A European Journal, 19 (2013) 8621-8626.

[13] S. Y. Zheng, Y. Chen, Y. H. Xu, F. Yi, Y. J. Zhu, Y. H. Liu, J. H. Yang, C. S. Wang, ACS Nano, 7 (2013) 10995-11003.

[14] S. Xin, L. Gu, N. H. Zhao, Y. X. Yin, L. J. Zhou, Y. G. Guo, Journal of the American Chemical Society, 134 (2012) 18510-18513.

[15] G. Y. Xu, B. Ding, L. F. Shen, P. Nie, J. P. Han, X. G. Zhang, Journal of Materials Chemistry A, 1 (2013) 4490-4496.

[16] L. H. Yu, N. Brun, K. Sakaushi, J. Eckert, M. M. Titirici, Carbon, 61 (2013) 245-253.

[17] M. S. Park, B. O. Jeong, T. J. Kim, S. Kim, K. Y. Kim, J. S. Yu, Y. Jung, Y. J. Kim, Carbon, 68 (2014) 265-272.

[18] M. Nagao, Y. Imade, H. Narisawa, R. Watanabe, T. Yokoi, T. Tatsumi, R. Kanno, Journal of Power Sources, 243 (2013) 60-64.

[19] T. Xu, J. X. Song, M. L. Gordin, H. Sohn, Z. X. Yu, S. R. Chen, D. H. Wang, ACS Applied Materials & Interfaces, 5 (2013) 11355-11362.

[20] C. D. Liang, N. J. Dudney, J. Y. Howe, Chemistry of Materials, 21 (2009) 4724-4730.

[21] X. L. Ji, K. T. Lee, L. F. Nazar, Nature Materials, 8 (2009) 500-506.

[22] J. L. Wang, L. Liu, Z. J. Ling, J. Yang, C. R. Wan, C. Y. Jiang, Electrochimica Acta, 48 (2003) 1861-1867.

[23] C. F. Zhang, H. B. Wu, C. Yuan, Z. P. Guo, X. W. Lou, Angewandte Chemie International Edition, 51 (2012) 9592-9595.

[24] N. Jayaprakash, J. Shen, S. S. Moganty, A. Corona, L. A. Archer, Angewandte Chemie International Edition, 50 (2011) 5904-5908.

[25] N. Brun, K. Sakaushi, L. H. Yu, L. Giebeler, J. Eckert, M. M. Titirici, Physical Chemistry Chemical Physics, 15 (2013) 6080-6087.

[26] C. Wang, H. Chen, W. Dong, J. Ge, W. Lu, X. Wu, Chemical Communications, 50 (2014) 1202-1204.

[27] F. Bottger-Hiller, P. Kempe, G. Cox, A. Panchenko, N. Janssen, A. Petzold, Angewandte Chemie International Edition, 52 (2013) 6088–6091.

[28] S. C. Han, M. S. Song, H. Lee, H. S. Kim, H. J. Ahn, J. Y. Lee, Journal of the Electrochemical Society, 150 (2003) A889-A893.

[29] L. Ma, H. L. L. Zhuang, S. Y. Wei, K. E. Hendrickson, M. S. Kim, G. Cohn, R. G. Hennig, L. A. Archer, ACS Nano, 10 (2016) 1050-1059.

[30] F. Wu, J. Chen, L. Li, T. Zhao, R. Chen, The Journal of Physical Chemistry C, 115 (2011) 24411-24417.

[31] Z. Yuan, H. J. Peng, J. Q. Huang, X. Y. Liu, D. W. Wang, X. B. Cheng, Advanced Functional Materials, 24 (2014) 6105-6112.

[32] Y. C. Jeong, K. Lee, T. Kim, J. H. Kim, J. Park, Y. S. Cho, S. J. Yang, C. R. Park, Journal of Materials Chemistry A, 4 (2016) 819-826.

[33] X. Fang , W. Weng , J. Ren, H. S. Peng, Advanced Materials, 28 (2016) 491-496.

[34] Z. Li, Y. M. Huang, L. X. Yuan, Z. X. Hao, Y. H. Huang, Carbon, 2 (2015) 41-63.

[35] X. M. Ye, J. Ma, Y. S. Hu, H. Y. Wei, F. F. Ye, Journal of Materials Chemistry A, 4 (2016) 775-780.

[36] F. Y. Jin, S. Xiao, L. J. Lu, Y. Wang, Nano Letters, 16 (2016) 440-447.

[37] Z. A. Zhang, Q. Li, S. F. Jiang, K Zhang, Y. Q. Lai, J. Li, Chemistry − A European Journal, 21 (2015), 1343-1349.

[38] Y. H. Wu, M. X. Gao, X. Li, Y. F. Liu, H. G Pan, Journal of Alloys and Compounds, 608 (2014) 220–228.

[39] S. H. Chung, P. Han, R. Singhal, V. Kalra, A. Manthiram, Advanced Energy Materials, 5 (2015) 1500738.

[40] Z. A. Zhang, Q. Li, Y. Q. Lai, J. Li, The Journal of Physical Chemistry C, 118 (2014) 13369−13376.

[41] Q. Li, Z. Zhang, K. Zhang, J. Fang, Y. Q. Lai, J. Li, Journal of Power Sources, 256 (2014) 137-144.

[42] L. W. Ji, M. M. Rao, S. Aloni, L. Wang, E. J. Cairns, Y. G. Zhang, Energy & Environmental Science, 4 (2011) 5053-5059.

[43] M. Rao, X. Song, E. J. Cairns, Journal of Power Sources, 205 (2012) 474-478.

[44] J. Guo, Y. Xu, C. Wang, Nano Letters, 11 (2011) 4288-4294.

[45] A. K. Geim, K. S. Novoselov, Nature Materials, 6 (2007) 183-191.

[46] H. Wang, H. S. Casalongue, Y. Liang, H. Dai, Journal of the American Chemical Society, 132 (2010) 7472-7477.

[47] H. Kim, S.-W. Kim, Y. U. Park, H. Gwon, D. H. Seo, Y. Kim, K. Kang, Nano Research, 3 (2010) 813-821.

[48] D. Wang, D. Choi, J. Li, Z. Yang, Z. Nie, R. Kou, D. Hu, C. Wang, L. V. Saraf, J. Zhang, I. A. Aksay, J. Liu, ACS Nano, 3 (2009) 907-914.

[49] J. Z. Wang, L. Lu, M. Choucair, J. A. Stride, X. Xu, H. K. Liu, Journal of Power Sources, 196 (2011) 7030-7034.

[50] Y. L. Cao, X. L. Li, I. A. Aksay, J. Lemmon, Z. Nie, Z. G. Yang, J. Liu, Physical Chemistry Chemical Physics, 13 (2011) 7660-7665.

[51] H. L. Wang, Y. Yang, Y. Y. Liang, J. T. Robinson, Y. G. Li, A. Jackson, Y. Cui, H. J. Dai, Nano Letters, 11 (2011) 2644-2647.

[52] L. W. Ji, M. M. Rao, H. M. Zheng, L. Zhang, Y. C. Li, W. H. Duan, J. H. Guo, E. J. Cairns, Y. G. Zhang, Journal of the American Chemical Society, 133 (2011) 18522-18525.

[53] F. F. Zhang, X. B. Zhang, Y. H. Dong, L. M. Wang, Journal of Materials Chemistry A, 22 (2012) 11452-11454.

[54] L. Zhang, L. W. Ji, P. A. Glans, Y. G. Zhang, J. F. Zhu, J. H. Guo, Physical Chemistry Chemical Physics, 14 (2012) 13670-13675.

[55] M. Q. Zhao, Q. Zhang, J. Q. Huang, G. L. Tian, H. J. Peng, F. Wei, Nature Communications, 5 (2014) 3410.

[56] L. L. Qiu, S. C. Zhang, L. Zhang, M. M. Sun, W. K. Wang, Electrochimica Acta, 55 (2010) 4632-4636.

[57] F. Wu, J. Z. Chen, R. J. Chen, S. X. Wu, L. Li, S. Chen, T. Zhao, The Journal of Physical Chemistry C, 115 (2011) 6057-6063.

[58] M. M. Sun, S. C. Zhang, T. Jiang, L. Zhang, J. H. Yu, Electrochemistry Communications, 10 (2008) 1819-1822.

[59] J. Wang, J. Chen, K. Konstantinov, L. Zhao, S. H. Ng, G. X. Wang, Z. P. Guo, H. K. Liu, Electrochimica Acta, 51 (2006) 4634-4638.

[60] L. Xiao, Y. Cao, J. Xiao, B. Schwenzer, M. H. Engelhard, L. V. Saraf, Z. Nie, G. J. Exarhos, J. Liu, Advanced Materials, 24 (2012) 1176-1181.

[61] J. L. Wang, J. Yang, J. Y. Xie, N. X. Xu, Advanced Materials, 14 (2002) 963-965.

[62] H. Hu, H. Y. Cheng, Z. F. Liu, G. J. Li, Q. C. Zhu, Y. Yu, Nano Letters, 15 (2015) 5116-5123.

[63] J. Ye, F. He, J. Nie, Y. L. Cao, H. X. Yang, X. P. Ai, Journal of Materials Chemistry A, 3 (2015) 7406-7412.

[64] A. Konarov, D. Gosselink, TNL. Doan, Y. G. Zhang, Y. Zhao, P. Chen, Journal of Power Sources, 259 (2014) 183-187.

[65] Y. Z. Zhang, S. Liu, G. C. Li, G. R. Li, X. P. Gao, Journal of Materials Chemistry A, 2 (2014) 4652-4659.

[66] S. Y. Wei, L. Ma, K. E. Hendrickson, Z. Y. Tu, L. A. Archer, Journal of the American Chemical Society, 137 (2015) 12143-12152.

[67] J. Wang, J. Yang, C. Wan, K. Du, J. Xie, N. Xu, Advanced Functional Materials, 13 (2003) 487-492.

[68] M. S. Song, S. C. Han, H. S. Kim, J. H. Kim, K. T. Kim, Y. M. Kang, H. J. Ahn, S. X. Dou, J. J. Lee, Journal of the Electrochemical Society, 151 (2004) A791-A795.

[69] Y. J. Choi, B. S. Jung, D. J. Lee, J. H. Jeong, K. W. Kim, H. J. Ahn, K. K. Cho, H. B. Gu, Physica Scripta, 129 (2007) 62-65.

[70] Y. G. Zhang, Y. Zhao, A. Yermukhambetova, Z. Bakenov, P. J. Chen, Journal of Materials Chemistry A, 1 (2013) 295-301.

[71] Q. Pang, D. Kundu, M. Cuisinier, L. F. Nazar, Nature Communications, 5 (2014) 4759.

[72] X. Liang, C. Hart, Q. Pang, A. Garsuch, T. Weiss, L. F. Nazar, Nature Communications, 6 (2015) 5682.

[73] J. Jiang, J. H. Zhu, W. Ai, X. L. Wang, Y. L. Wang, C. J. Zou, W. Huang, T. Yu, Nature Communications, 6 (2015) 8622.

[74] Z. W. Seh, W. Y. Li, J. J. Cha, G. Y. Zheng, Y. Yang, M. T. Mcdowell, P. C. Hsu, Y. Cui, Nature Communications, 4 (2013) 1331.

[75] H. Kim, J. T. Lee, D. C. Lee, A. Magasinski, W. Cho, G. Yushin, Advanced Energy Materials, 3 (2013) 1308-1315.

[76] K. T. Lee, R. Black, T. Yim, X. L. Ji, L. F. Nazar, Advanced Energy Materials, 2 (2012) 1490-1496.

[77] F. X. Wu, J. T. Lee, E. B. Zhao, B. Zhang, G. Yushin, ACS Nano, 10 (2016) 1333-1340.

[78] J. Hassoun, B. Scrosati, Angewandte Chemie International Edition, 49 (2010) 2371-2374.

[79] J. Hassoun, J. Kim, D. J. Lee, H. G. Jung, S. M. Lee, Y. K. Sun, B. Scrosati, Journal of Power Sources, 202 (2012) 308-313.

[80] K. Cai, M. K. Song, E. J. Cairns, Y. Zhang, Nano Letters, 12 (2012) 6474-6479.

[81] C. Y. Nan, Z. Lin, H. G. Liao, M. K. Song, Y.D. Li, E. J. Cairns, Journal of the American Chemical Society, 136 (2014) 4659-4663.

[82] Y. Hwa, J. Zhao, E. J. Cairns, Nano Letters, 15 (2015) 3479-3486.

[83] Z. W. Seh, H. T. Wang, P. C. Hsu, Q. F. Zhang, W. Y. Li, G. Y. Zheng, H. B. Yao, Y. Cui, Energy & Environmental Science, 7 (2014) 672-676.

[84] L. Chen, Y. Z. Liu, F. Zhang, C. H. Liu, L. L. Shaw, ACS Applied Materials & Interfaces, 7 (2015) 25748-25756.

[85] Y. Yang, M. T. McDowell, A. Jackson, J. J. Cha, S. S. Hong, Y. Cui, Nano Letters, 10 (2010) 1486-1491.

[86] X. B. Meng, D. J. Comstock, T. T. Fister, J. W. Elam, ACS Nano, 8 (2014) 10963-10972.

[87] J. C. Guo, Z. C. Yang, Y. C. Yu, H. D. Abruna, L. A. Archer, Journal of the American Chemical Society, 135 (2013) 763-767.

[88] Z. W. Seh, J. H. Yu, W. Y. Li, P. C. Hsu, H. T. Wang, Y. M. Sun, H. B. Yao, Q. F. Zhang, Y. Cui, Nature Communications, 5 (2014) 5017.

[89] F. X. Wu, J. T. Lee, F. F. Fan, N. Nitta, H. Kim, T. Zhu, G. Yushin, Advanced Materials, 27 (2015) 5579-5586.

[90] C. Wang, X. S. Wang, Y. Yang, A. Kushima, J. T. Chen, Y. H. Huang, J. Li, Nano Letters, 15 (2015) 1796-1802.

[91] G. M. Zhou, E. Paek, G. S. Hwang, A. Manthiram, Advanced Energy Materials, 6 (2016) 1501355.

[92] M. Wu, Y. Cui, Y. Z. Fu, ACS Applied Materials & Interfaces, 7 (2015) 21479-21486.

[93] C. X. Zu, Y. Z. Fu, A. Manthiram, Journal of Materials Chemistry A, 1 (2013) 10362-10367.

[94] Y. Son, J. S. Lee, Y. Son, J. H. Jang, J. Cho, Advanced Energy Materials, 5 (2015) 1500110.

[95] W. K. Wang, Y. Wang, Y. Q. Huang, C. J. Huang, Z. B. Yu, H. Zhang, A. B. Wang, K. G. Yuan, Journal of Applied Electrochemistry, 40 (2010) 321-325.

[96] M. Agostini, S. Z. Xiong, A. Matic, J. Hassoun, Chemistry of Materials, 27 (2015) 4604-4611.

[97] J. Gao, M. A. Lowe, Y. Kiya, H. D. Abruna, The Journal of Physical Chemistry C, 115 (2011) 25132-25137.

[98] D. R. Chang, S. H. Lee, S. W. Kim, H. T. Kim, Journal of Power Sources, 112 (2002) 452-460.

[99] D. Aurbach, E. Pollak, R. Elazari, G. Salitra, C. S. Kelley, J. Affinito, Journal of the Electrochemical Society, 156 (2009) A694-A702.

[100] X. Liang, Z. Wen, Y. Liu, M. Wu, J. Jin, H. Zhang, X. Wu, Journal of Power Sources, 2011, 196, 9839-9843.

[101] H. Nagata, Y. Chikusa, Journal of Power Sources, 264 (2014) 206-210.

[102] S. E. Cheon, J. H. Cho, K. S. Ko, C. W. Kwon, D. R. Chang, H. T. Kim, S. W. Kim, Journal of the Electrochemical Society, 149 (2002) A1437-A1441.

[103] M. J. Lacey, F. Jeschull, K. Edstrom, D. Brandell, Journal of Power Sources, 264 (2014) 8-14.

[104] J. Sun, Y. Q. Huang, W. K. Wang, Z. B. Yu, A. B. Wang, K. G. Yuan, Electrochemistry Communications, 10 (2008) 930-933.

[105] J. Sun, Y. Q. Huang, W. K. Wang, Z. B. Yu, A. B. Wang, K. G. Yuan, Electrochimica Acta, 53 (2008) 7084-7088.

[106] J. L. Wang, Z. D. Yao, C. W. Monroe, J. Yang, Y. N. Nuli, Advanced Functional Materials, 23 (2013) 1194-1201.

[107] G. R. Li, M. Ling, Y. F. Ye, Z. P. Li, J. H. Guo, Y. F. Yao, J. F. Zhu, Z. Lin, S. Q. Zhang, Advanced Energy Materials, 5 (2015) 1500878.

[108] Y. S. Su, A. Manthiram, Chemical Communications. 48 (2012) 8817-8819.

[109] Y. S. Su, A. Manthiram, Nature Communications, 3 (2012) 1166.

[110] C. X. Zu, Y. S. Su, Y. Z. Fu, A. Manthiram, Physical Chemistry Chemical Physics, 15 (2013) 2291-2297.

[111] S. H. Chung, A. Manthiram, Advanced Materials, 26 (2014) 1360-1365.

[112] S. H. Chung, A. Manthiram. ChemSusChem, 7 (2014) 1655-1661.

[113] S. Y. Sheng, A. Manthiram, Chemical Communications, 48 (2012) 8817-8819.

[114] J. Q. Huang, B. A. Zhang, Z. L. Xu, S. Abouali, M. A. Garakani, J. Q. Huang, J. K. Kim, Journal of Power Sources, 285 (2015) 43-50.

[115] X. F. Wang, Z. X. Wang, L. Q. Chen, Journal of Power Sources, 242 (2013) 65-69.

[116] S. H. Chung, A. Manthiram, Chemical Communications, 50 (2014) 4184-4187.

[117] Y. Z. Fu, Y. S. Su, A. Manthiram, Advanced Energy Materials, 4 (2014) 1300655.

[118] L. Qie, A. Manthiram, Advanced Materials, 27 (2015) 1694-1700.

[119] Z. B. Xiao, Z. Yang, L. Wang, H. G. Nie, M. Zhong, Q. Q. Lai, X. J. Xu, L. J. Zhang, S. M. Huang, Advanced Materials, 27 (2015) 2891-2898.

[120] J. Fang, F. R. Qin, J. Li, W. W. Liu, M. R. Wang, F. Yu, L. Y. Zhang, Journal of Power Sources, 297 (2015) 265-270.

[121] G. M. Zhou, L. Li, D. W. Wang, X. Y. Shan, S. F. Pei, F. Li, H. M. Cheng, Advanced Materials, 27 (2015) 641-647.

[122] S. H. Chung, A. Manthiram, Advanced Functional Materials, 24 (2014) 5299-5306.

[123] J. Balach, T. Jaumann, M. Klose, S. Oswald, J. Eckert, Advanced Functional Materials, 25 (2015) 5285-5291.

[124] S. H. Chung, A. Manthiram, Advanced Materials, 26 (2014) 7352-7357.

[125] H. J. Peng, D. W. Wang, J. Q. Huang, X. B. Cheng, Z. Yuan, F. Wei, Q. Zhang, Advanced Science, (2015) 1500268.

[126] J. Q. Huang, Q. Zhang, H. J. Peng, X. Y. Liu, W. Z. Qian, F. Wei, Energy & Environmental Science, 7 (2014) 347-353.

[127] Z. Y. Zhang, Y. Q. Lai, Z. A. Zhang, K. Zhang, J. Li, Electrochimica Acta, 129 (2014) 55-61.

[128] Z. Y. Zhang, Y. Q. Lai, Z. A. Zhang, J. Li, Solid State Ionics, 278 (2015) 166-171.

[129] H. B. Yao, K. Yan, W. Y. Li, G. Y. Zheng, D. S. Kong, Z. W. Seh, V. K. Narasimhan, Z. Liang, Y. Cui, Energy & Environmental Science, 7 (2014) 3381-3390.

[130] Z. A. Zhang, Z. Y. Zhang, J. Li, Y. Q. Lai, Journal of Solid State Electrochemistry, 19 (2015) 1709-1715.

[131] J. Bruckner, S. Thieme, F. Bottger-Hiller, I. Bauer, H. T. Grossmann, P. Strubel, H. Althues, S. Spange, S. Kaskel, Advanced Functional Materials, 24 (2014) 1284-1289.

[132] N. Liu, L. B. Hu, M. T. McDowell, A. Jackson, Y. Cui, ACS Nano, 5 (2011) 6487-6493.

[133] D. Bresser, S. Passerini, B. Scrosati, Chemical Communications, 49 (2013) 10545-10562.

[134] S. Bourderau, T. Brousse, D. M. Schleich, Journal of Power Sources, 81 (1999) 233-236.

[135] H. Li, X. J. Huang, L. Q. Chen, Z. G. Wu, Y. Liang, Electrochemical and Solid State Letters, 2 (1999) 547-549.

[136] Y. S. Su, Y. Z. Fu, T. Cochell, A. Manthiram, Nature Communications, 4 (2013) 2985.

[137] Y. J. Cui, A. Abouimrane, J. Lu, T. Bolin, Y. Ren, W. Weng, C. J. Sun, V. A. Maroni, S. M. Heald, K. Amine, Journal of the American Chemical Society, 135 (2013) 8047-8056.

[138] A. Abouimrane, D. Dambournet, K. W. Chapman, P. J. Chupas, W. Weng, K. Amine, Journal of the American Chemical Society, 134 (2012) 4505-4508.

[139] C. P. Yang, S. Xin, Y. X. Yin, H. Ye, J. Zhang, Y. G. Guo, Angewandte Chemie International Edition, 52 (2013), 8363-8367.

[140] C. Luo, Y. H. Xu, Y. J. Zhu, Y. H. Liu, S.Y. Zheng, Y. Liu, A. Langrock, C. S. Wang, ACS Nano, 7 (2013) 8003-8010.

[141] L. L. Liu, Y. Y. Hou, X. W. Wu, S. Y. Xiao, Z. Chang, Y. Q. Yang, Y. P. Wu, Chemical Communications, 49 (2013) 11515-11517.

[142] L. L. Liu, Y. Y. Hou Y. Q. Yang, M. X. Li, X. W. Wang, Y. P. Wu, RSC Advances, 4 (2014) 9086-9091.

[143] S. F. Jiang, Z. A. Zhang, Y. Q. Lai, Y. H. Qu, X. W. Wang, J. Li, Journal of Power Sources, 267 (2014) 394-404.

[144] C. Luo, J. J. Wang, L. M. Suo, J. F. Mao, X. L. Fan, C. S. Wang, Journal of Materials Chemistry A, 3 (2015) 555-561.

[145] J. J. Zhang, Y. H. Xu, L. Fan, Y. C. Zhu, J. W. Liang, Y. T. Qian, Nano Energy, 13 (2015) 592-600.

[146] L. C. Zeng, X. Wei, J. Q. Wang, Y. Jiang, W. H. Li, Y. Yu, Journal of Power Sources, 281 (2015) 461-469.

[147] Y. X. Liu, L. Si, Y. C. Du, X. S. Zhou, Z. H. Dai, J. C. Bao, The Journal of Physical Chemistry C, 119 (2015) 27316-27321.

3 EXPERIMENT

3.1 Chemicals and materials

The chemicals and materials with detailed information used in this thesis are summarized in Table 3.1.

Table 3.1 Chemicals and materials used in this thesis.

Materials/Chemicals	Formula	Purity (%)	Supplier
Carbon black	C	Super P	Timcal, Belgium
Aluminium foil	Al	N/A	China
Polyvinylidene difluoride (PVDF)	$(CH_2CF_2)_n$	N/A	Sigma Aldrich, Australia
1-methyl-2-pyrrolidinone (NMP)	C_5H_9NO	99.5%	Sigma Aldrich, Australia
Ethanol	C_2H_5OH	99.95%	Sigma Aldrich, Australia
Lithium metal	Li	99.9%	Sigma Aldrich, Australia
Polypropylene separator	$(C_3H_6)n$	Celgard 2500	Hoechst Celanese Corporation
CR2032 type coin cells	N/A	N/A	China
1,3-dioxolane (DOL)	$C_3H_6O_2$	99.8%	Sigma Aldrich,

			Australia
Dimethoxyethane (DME)	$C_4H_{10}O_2$	99.5%	Sigma Aldrich, Australia
lithium bis(trifluoromethanesulfonyl)imide	$C_2F_6LiNO_4S_2$	99.9%	Sigma Aldrich, Australia
Lithium nitrate	$LiNO_3$	N/A	Sigma Aldrich, Australia
Sulfur	S	99.5%	Sigma Aldrich, Australia
Foam	N/A	N/A	Woolworth
Sodium hydroxide	NaOH	98%	Sigma Aldrich, Australia
Formalin solution	CH_3O	37%	Sigma Aldrich, Australia
Phenol	C_6H_5OH	99%	Sigma Aldrich, Australia
Hydrochloric acid	HCl	37%	Sigma Aldrich, Australia
Tetraethyl orthosilicate	$Si(OC_2H_5)_4$	99%	Sigma Aldrich,

			Australia
Pluronic F-127	$(C_3H_6OC_2H_4O)_x$	N/A	Sigma Aldrich, Australia
Cotton	N/A	N/A	Sigma Aldrich, Australia
Potassium hydroxide	KOH	98%	Sigma Aldrich, Australia
Ammonia hydroxide solution	NH_4OH	25%	Sigma Aldrich, Australia
Polyvinyl butyral (PVB)	$H_2(C_8H_{14}O_2)_n$	N/A	Sigma Aldrich, Australia
Urea	NH_2CONH_2	Bioreagent	Sigma Aldrich, Australia
N,N-dimethylformamide (DMF)	C_3H_7NO	99.8%	Sigma Aldrich, Australia
Selenium	Se	99.5%	Sigma Aldrich, Australia
Sodium perchlorate	$NaClO_4$	98%	Sigma Aldrich, Australia

Ethylene carbonate (EC)	$C_3H_4O_3$	99%	Sigma Aldrich, Australia
Diethyl carbonate (DEC)	$C_5H_{10}O_3$	99%	Sigma Aldrich, Australia
Polyacrylonitrile (PAN)	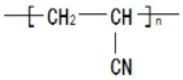	N/A	Sigma Aldrich, Australia
Lithium hexafluorophosphate	$LiPF_6$	99.99	Sigma Aldrich, Australia

3.2 Experimental procedure

In this research work, the overall experimental procedure mainly divided into two parts (described in Figure 3.1). The first part focused on the preparation and characterization of nanostructured active materials, including the synthesis method, and a series of physical and chemical techniques to identify the morphology, physical properties, and chemical structure of the as-prepared materials. The second part covers the application of the as-prepared active material in the lithium-sulfur batteries. After preparation of the electrodes by using these materials and assembling the coin-type cells, the electrochemical lithium storage properties were tested. Sometimes, in order to clearly understand the reasons for the enhanced electrochemical performance of the materials, the electrode materials were disassembled from the cycled coin cells, and then the morphology and structure were also investigated.

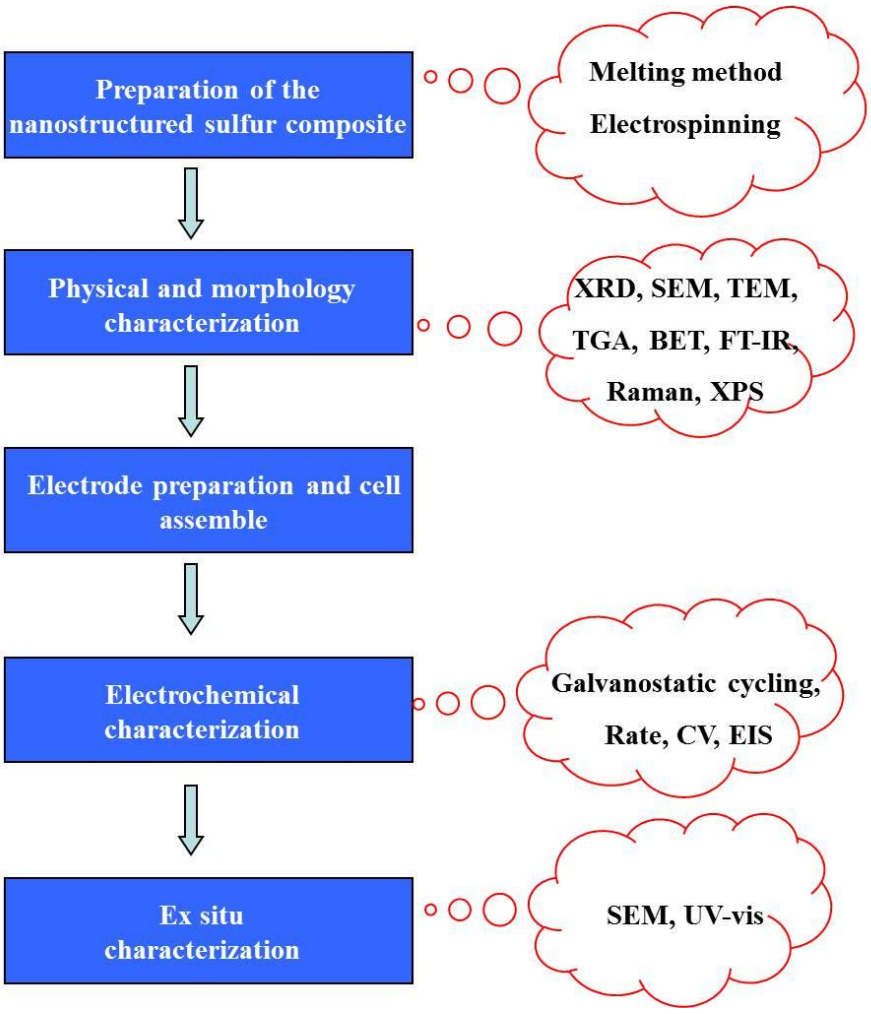

Figure 3.1 Outline of the experimental procedures.

3.3 Synthesis methods

The active materials used in this thesis were synthesized via the melting method and the electrospinning technique. The detailed information on these experimental procedures is given in the respective chapters.

3.3.1 Electrospinning technique

Electrospinning is regarded as an efficient technique for the fabrication of continuous fibres with diameters in the range of several nanometres to micrometres. Many kinds of fibrous materials have been successfully prepared by this method, including

polymers, polymer alloys, ceramics, and metals, as well as their composites. Electrospinning uses electric forces to draw charged threads of polymer solution or polymer melt into fibers. The process is particularly suited to the production of fibers with complicated molecules, because it does not require the use of coagulation chemistry or high temperature to produce solid threads from solution. A schematic illustration of the typical electrospinning set-up is presented in Figure 3.2, including the three main parts that are needed: the fiber precursor is firstly loaded into a syringe and pumped though a flow pump. When a sufficiently high voltage is applied to the spinnable solution, a droplet is formed on the tip of syringe, which can be further elongated due to electrostatic forces. Subsequently, solid nanofibers are formed by the evaporation of the solvent, which are collected on the collector substrate. There are various electrospinning technique parameters that could affect the morphology and diameter of the as-prepared fibers, including the viscosity, conductivity, and surface tension of the solution, the electrical potential, and the distance between the capillary and collection substrate, as well as the flow rate, needle gauge, temperature, and humidity. In this study, ordered mesoporous carbon fibers and organic selenium-containing carbon fibers were prepared by the electrospinning technique.

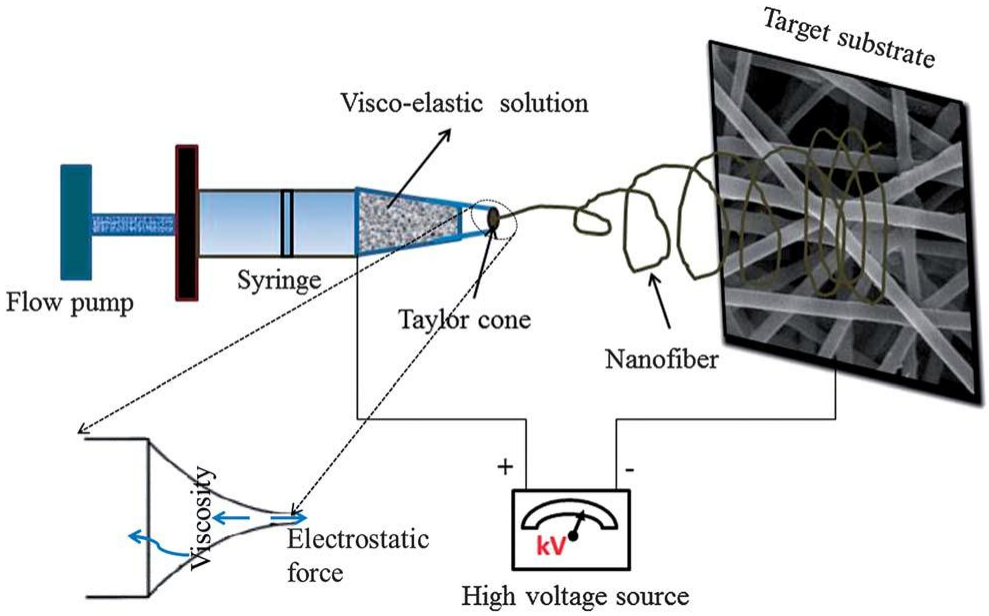

Figure 3.2 Schematic representation of the electrospinning process. [1]

3.3.2 Melting method

After preparing the porous carbon materials, the next experimental procedure is to encapsulate sulfur into the porous strcture. The melting method is the most widely used way to load sulfur into a nanostructured matrix to obtain sulfur composite for cathode materials. On heating the sulfur composite to around 160 ^{o}C (since the melting point of sulfur is around 115 ^{o}C) in a sealed device, the sulfur exists in form of a liquid and can diffuse into nanostructured carbon under capillary forces to yield a high-loading sulfur composite.

3.4 Physical and morphology characterization methods

3.4.1 X-ray Diffraction (XRD)

X-ray diffraction (XRD) is a powerful tool to investigate the structure of materials. The crystalline atoms cause a beam of X-rays to diffract into many specific directions. A three-dimensional picture of the density of electrons within the crystal can be

produced through measuring the angles and intensities of these diffracted beams, so the mean positions of the atoms in the crystal, the chemical bonds, and other information can be determined. X-rays can be regarded as waves of electromagnetic radiation, and crystals are regular arrays of atoms. A regular array of scatterers produces a regular array of spherical waves.

In the X-ray diffractometer, there is an anode (usually copper). The copper anode is irradiated with a beam of high-energy electrons that is accelerated by a high voltage electric field to a very high speed. A small Be window in the X-ray tube allows the X-rays to exit the tube with little attenuation, while maintaining the vacuum seal required for the X-ray tube operation. The scattering from all the different sets of planes results in a pattern unique to the crystal structure of a given compound. Bragg's law describes the diffraction condition from planes with spacing, d:

$n\lambda = 2d\sin\theta$ (3.1)

where n is an integer, λ is the wavelength of the incident X-ray beam, d is the distance between diffracting planes, and θ is the angle of incidence experienced by the X-ray beam reflection from the faces of the crystal.

The crystal sizes, D, of materials can also be calculated by using the Scherrer formula:

$$D = \frac{K\lambda}{\beta \cos\theta} \qquad (3.2)$$

where K is the shape factor of the average crystallite (typically around 0.9), λ is the X-ray wavelength, β is the half-peak width, and 2θ is the peak position ( ).

In this thesis, X-ray powder diffraction was carried out using a GBC MMA diffractometer and a Bruker D8-Advanced X-ray Diffractometer with Cu Kα radiation (λ = 1.5406 Å) in UOW.

3.4.2 Scanning electron microscopy (SEM)

The morphology of the as-prepared materials was observed with a scanning electron microscope (SEM), which can produce images of the sample by scanning it with a focused beam of electrons. Various signals containing information about the surface of the sample can be detected when electrons interact with atoms in the sample. The electron beam, which typically has an energy ranging from 0.2 to 40 keV, is focused by one or two condenser lenses to a spot about 0.4 nm to 5 nm in diameter. The electron beam is generally scanned in a raster scan pattern, and the beam's position is combined with the detected signal to produce an image. SEM can achieve a resolution better than 1 nanometer. A thin layer of gold or platinum is sputter-coated on the surfaces of the less conductive samples. The SEM used in this thesis is a field-emission JOEL 7500F.

3.4.3 Transmission electron microscopy (TEM)

Transmission electron microscopy (TEM) can be used to observe the morphology, crystal structure, and electronic structure through the signals which are produced from the interaction between the atoms of the sample and the electrons transmitted through the specimen. A beam of electrons is transmitted through an ultra-thin specimen,

interacting with the specimen as it passes through. TEM is capable of imaging at a significantly higher resolution than light microscopes due to the small de Broglie wavelength of electrons. Selected area electron diffraction (SAED) is a crystallographic experimental technique that can be conducted inside a transmission electron microscope, providing the crystallographic information from selected areas of the samples from 100 nm to the microscale. Furthermore, high resolution TEM (HRTEM) can supply images with atomic resolution, thus identifying lattice planes and defects of the samples. The TEM used in this thesis was a JEOL 2011 (200 keV).

3.4.4 Thermogravimetric Analysis (TGA)

Thermogravimetric analysis (TGA) is a method of thermal analysis that is performed on samples to determine their change in weight as function of temperature. It is used to analyse selected characteristics of materials through the mass loss or increase, such as decomposition, oxidation, vaporization, or sublimation. The testing environment is controlled by the purge gas (argon, air) that flow over the sample. In this doctoral work, TGA was used to determine the carbon contents in the carbon composite materials. TGA was carried out in a Shimadzu, a DRG-60 or a TA Instruments 2000 in flowing N_2 or in air. TGA was also used to determine the sulfur contents in the composite materials in this work with a TGA/differential scanning calorimetry (DSC) type instrument (METTLER TOLEDO, Switzerland) at a heating rate of 10 °C min^{-1} from room temperature to 500 °C under argon atmosphere.

3.4.5 Brunauer Emmett Teller (BET) technique

Brunauer Emmett Teller (BET) is an important analysis technique to measure the specific surface area of materials. BET analysis, including the specific surface area and the pore size distribution, is based on the theory of physical adsorption of gas molecules on a solid surface. The analysis process is conducted at liquid nitrogen temperature (77 K), and the samples should be degassed to remove H_2O and provide more accurate results before analysis. In this work, Brunauer Emmett Teller analysis was used to measure the surface area and pore size distribution of the as-prepared carbon, on a Quantachrome Instruments Autosorb AS-6B in NTU or a Quanta Chrome Nova 1000 in UOW in liquid nitrogen.

3.4.6 Raman spectroscopy

Raman spectroscopy is a spectroscopic technique for the study of the vibrational, rotational, and low frequency modes of a sample to identify the chemical bonds and symmetry of molecules. In a Raman spectrometer, laser light is used to interact with molecular vibrations, phonons, or other excitations, leading to the energy of some laser photons being shifted up or down. This shift can give information about the phonon modes in the system. In this work, Raman spectra were used to study the carbon-based sulfur composites and organic selenium composites by using a JOBIN YVON HR800 Raman Spectrometer with a 632.8 nm laser.

3.4.7 Fourier Transform Infrared Spectroscopy (FTIR)

Fourier Transform Infrared Spectroscopy (FTIR) is used to obtain an infrared absorption spectrum of a solid, liquid or gas by measuring how well a sample absorbs

light at each wavelength. FTIR spectrometers are mostly used for measurements in the mid and near IR regions, providing complementary information to Raman spectroscopy. In this work, FTIR spectroscopy was used to identify the form of selenium in the organic selenium-containing composite on a JASCO FT/IR-4100.

3.4.8 X-ray photoelectron spectroscopy (XPS)

X-ray photoelectron spectroscopy (XPS) is a surface-sensitive quantitative spectroscopic technique used to analyse the empirical formula, chemical states, and electronic states of the elements in the samples. XPS spectra are obtained bt irradiating the sample with a beam of X-rays and measuring the kinetic energy and number of electrons escaping from the top 0 to 10 nm of the sample. Usually, the samples are analysed under high vacuum (10^{-8} millibar). The information about elements is determined from the obtained spectra based on the characteristic binding energies associated with electrons in their orbitals.

3.4.9 Ultraviolet-visible spectroscopy (UV-Vis)

Ultraviolet-visible spectroscopy (UV-Vis) refers to absorption spectroscopy or reflectance spectroscopy in the ultraviolet-visible spectral region, which means that it uses light in the visible and adjacent ranges. UV-Vis spectroscopy is widely used in the analytical chemistry field, including for transition metal ions, biological macromolecules, and highly conjugated organic compounds. Spectroscopic analysis is commonly carried out in solution. In this thesis, the contents of polysulfides in the DOL/DME solutions in cells after different numbers of cycles were characterized

with a UV-3600 spectrophotometer (Shimadzu).

3.5 Electrochemical measurement methods

The electrochemical measurements of the nanostructured sulfur-based materials involve three parts: preparation of electrode, assembly of coin cells, and galvanostatic cycling in conjunction with cyclic voltammetry. .

3.5.1 Electrode preparation

Firstly, the nanostructured active materials were mixed with a conductive additive (carbon black, Super P), and a binder (polyvinylidene difluoride (PVDF)) in a certain ratio in N-methyl-2-pyrrolidinone (NMP) to form a homogeneous slurry. Then, the slurry was uniformly pasted onto an aluminum foil metallic substrate via the doctor blade technique. The thus-prepared working electrodes were dried in a vacuum oven at 60 ℃ for 24 hours. After drying, the electrode was pressed to improve the contact.

3.5.2 Cell assembly

The cell assembly was carried out in an Ar-filled glove box with both moisture and oxygen levels below 1 ppm. 2032-type coin cells were used in this thesis work. In a typical assembly procedure, the working electrode was placed at the positive cap, followed by porous polypropylene film as the separator, lithium foil as the counter electrode, a stainless steel spacer, a disk spring, and the negative cap. 4 drops of electrolyte were used to soak the electrodes and separator.

3.5.3 Galvanostatic electrochemical testing

The electrochemical performance, including the cycling performance at a constant current density and rate performance at different current densities, can be investigated by galvanostatic electrochemical testing. The charge or discharge capacity can be calculated based on the applied constant current and the total test time. Rate performance can also be obtained by varying the applied current. The instrument used in this work was a cell test instrument (CT2001A, LAND, China).

3.5.4 Cyclic voltammetry

Cyclic voltammetry (CV) is a type of potentiodynamic electrochemical measurement which can measure the current that is developed in an electrochemical cell under conditions where the voltage is in excess of that predicted by the Nernst equation. CV can be used to characterize redox reactions at electrodes in the cells. CV is performed by cycling the potential of a working electrode and detecting the resulting current. CV testing is based on the two-electrode model, in which lithium foil acts as reference electrode and counter electrode. The CV data were collected on a Biologic VMP3 electrochemical workstation with different scanning rates in the range from 0.1 to 0.8 $mV\ s^{-1}$.

3.5.5 Electrochemical Impedance Spectroscopy (EIS)

Electrochemical Impedance Spectroscopy (EIS) is an experimental method for characterizing the energy storage and dissipation properties of the electrochemical system. It works by recording the response of the system to a small applied perturbation over a predetermined frequency range. A common impedance spectrum

for active materials is composed of a low-frequency semicircle and a high-frequency linear tail, which are related to the kinetic processes from the charge transfer resistance and the double layer capacitance, and the solid-state diffusion of Li ions into the bulk of the active materials, respectively. In this thesis, EIS data were collected on a Biologic VMP3 electrochemical workstation.

3.6 Reference

[1] S. Kalluri, K. H. Seng, Z. P. Guo, H. K. Liu, S. X. Dou, RSC Advances, 3 (2013) 25576-25601.

4 TIO_2 COATED THREE-DIMENESIONAL HIERARCHICALLY ORDERED POROUS SULFUR ELECTRODE FOR THE LITHIUM/SULFUR RECHARGEBLE BATTERIES

4.1 Introduction

Rechargeable lithium ion batteries (LIBs) have achieved great development during the past decades as power sources for various portable devices such as laptops, smart phones and electric vehicles [1-4]. However, the specific energy of the commercialized lithium ion batteries will become insufficient for the future electric vehicles due to the low capacity of conventional electrode materials. Therefore, new electrode materials with higher gravimetric and volumetric capacity should be developed. Sulfur, as one of the most abundant elements on the earth, can offer ultra-high energy density (theoretically 2567 Wh kg^{-1}) and high theoretical specific capacity (1675 mAh g^{-1}), making it a very promising cathode candidate for the next generation batteries [5-8]. The Li-S battery system may suffer, however, from several disadvantages, including the low conductivity of sulfur and lithium sulfide [9] as well as the large volume changes of sulfur particles during charge and discharge processes. A more significant challenge that needs to be overcome is the high solubility of the intermediate lithium polysulfides in organic electrolytes. The soluble polysulfides can diffuse from the cathode and react with the lithium anode to generate insoluble lower-order polysulfides in the form of Li_2S or Li_2S_2, resulting in the precipitation of these species on the surface during cyclic processes [10,11]. These

issues lead to the low utilization of sulfur, which is the active material, low coulombic efficiency of the sulfur cathode, and fast capacity fading [12-15].

There are two basic strategies to address this problem in terms of designing nanostructured sulfur cathodes. One is to constrain the sulfur or lithium polysulfide within a framework by using host materials, such as various types of porous carbon [16,17], hollow carbon spheres [13,18], carbon nanotubes [19,20], graphene [21,22], graphene oxide [23,24], and conductive polymers [25,26]. An alternative route is to build a physical barrier to prevent soluble polysulfides from dissolving in the organic electrolyte by forming a thin film to acts as a coating on the surface of the active material. Such barrier materials include polymers [27,28] and metal oxides such as TiO_2 [29], Al_2O_3 [30], SiO_x, and VO_x [31]. Compared with a polymer coating, a metal oxide coating layer could almost completely block out-diffusion of the polysulfides and enhance the strength of the entire electrode to withstand structural damage during long cycle testing.

Herein, we employ 3D hierarchical porous carbon slice (C) as an improved confined matrix for high-level sulfur impregnation. 3D porous nanostructured carbon is highly desirable for high-performance electrode materials, as it can not only provide a continuous electron pathway to ensure good electrical contact, but also facilitates the transport of ions and electrolyte. Additionally, the well-developed 3D structure with macropores and ordered interconnected mesopores can encapsulate a large amount of sulfur, provide a large specific surface area, and facilitate fast ion transport, thus enhancing the electrochemical performance of electrodes. In order to trap the

dissolved polysulfides more effectively, a TiO_2 layer was further coated on the surface of the as-prepared porous carbon-sulfur composite to obtain carbon-sulfur-TiO_2 composite, as shown in Figure 4.1. The as-prepared TiO_2 coated carbon-sulfur composite slice could be used as cathode directly without further electrode preparation process, therefore, no inert weight, i.e. binders and metal substrate, is included in the electrodes.

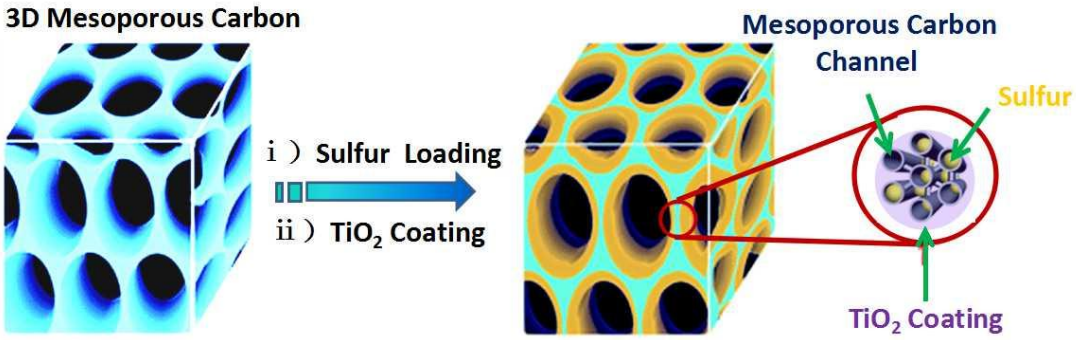

Figure 4.1 Pictorial representation of the structure of C-S-TiO_2 composite.

4.2 Experimental

4.2.1 Synthesis of hierarchical porous-structured carbon

The ordered mesoporous carbon-silica composite slice with macroporous architecture were synthesized through an evaporation-induced coating and self-assembly method using foam as template, as described by Zhao et al [32]. The foam was cut into thin slice to prepare carbon-silica composite slice. Afterwards, the obtained thin slice was put into boiling 2 mol L^{-1} NaOH solution for 2 h to remove the silica to obtain the hierarchical porous carbon slice.

4.2.2 Fabrication of TiO_2 coated porous carbon-sulfur composite electrodes

The as-prepared carbon slice and sulfur were mixed together in a weight ratio of 3:7 and heated to 160 ^oC in a sealed stainless steel autoclave for 24 h to facilitate sulfur diffusion into the carbon host. Then, the composite was heated at 200 ^oC and kept for 10 minutes under flowing argon gas (50 $cm^3 s^{-1}$) to vaporize the sulfur deposited on the outside surface of the composite (with the sample at this stage denoted as C-S). After that, titanium diisopropoxide bis(acetylacetonate) was used as the titanium precursor to coat a TiO_2 layer on the surface of the C-S composite slice according to a previous report [25] to obtain C-S-TiO_2 slice (denoted as C-S-TiO_2).

4.2.3 Characterization

The crystal phases of the resulting materials were analysed by powder X-ray diffraction (XRD, MMA GBC, Australia). Thermogravimetric analysis (TGA) was carried out to determine the sulfur content with a TGA/differential scanning calorimetry (DSC) type instrument (METTLER TOLEDO, Switzerland) at a heating rate of 10 ^oC min^{-1} from room temperature to 500 ^oC under argon atmosphere. The Brunauer–Emmett–Teller (BET) method was utilized to calculate the specific surface areas. The pore size distributions were derived from the adsorption branches of the isotherms based on the Barrett–Joyner–Halenda (BJH) model. The morphologies of the samples were investigated by field-emission scanning electron microscopy (FESEM; JEOL JSM-7500FA). Transmission electron microscope (TEM) images were collected on a JEOL 2011 200 kV instrument. X-ray photoelectron spectroscopy

(XPS) analysis was conducted on a VG Scientific ESCALAB 2201XL instrument using aluminium Kα X-ray radiation.

4.2.4 Electrochemical measurement

The C-S and C-S-TiO_2 composite thin slices can be as a binder-free electrode for lithium-sulfur batteries that does not require any current collectors. Coin-type (CR2032) cells were assembled in an argon-filled glove box. The electrolyte used was 1 M lithium bis(trifluoromethanesulfonyl)imide in a solvent mixture of 1,3-dioxolane (DOL): dimethoxyethane (DME) (1:1, v/v) containing $LiNO_3$ (1 wt%). The coin cells were galvanostatically charged-discharged between 1.5 and 3.0 V (vs. Li/Li^+) by using a cell test instrument (CT2001A, LAND, China).

4.3 Results and discussion

A scanning electron microscope (SEM) image in Figure 4.2 shows that the carbon slice is a 3D interconnecting network composed of prism-shaped struts with

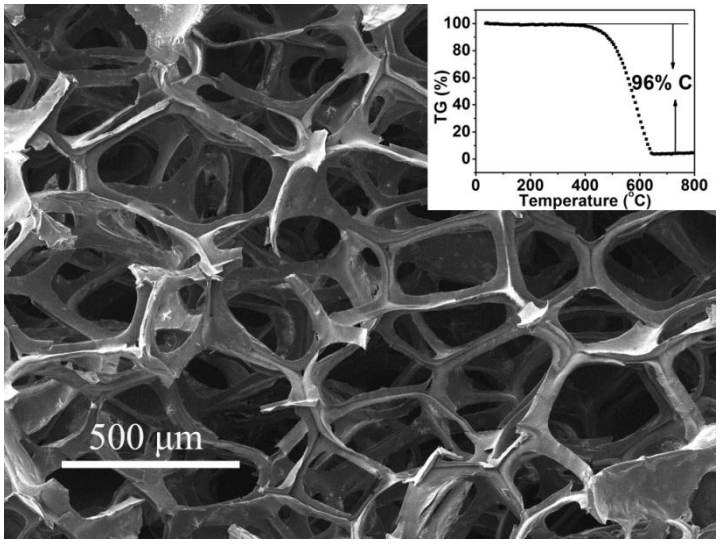

Figure 4.2 SEM image of as-prepared carbon. Inset shows the TG curve of C under air atmosphere to determine the content of carbon.

macropores about 300 μm in diameter. Thermogravimetric (TG) curves of the C (inset in Figure 4.2) displays a weight loss of 96 wt% from 400 to 650 °C, indicating that the content of carbon is up to 96% and nearly all the silica has been removed from the carbon-silica composite.

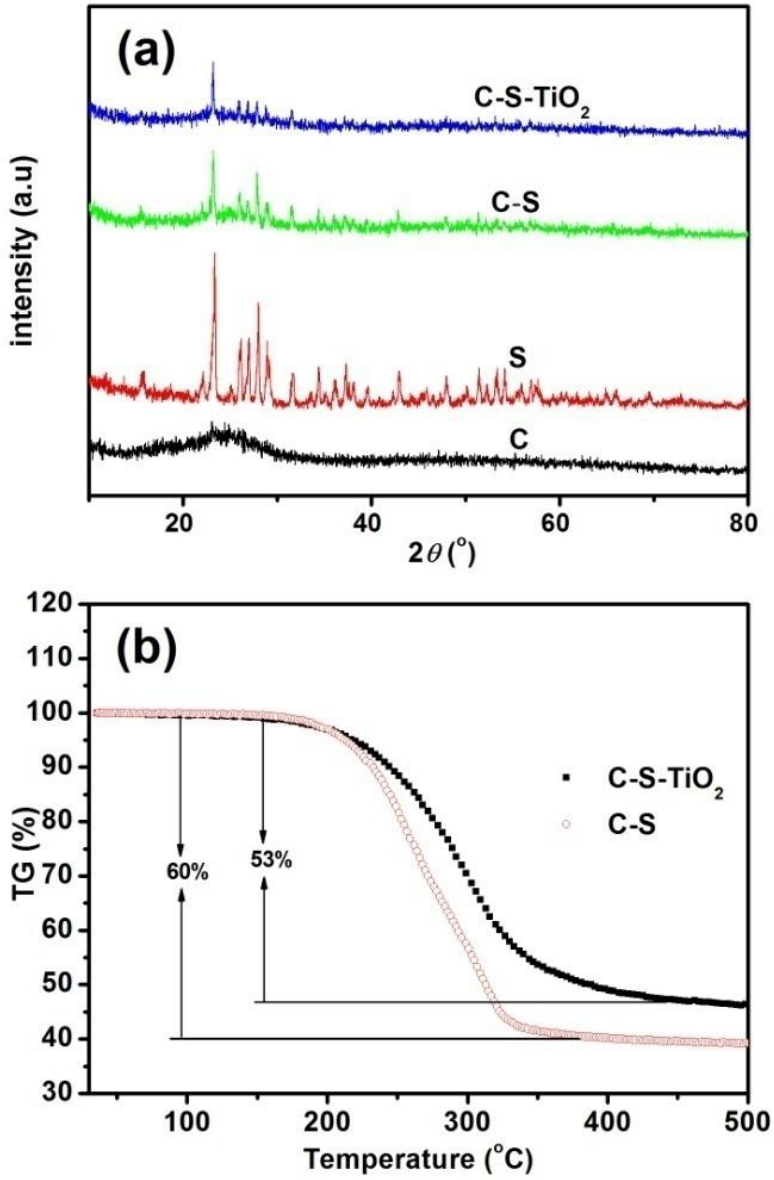

Figure 4.3 (a) XRD patterns of C, S, C-S, and C-S-TiO_2 composites, and (b) TG curves of C-S and C-S-TiO_2 composites under argon atmosphere.

As shown in Figure 4.3 (a), the X-ray diffraction (XRD) pattern of the carbon exhibits low-intensity and broad peaks, which reveal a typical amorphous structure. The pure elemental sulfur has various diffraction peaks, corresponding to an orthorhombic structure. As for the C-S and C-S-TiO_2 composites, some diffraction peaks of the elemental S are visible, although the intensities become distinctly lower and some diffraction peaks even disappear, which suggests good dispersion of the S within the mesoporous carbon hosts [33]. The sulfur content in the C-S and C-S-TiO_2 composites was determined by thermogravimetric analysis (TGA) conducted under argon atmosphere (as shown in Figure 4.3 (b)). The amount of sulfur in the C-S and C-S-TiO_2 composites is 60 wt% and 53 wt%, respectively.

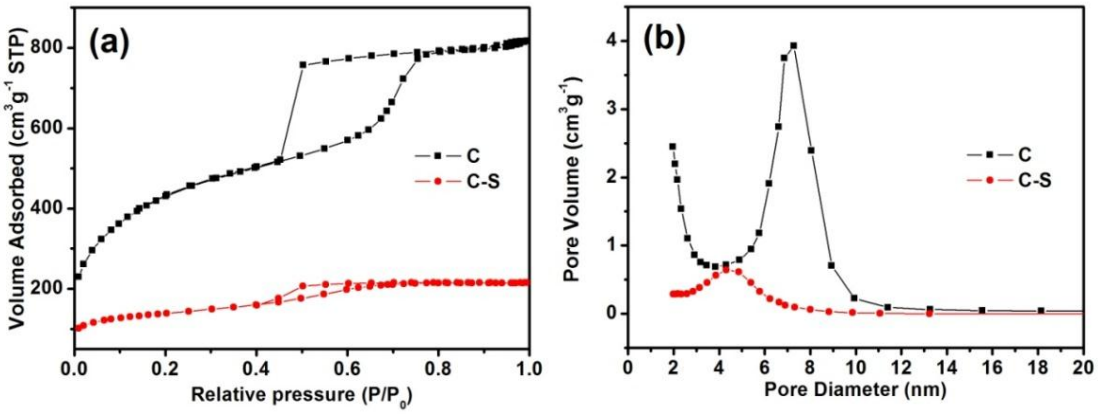

Figure 4.4 (a) N_2 sorption isotherms and (b) pore-size distributions of C and C-S composite.

The nitrogen adsorption-desorption isotherms of the C, C-S, and C-S-TiO_2 composites are shown in Figure 4.4 (a) to confirm the pore structures. The isotherms of C and the C-S composite are type IV isotherms with hysteresis at relative pressure above 0.4, which is characteristic of mesopores. Note that the insertion of sulfur leads to a

significant decrease in the pore volume (from 1.26 to 0.33 cm^3 g^{-1}) and Brunauer-Emmett-Teller (BET) surface area (1564 to 487 m^2 g^{-1} for C and C-S composite, respectively). Meanwhile, the pore size (Figure 4.4 (b)) also shows a strong decrease from 7 nm to 4.5 nm, suggesting that a large portion of the pores are filled with sulfur. The C-S-TiO_2 sample, however, does not exhibit a typical isotherm, indicating that the TiO_2 layer almost completely covers the surface of the C-S composite.

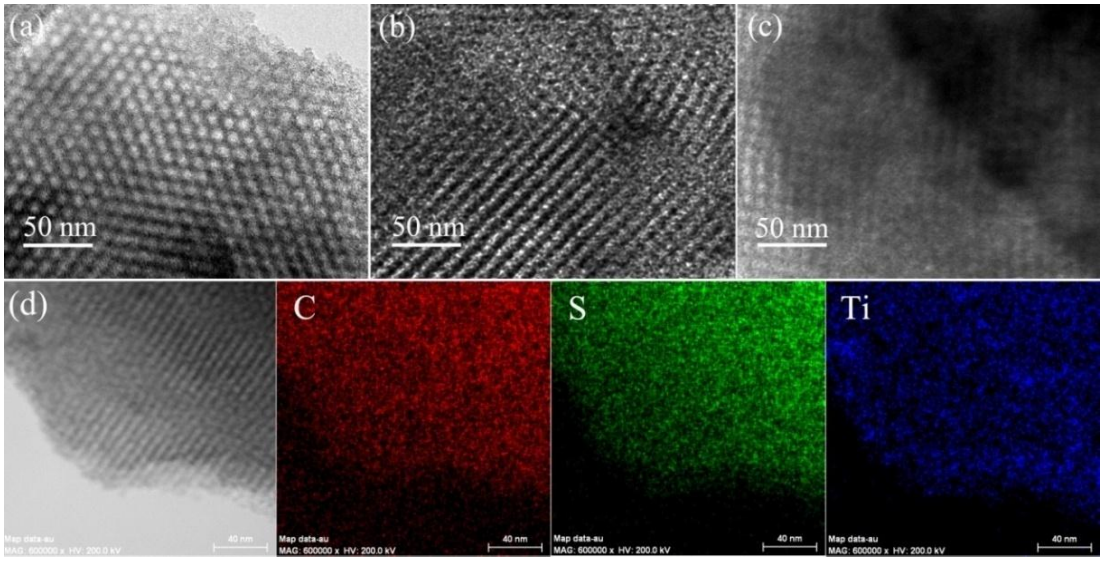

Figure 4.5 TEM images of (a) C, (b) C-S composite, (c) C-S-TiO_2 composite, and (d) STEM image of C-S-TiO_2 and corresponding elemental mapping images of C, S, and Ti.

Well-developed ordered mesostructure can be observed for the C sample, and the pore size estimated from the transmission electron microscope (TEM) image (Figure 4.5 (a)) is less than 8 nm, in good accordance with the value from the N_2 sorption isotherms. Moreover, compared to the C, the contrast and the pore size of the C-S composite are obviously decreased, and no significant amount of bulk sulfur on the

external surface is detected (Figure 4.5 (b)). This indicates that sulfur is homogeneously embedded in the mesopores of the sample due to the intense capillary forces. As for the C-S-TiO_2 composite, the mesopores are not as clear as those in the C and the C-S composite due to the TiO_2 coating on the surface of the C-S composite, resulting in a nearly complete lack of differentiation of the mesoporous composite (Figure 4.5 (c)). The scanning TEM (STEM) (Figure 4.5(d)) and corresponding elemental mapping images of the C-S-TiO_2 composite demonstrate that the TiO_2 coating layer is evenly distributed on the surface of the C-S composite, which is also in good agreement with the results from the N_2 sorption isotherms.

X-ray photoelectron spectroscopy (XPS) was used to further confirm and characterize the TiO_2 coating layer on the surface of the C-S composite electrode (as displayed in Figure 4.6). Three peaks positioned at 288.3, 284.9, and 283.7 eV are observed from the C1s spectrum, which could be attributed to the C=O, C-O, and C=C/C-C groups [34,35], respectively, indicating that C still retains some oxygen-containing groups from the carbonization process of the carbon precursor. The S $_{2p}$ spectrum exhibits two peaks at 164.8 and 163.7 eV, corresponding to the resolved S $_{2p1/2}$ and S $_{2p3/2}$ peaks. Additionally, two peaks at 460.8 and 454.8 eV corresponding to Ti $_{2p1/2}$ and Ti $_{2p3/2}$ are shown in the Ti $_{2p}$ spectrum, demonstrating the presence of Ti^{4+} [36]. As the penetration depth of XPS is about 10 nm, it is likely that the possible elemental sulfur signal is from places where the TiO_2 layer is thinner than 10 nm. The XPS results together with the TEM images and N_2 sorption isotherms results reveal that most of

the surface area of the C-S composite is covered with a TiO_2 layer less than 10 nm in thickness.

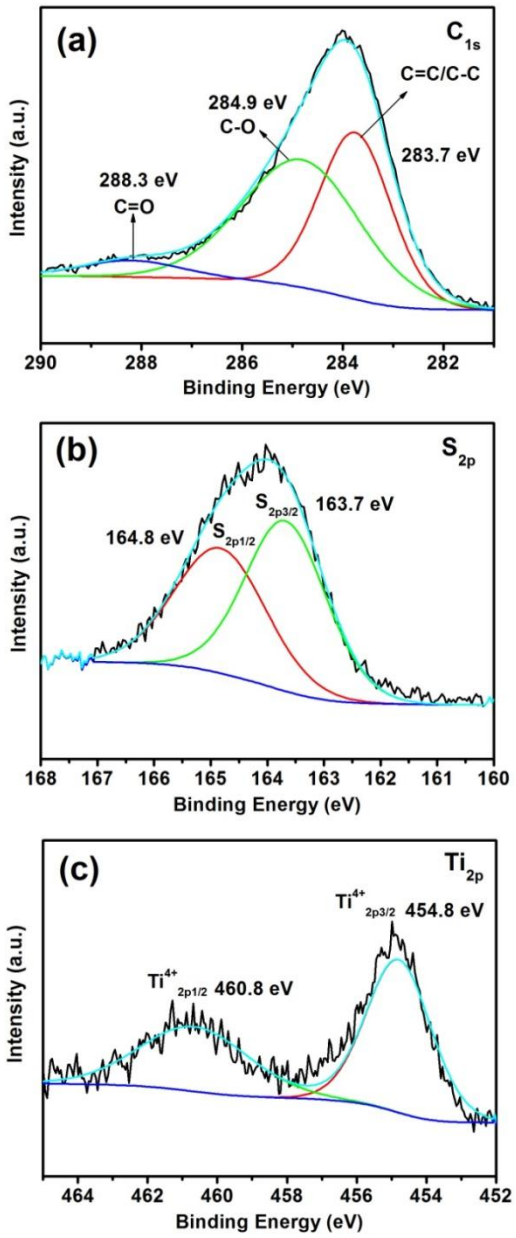

Figure 4.6 XPS spectra with fitting results of C-S-TiO_2 composite: (a) C $_{1s}$ spectrum, (b) S $_{2p}$ spectrum, (c) Ti $_{2p}$ spectrum.

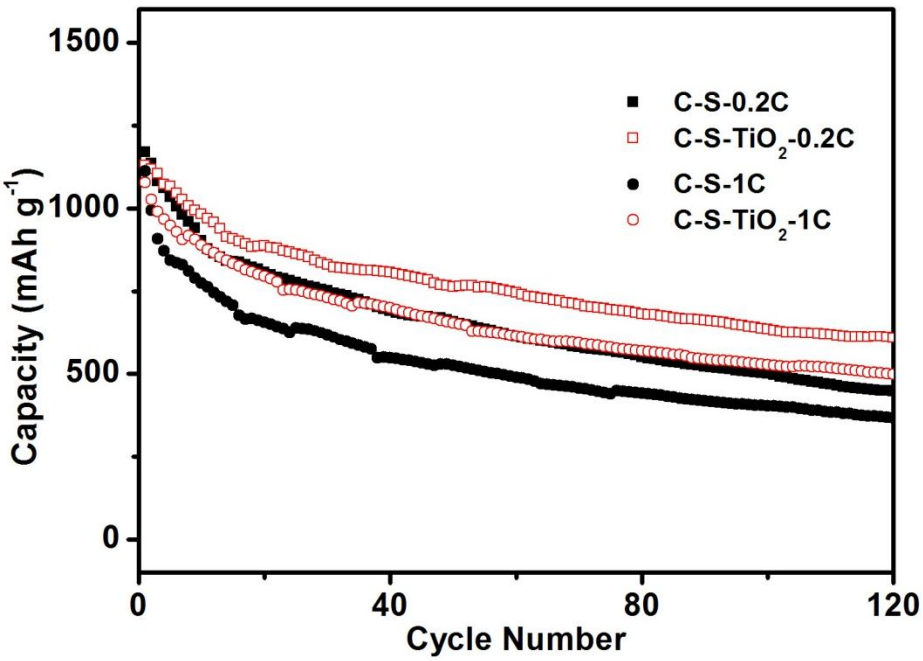

Figure 4.7 Cycling performances of C-S and C-S-TiO_2 electrodes at current densities of 0.2 C and 1 C

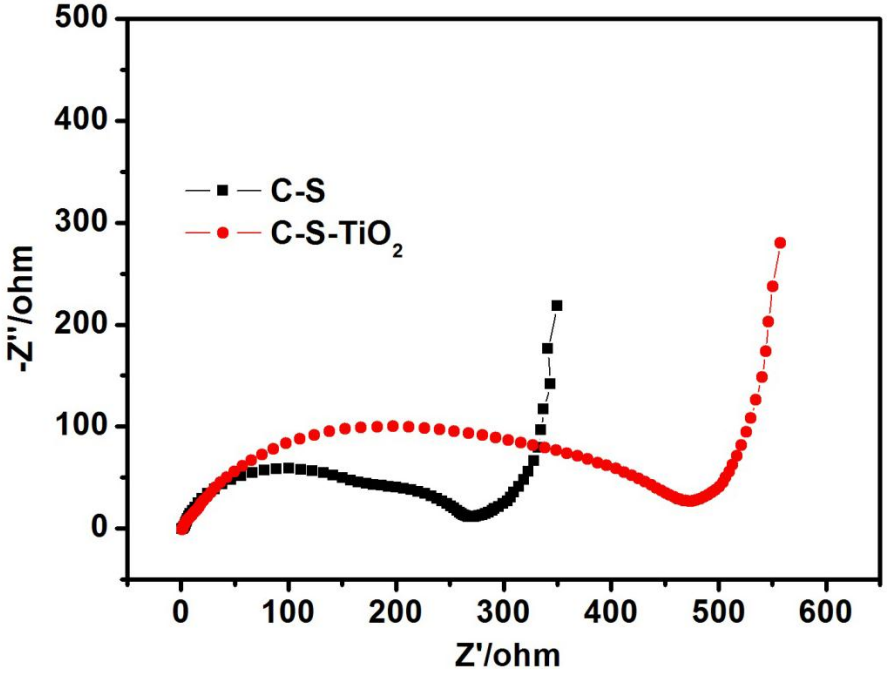

Figure 4.8 EIS spectra of C-S electrode and C-S-TiO_2 electrode for the first cycle.

The cycling performance of the C-S and the TiO_2 coated composite electrodes at current rates of 0.2 C and 1 C is shown in Figure 4.7. The initial discharge capacity is up to 1168 and 1111 mAh g^{-1} for the C-S composite cathode at the 0.2 C and 1 C rates, while the TiO_2 coated electrode delivers a corresponding discharge capacity of 1128 and 1076 mAh g^{-1}, respectively, which is slightly lower than for the C-S composite cathode due to the poor conductivity of the TiO_2 layer. This can be seen from the electrochemical impedance spectra (EIS) of the C-S and C-S-TiO_2 electrodes, as shown in Figure 4.8. The resistance of the C-S-TiO_2 electrode is much higher than that of the C-S electrode, resulting in lower initial discharge capacity. In contrast, it is obvious that the TiO_2 coated sample shows superior cycling performance in the long run. In the beginning, the capacities of the two samples are almost the same, however, the gap become more and more significant, especially after 20 cycles, as shown in Figure 4.7. The discharge capacity at the 120 th cycle can reach 608 mAh g^{-1} at 0.2 C and 500 mAh g^{-1} at the 1 C rate for the TiO_2 coated electrode, while the C-S composite cathode only exhibits corresponding capacities of 450 and 370 mAh g^{-1}, respectively. This means that the mesopores of C can trap the polysulfides for a short time, but only a real capping layer can confine the polysulfides in the carbon matrix over a long span of time. Another important aspect that contributes to the stable cycling performance is that the TiO_2 layer can effectively integrate the individual components in the electrode into a whole system and enhance the strength of the entire electrode to withstand structural damage during cycling. It is noted that specific capacity of the electrode without any binders and metal substrate in our study could

be comparable with that using binders and substrate in previous report [21, 23-25]. This suggests that the polysulfides are better trapped inside the carbon matrix due to the TiO_2 layer that is coated on the surface of the C-S composite. It should be noted that, after TiO_2 coating, the improvement on electrochemical performance is not significantly but moderate, which is caused by the poor electrical conductivity of the TiO_2. TiO_2 coating layer serves as as barrier to prevent the dissolution of polysulfides, however, the electrical conductivity of the TiO_2 coated cathode is lower. The poor conductivity of TiO_2, on the other hand, makes an adverse influence on the electrochemical performance of the electrode.

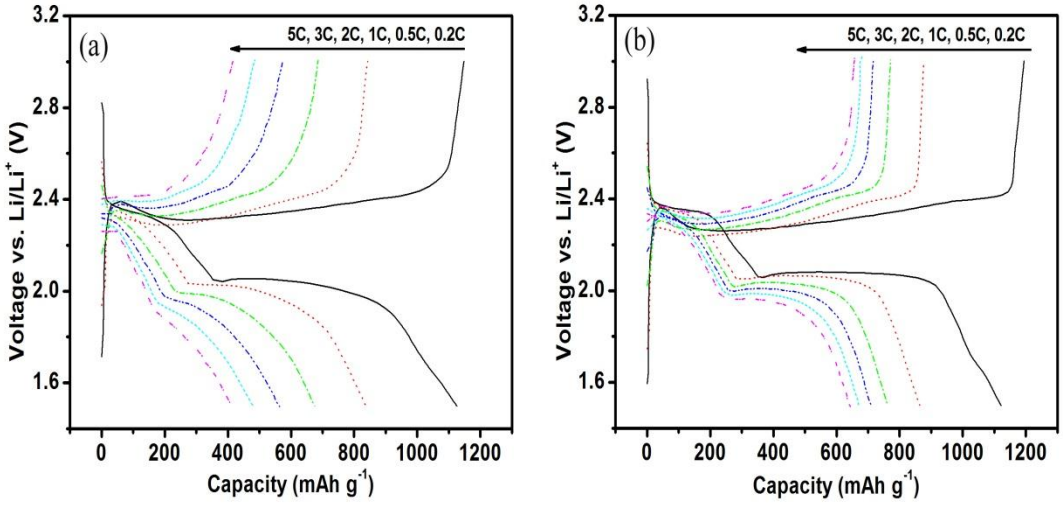

Figure 4.9 Discharge/charge voltage profiles of (a) C-S and (b) C-S-TiO_2 electrodes at various rates.

The rate capability of the C-S and the TiO_2 coated composite electrodes at different current rates, ranging from 0.2 C to 5 C, is shown in Figure 4.9. Compared with the C-S electrode, after TiO_2 coating, the rate performance is obviously improved, especially at high current rates. The discharge capacity at the second discharge cycle

for the C-S-TiO_2 composite cathode is 1142 mAh g^{-1} at the current rate of 0.2 C, which is slightly lower than that of the C-S composite. Nevertheless, the discharge capacity for the C-S-TiO_2 electrode remains as high as 889, 770, 714, 677, and 650 mAh g^{-1}, as the current density is increased to 0.5, 1, 2, 3, and 5 C, respectively, which is much higher than the performance of the C-S composite, as shown in Figure 4.9 (a, b) display the discharge/charge voltage profiles of C-S and C-S-TiO_2 electrodes at various rates, in which two plateaus at around 2.0 and 2.3 V are observed in the discharge process, which are typical characteristics of sulfur-carbon cathodes. Compared with previous report [13,18,37], rate capabilities (in table 4.1) for TiO_2 coated samples are higher. On the one hand, 3D porous hierarchical structure could support rapid electronic/ionic transport and improve electrochemical kinetics. On the other hand, a possible reason is that the TiO_2 works as an effective coating that helps to maintain the integrity of the electrode during charge and discharge processes. Together with the 3D hierarchically ordered porous carbon, it provides a real barrier to effectively trap polysulfides and minimize the dissolution of the polysulfides, thus reducing the loss of active mass in the cathode, and enhancing the electrochemical performance.

Table 4.1 Rate performance of Lithium-sulfur cathodes with different nanostructures

different nanostructures	0.1C	0.2C	0.5C	1C	2C	3C	5C
TiO_2 coated 3D hierarchically porous architecture [this study]	—	1142	889	770	714	677	650
porous hollow carbon-sulfur composites [13]	—	1150	970	750	600	450	820
sulfur in double-shelled hollow carbon spheres [18]	1080	820	550	350	—	—	—
graphene-based sandwich-type architecture [37]	—	1146	856	743	502	—	—

4.4 Conclusions

In summary, we have fabricated a 3D hierarchically ordered porous carbon-sulfur composite cathode, TiO_2 layer has been further introduced on the surface of C-S composite to help trap the dissolved polysulfides and enhance the strength of the entire electrode, which leads to notably improved performance for the lithium-sulfur battery, especially over long cycling and at high rates. Furthermore, the 3D hierarchically ordered porous carbon slice can be mass produced in a simple way at low cost and carbon sulfur composite thin slice could work as a binder-free cathode

without any current collectors for lithium-sulfur batteries, which makes our S-based electrode highly promising for practical application in lithium-sulfur batteries.

4.5 References

[1] H. D. Pang, Z. X. Yang, J. Lv, W. H. Yan, T. L. Guo, Energy, 69 (2014) 392-398.

[2] Z. X. Yang, Q. Meng, Z. P. Guo, X. B. Yu, T. L. Guo, Energy, 55 (2013) 925-932.

[3] P. G. Bruce, S. A. Freunberger, L. J. Hardwick, J. M. Tarascon, Nature Materials, 11 (2012) 19-29.

[4] X. W. Zhang, X. Kong, G. J. Li, J. Li, Energy, 64 (2014) 1092-1101.

[5] K. H. Seng, L. Li, D. P. Chen, Z. X. Chen, X. L. Wang, H. K. Liu, Z. P. Guo, Energy, 58 (2013) 707-713.

[6] S. E. Cheon, S. S. Choi, J. S. Han, Y. S. Choi, B. H. Jung, H. S. Lim, Journal of the Electrochemcial Society, 151 (2004) A2067-A2073.

[7] R. Xiong, F. C. Sun, H. W. He, T. D. Nguyen, Energy, 63 (2013) 295-308.

[8] J. Shim, K. A. Striebel, E. J. Cairns, Journal of the Electrochemcial Society, 149 (2002) A1321-A1325.

[9] P. Novak, K. Muller, KSV. Santhanam, O. Haas, Chemical Reviews, 97 (1997) 207-281.

[10] L. X. Yuan, H. P. Yuan, X. P. Qiu, L. Q. Chen, W. T. Zhu, Journal of Power Sources, 189 (2009) 1141-1146.

[11] Y. V. Mikhaylik, J. R. Akridge, Journal of the Electrochemcial Society, 151 (2004) A1969-A1976.

[12] G. He, X. L. Ji, L. Nazar, Energy & Environmental Science, 4 (2011) 2878-2883.

[13] N. Jayaprakash, J. Shen, S. S. Moganty, A. Corona, L. A. Archer, Angewandte Chemie International Edition, 50 (2011) 5904-5908.

[14] W. Ahn, K. B. Kim, K. N. Jung, K. H. Shin, C. S. Jin, Journal of Power Sources, 202 (2012) 394-399.

[15] B. L. Ellis, K. T. Lee, L. F. Nazar, Chemistry of Materials, 22 (2010) 691-714.

[16] B. Zhang, X. Qin, G. R. Li, X. P. Gao, Energy & Environmental Science 3 (2010) 1531-1537.

[17] J. Schuster, G. He, B. Mandlmeier, T. Yim, K. T. Lee, T. Bein, L. F. Nazar, Angewandte Chemie International Edition, 51 (2012) 3591-3595.

[18] C. F. Zhang, H. B. Wu, C. Yuan, Z. P. Guo, X. W. Lou, Angewandte Chemie International Edition, 51 (2012) 9592-9595.

[19] S. Dorfler, M. Hagen, H. Althues, J. Tubke, S. Kaskel, M. J. Hoffmann, Chemical Communications, 48 (2012) 4097-4099.

[20] J. C. Guo, Y. H. Xu, C. S. Wang, Nano Letters, 11 (2011) 4288-4294.

[21] N. W. Li, M. B. Zheng, H. L. Lu, Z. B. Hu, C. F. Shen, X. F. Chang, G. B. Ji, J. M. Cao, Y. Shi, Chemical Communications, 48 (2012) 4106-4108.

[22] J. Z. Wang, L. Lu, M. Choucair, J. A. Stride, X. Xu, H. K. Liu, Journal of Power Sources, 196 (2011) 7030-7034.

[23] L. Zhang, L. W. Ji, P. A. Glans, Y. G. Zhang, J. F. Zhu, J. H. Guo, Physical Chemistry Chemical Physics, 14 (2012) 13670-13675.

[24] L. W. Ji, M. Rao, H. M. Zheng, L. Zhang, Y. C. Li, W. H. Duan, Journal of the American Chemical Society, 133 (2011) 18522-18525.

[25] L. F. Xiao, Y. L. Cao, J. Xiao, B. Schwenzer, M. H. Engelhard, L. V. Saraf, Advanced Materials, 24 (2012) 1176-1181.

[26] F. Wu, J. Z. Chen, R. J. Chen, S. X. Wu, L. Li, S. Chen, T. Zhao, The Journal of Physical Chemistry C, 115 (2011) 6057-6063.

[27] Y. Yang, G. H. Yu, J. J. Cha, H. Wu, M. Vosgueritchian, Y. Yao, ACS Nano, 5 (2011) 9187-9193.

[28]F. Wu, J. Z. Chen, L. Li, T. Zhao, R. J. Chen, The Journal of Physical Chemistry C, 115 (2011) 24411-24417.

[29] Z. W. Seh, W. Y. Li, J. J. Cha, G. Y. Zheng, Y. Yang, M. T. Mcdowell, P. C. Hsu, Y. Cui, Nature Communications, 4 (2013) 1331.

[30] H. Kim, J. T. Lee, D. C. Lee, A. Magasinski, W. Cho, G. Yushin. Advanced Energy Materials, 3 (2013) 1308–1315.

[31] K. T. Lee, R. Black, T. Yim, X. L. Ji, L. F. Nazar, Advanced Energy Materials, 2 (2012) 1490-1496.

[32] C. F. Xue, B. Tu, D. Y. Zhao, Advanced Functional Materials, 18 (2008) 3914-3921.

[33] C. Lai, X. Gao, B. Zhang, T. Yan, Z. Zhou, The Journal of Physical Chemistry C, 113 (2009) 4712-4716.

[34] S. Stankovich, D. A. Dikin, R. D. Piner, K. A. Kohlhaas, A. Kleinhammes, Y. Jia, Y. Wu, S. T. Nguyen, R. S. Ruoff, Carbon 45 (2007) 1558-1565.

[35] B. Ding, C. Z. Yuan, L. F. Shen, G. Y. Xu, P. Nie, Q. X. Lai, X. G. Zhang, Journal of Materials Chemistry A, 1 (2013) 1096-1101.

[36] J. Y. Li, B. Ding, G. Y. Xu, L. R. Hou, X. G. Zhang, C. Z. Yuan, Nanoscale, 5 (2013) 5743-5746.

[37] R. J. Chen, T. Zhao, J. Lu, L. Li, J. Z. Chen, G. Q. Tan, Y. S. Ye, K. Amine, Nano Letters, 13 (2013) 4642-4649.

5 A FACILE SYNTHESIS APPROACH TO MICRO-MACROPOROUS CARBON FROM COTTON AND ITS APPICATION IN THE LITHIUM-SULFUR BATTERY

5.1 Introduction

The lithium-sulfur battery is expected to meet the demands of power sources for electric vehicles due to its abundant raw materials, nontoxicity, and high theoretical storage capacity (1675 mAh g^{-1}) [1-4]. Practical application of the Li-S battery, however, is greatly hampered by two major challenges. One is the low electrical conductivity of sulfur and the intermediate polysulfide products [5-7]. The other one is the high solubility of the intermediate lithium polysulfides in organic electrolytes, which can shuttle between the anode and cathode, resulting in the precipitation of solid Li_2S_2 and Li_2S on the cathode [8-10]. These issues lead to the low utilization of sulfur, low Coulombic efficiency, and severe degradation of cycle life [4, 11].

In attempts to overcome the problems mentioned above, various strategies have been developed, such as the optimization of the organic electrolyte [3, 12-16] and the preparation of conductive polymer/sulfur composites [17-20] and carbon/sulfur composites. It should be noted that employing porous carbon to constrain the sulfur or lithium polysulfide within a framework, such as microporous carbon [21-27], mesoporous carbon [28-32], hollow carbon spheres [33,34], porous carbon fibers [35], carbon nanotiles [36], or carbon nanotubes [37,38] can effectively minimize the shuttling of polysulfides and increase the utilization and cycling stability of sulfur cathodes. Carbon substrates with different pore types can offer different advantages.

The macroporous carbon can store more sulfur in its large pores, however, the macropores only weakly confine polysulfides, and the macroporous carbon exhibits inferior electrochemical properties. Compared with their macroporous counterpart, both microporous carbon and mesoporous carbon exhibit much improved sulfur utilization and sulfur retention, leading to good electrochemical performance. The disadvantage is that the sulfur content in the composite is low. In addition, majority of carbon materials used in confining sulfur so far are difficult to be applied in practical applications due to their complicated preparation processing and high cost.

Cotton is well known as one of the most important and common commodities in the world. Selecting cotton as the precursor to prepare porous carbon can not only reduce its preparation costs but can also achieve mass production. Herein, we report a novel and facile approach to synthesize cotton-based porous carbon, and use it as an improved confinement matrix to encapsulate active sulfur for high performance lithium-sulfur batteries.

Figure 5.1 A schematic illustration for the preparation of porous carbon-sulfur composites.

5.2 Experimental

5.2.1 Preparation of porous carbon-sulfur composite

The schematic illustration for the preparation of porous carbon-sulfur composites from cotton is presented in the Figure 5.1. Firstly, 12 g cotton was impregnated with solvent mixtures of urea/KOH/H_2O (U-K) (10:10:80 w/w) and KOH/H_2O (K) (20:80) for 6 h, respectively. Then, each sample was dried at 80 ^oC for 24 h. The as-prepared precursor was then heated at 700 ^oC for 2 h at the heating rate of 5 ^oC min^{-1} under N_2 atmosphere to obtain porous carbon (PC), with the samples denoted as PC-U-K and PC-K, respectively. Actually, we designed a series of experiments to investigate the cotton treatment under different conditions and found that the

adjustment of mass ratio of KOH to urea could control the nanostructure of porous carbon (Figure 5.2).

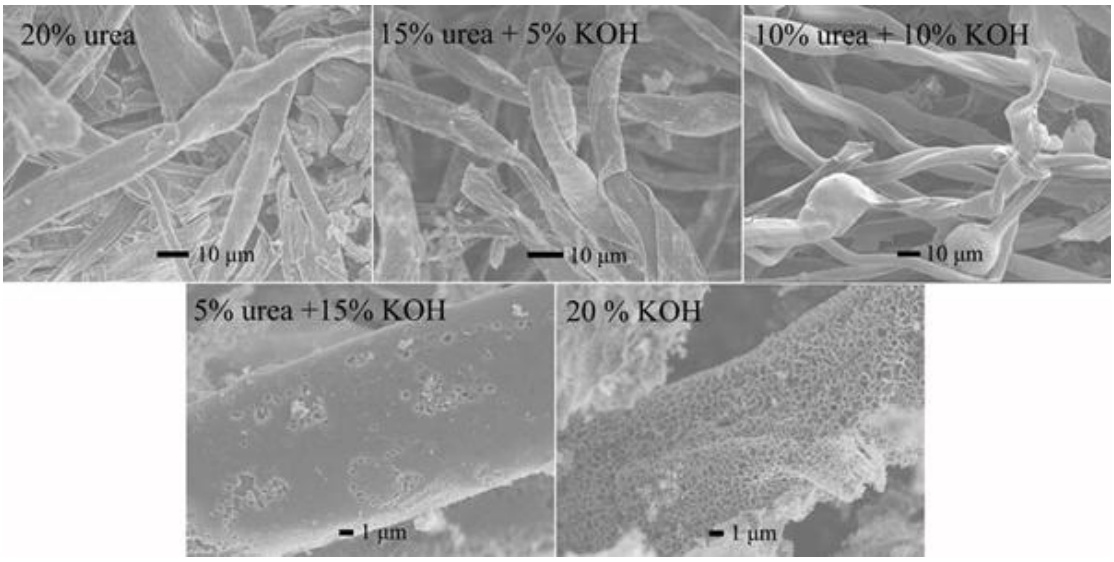

Figure 5.2 SEM images of porous carbon derived from cotton under different treatment conditions.

We found that the as-prepared samples with urea only or only a low concentration of KOH had lower surface area. Lower surface area and pore volume are not suitable for high S loading. Therefore, we chose two samples with different structures to discuss (one treated with 10% urea and 10% KOH, mainly showing micropores; the other one treated with 20% KOH, which is rich in micropores and macropores). The as-prepared porous carbon and sulfur were mixed together in a weight ratio of 2:8 and heated to 160 ^{o}C in a sealed stainless steel autoclave for 24 h to facilitate sulfur diffusion into the carbon host. Then, the composite was heated at 200 ^{o}C and kept for 10 minutes under flowing argon gas (50 $cm^3 s^{-1}$) to vaporize the sulfur deposited on the outside surface of the composite (with the samples at this stage denoted as PC-K-S and PC-U-K-S, respectively).

5.2.2 Characterization

The crystal phases and morphologies of the obtained materials were analysed by powder X-ray diffraction (XRD) using an X-ray diffractometer (MMA GBC, Australia), by Raman spectroscopy on an instrument (JOBIN YVON HR800) equipped with a 632.8 nm diode laser, by JEOL JSM-7500FA field-emission scanning electron microscopy (FESEM), and by JEOL 2011 transmission electron microscopy (TEM). The content of sulfur in composites was measured by Thermogravimetric analysis/differential scanning calorimetry (TGA/DSC) type instrument (METTLER TOLEDO, Switzerland) at a heating rate of 10 ^{o}C min^{-1} from room temperature to 500 ^{o}C under argon atmosphere. The porous structure of the samples was confirmed by N_2 adsorption–desorption isotherm at 77 K.

5.2.3 Electrochemical measurements

The PC-K-S and PC-U-K-S composites (80% by weight) were mixed with super-P (10%) and PVDF (10%) in NMP to form the slurry, respectively. After that, the electrodes were prepared by coating the slurry onto aluminium foil and then dried at 50 ^{o}C for 24 h. Coin-type (CR2032) cells were assembled in an argon-filled glove box. The electrolyte used was 1 M lithium bis(trifluoromethanesulfonyl)imide in a solvent mixture of 1,3-dioxolane (DOL): dimethoxyethane (DME) (1:1, v/v), containing $LiNO_3$ (1 wt%). The coin cells were galvanostatically charged-discharged from 1.8 to 2.6 V using a cell test instrument (CT2001A, LAND, China).

5.3 Results and discussion

SEM images of the raw cotton and the porous carbon samples made from various conditions are shown in Figure 5.3.

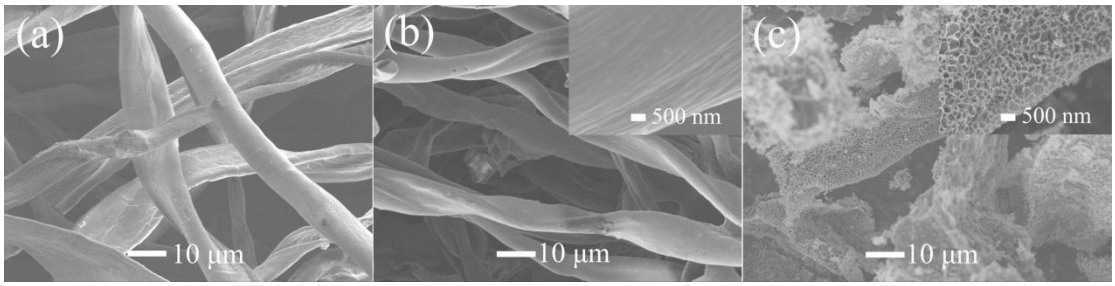

Figure 5.3 SEM images of (a) raw cotton, (b) PC-U-K, (c) PC-K.

The fibrous structure of the cotton was still maintained in the PC-U-K, while the fibrous structure was destroyed in the PC-K sample, which shows a three-dimensional porous structure. There are decomposition and drastic reaction between the carbon and KOH when the cotton is impregnated in KOH solution followed with carbonization process. These reactions results in the formation of macropores with pore size from 100 to 300 nm. In this case, KOH first reacts with carbon according to the reaction (1)

$6KOH+2C=2K+3H_2+2K_2CO_3$ (when annealing temperature is above 400 ^oC) (1)

After the reaction (1), the decomposition of K_2CO_3 and reactions of $K/K_2CO_3/CO_2$ with carbon could generate a large amount of nanoscale pores [39]. When the cotton was impregnated with KOH and urea simultaneously, the extent of the reaction between KOH and carbon was weakened, therefore, no obvious macropores were generated and the entire structure of cotton could be maintained. Indeed, the role of urea is to generate micropores as well, by decomposing to NH_3 during the

carbonization process. The yield of PC-U-K and PC-K are 15% and 9% based on the initial cotton weight, respectively.

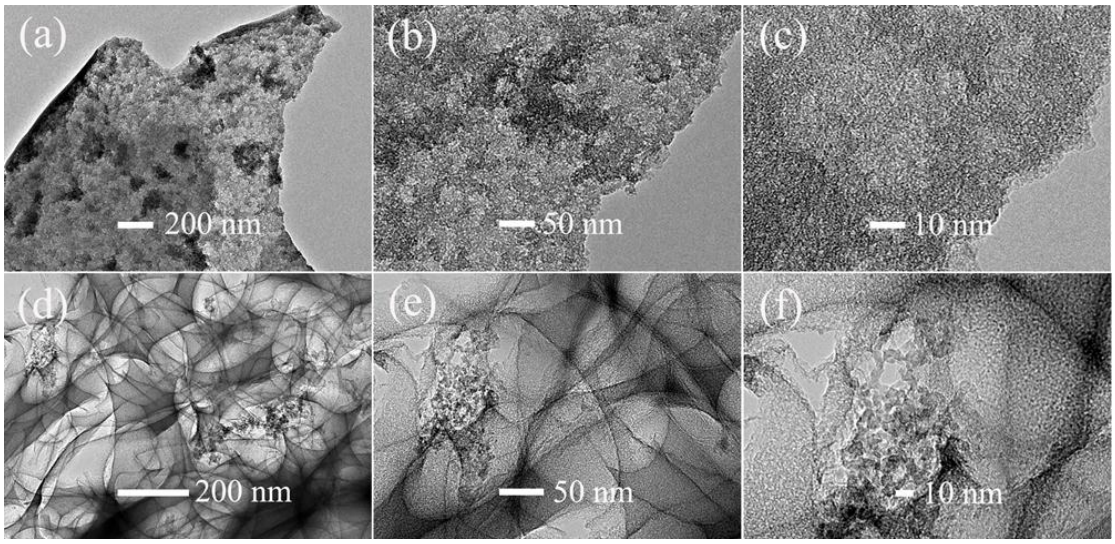

Figure 5.4 TEM images of (a-c) PC-U-K and (d-f) PC-K.

In order to investigate the microstructure of the samples in detail, TEM and HRTEM were conducted at various magnifications. Figure 5.4 shows TEM images of PC-U-K and PC-K. Compared to the PC-U-K, PC-K sample shows hierarchically porous structure and macropores with different sizes are well distributed in the PC-K sample which connected with each other form into a three-dimensional conductive network. However, it is not very clear to observe micropores from TEM images, therefore, nitrogen adsorption isotherms were employed to further investigate the microporous structure. It can be imagined that the hierarchically porous structure with micro-macropores framework is highly desirable for high-performance electrode materials. The micro-macropores can not only facilitate loading of sulfur into the pores, but also provide a large reaction surface area, which helps electrolyte

immersion and fast ion transport in the electrode/electrolyte interface, thus enhancing the electrochemical performance of electrodes.

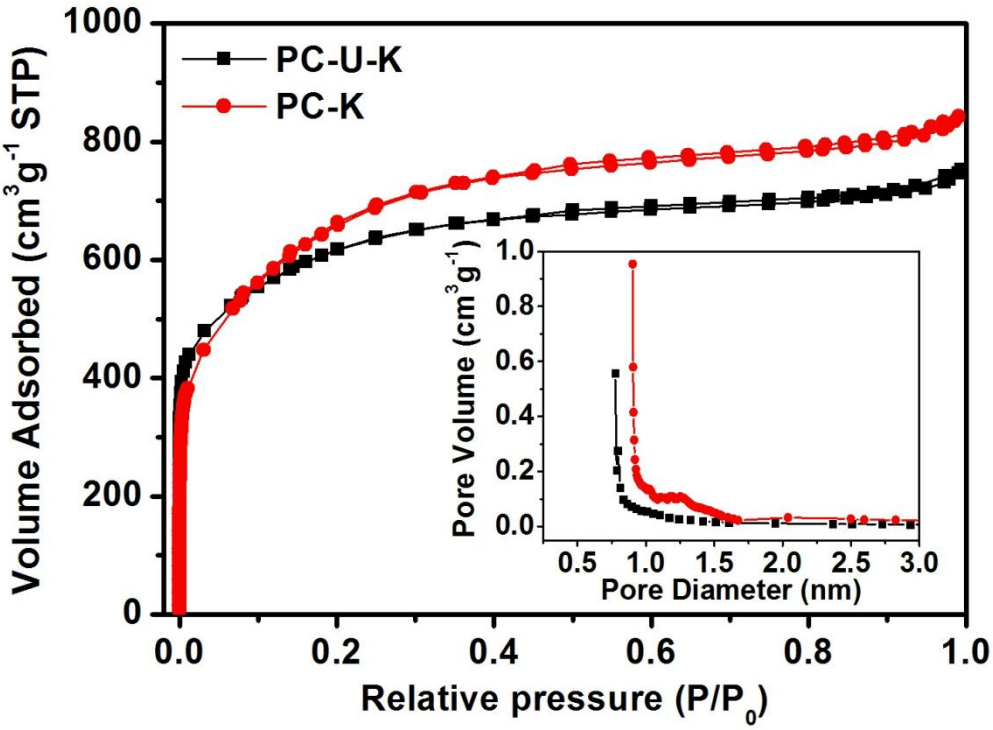

Figure 5.5 N_2 sorption isotherms of the PC-U-K and PC-K. Inset shows the pore-size distributions for the materials.

Figure 5.5 shows the nitrogen adsorption isotherms of the PC-U-K and PC-K. Both the PC-U-K and the PC-K present type-I isotherms, indicating the microporous feature of the samples. Moreover, the pore-size distributions of the carbon materials is shown in the Figure 5.5 inset. The PC-U-K shows a dominant peak centered at 1.0 nm, while a peak centered at 1.6 nm can be observed for the PC-K. The BET surface area and total pore volume for PC-U-K and PC-K are 989 and 882 m^2 g^{-1}, and 0.58 and 0.52 cm^3 g^{-1}, respectively. The difference in the specific surface area and pore volume may be introduced by the macropores in the PC-K which generated by KOH

treatment. These additional macropores of the PC-K sample compared to that of the PC-U-K sample will play a significant role in facilitating sulfur loading into micropores, fast transport of ion and electrolyte, consequently improving the electrochemical performance of sulfur/carbon cathode.

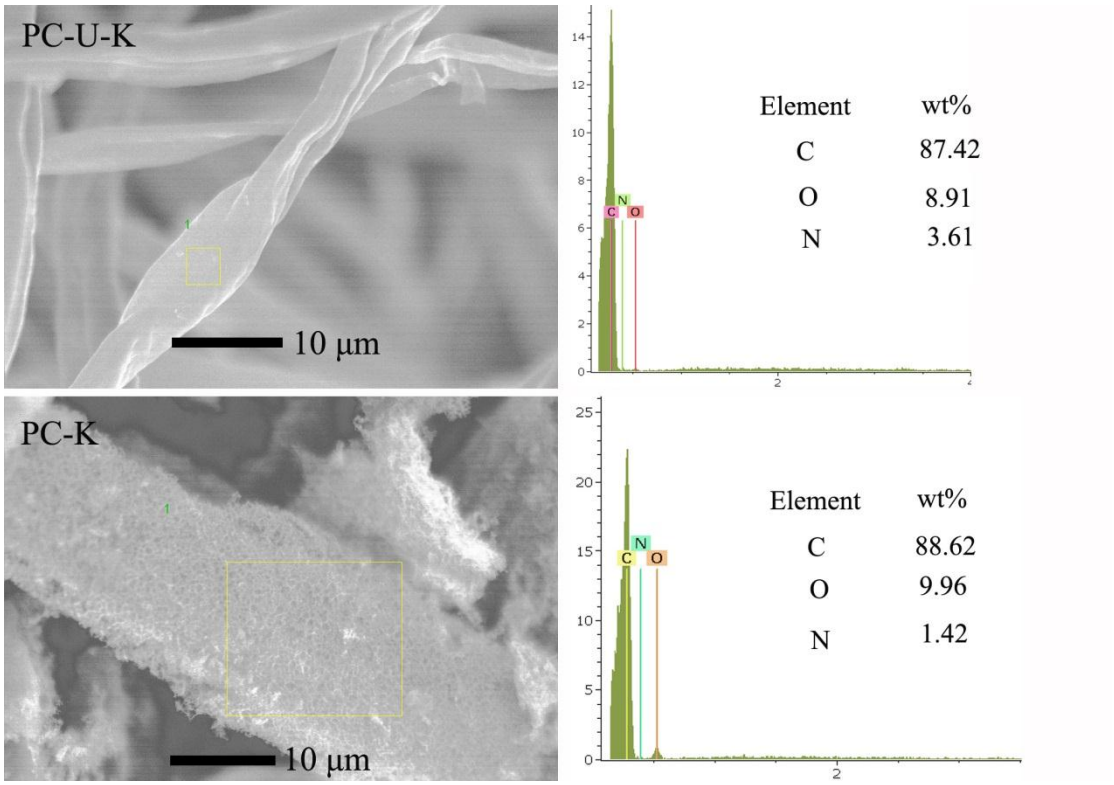

Figure 5.6 SEM images and corresponding Energy deispersive spectroscopy analysis of the PC-U-K and PC-K samples.

It is a fact that adding urea could lead to the N-doped carbon. However, cotton contains elemental nitrogen itself (Figure 5.6). EDX analysis shows that the content of N in PC-U-K and PC-K is very low, 3.61% and 1.42%, respectively. Therefore, the effect of N-doping on the electrochemical performance is not obvious. In addition, we work focused on effect of different nanostructure on the electrochemical properties. Therefore, we do not discuss the issue of N-dopping introduced by urea in detail.

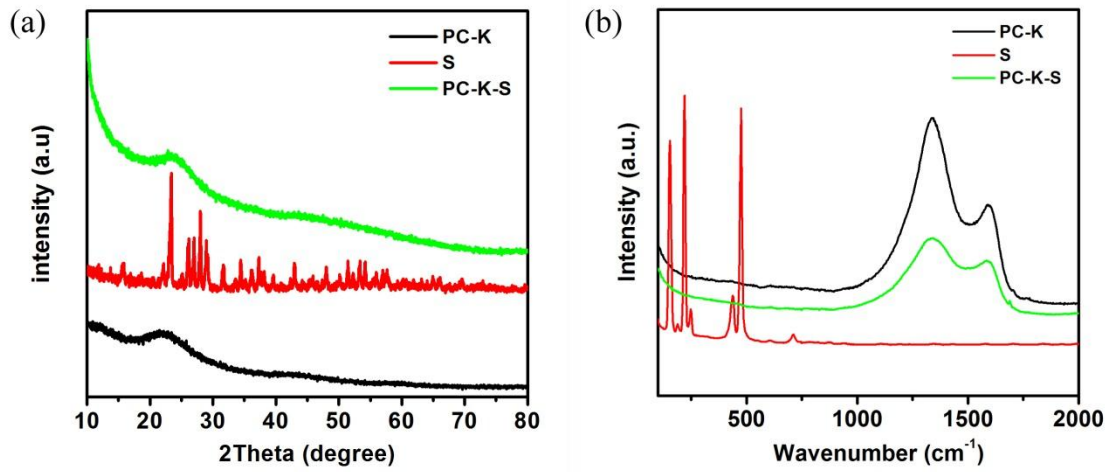

Figure 5.7 XRD patterns and Raman spectra of the PC-K, S, and PC-K-S composite.

The XRD patterns for the PC-K, S, and PC-K-S are shown in Figure 5.7 (a). The peak at 24.4^{o}C can be assigned to the (002) crystallographic planes of graphite in the PC-K sample. The low intensity and the high peak broadening are typical feature of amorphous carbon. In contrast, the pure elemental sulfur has well-defined diffraction peaks, corresponding to an orthorhombic structure. Although there is a substantial amount of sulfur in the PC-K-S composite, the peaks of elemental sulfur were not observed, suggesting good dispersion of the S within the porous carbon host [22, 40]. Raman spectra of PC-K, S, and PC-K-S composite were also carried out to further observe their structure in Figure 5.7 (b). Element sulfur displays typical Raman peaks corresponding to the S-S bond [41], however, any sulfur peaks cannot be observed in the PC-K-S, which is also indicates that sulfur is successfully embedded into the pores of the PC-K. The sulfur content in the PC-U-K-S and PC-K-S composites was determined by TGA conducted under argon atmosphere. The amount of sulfur in the PC-U-K-S and PC-K-S composites is 50 wt% and 68 wt%, respectively.

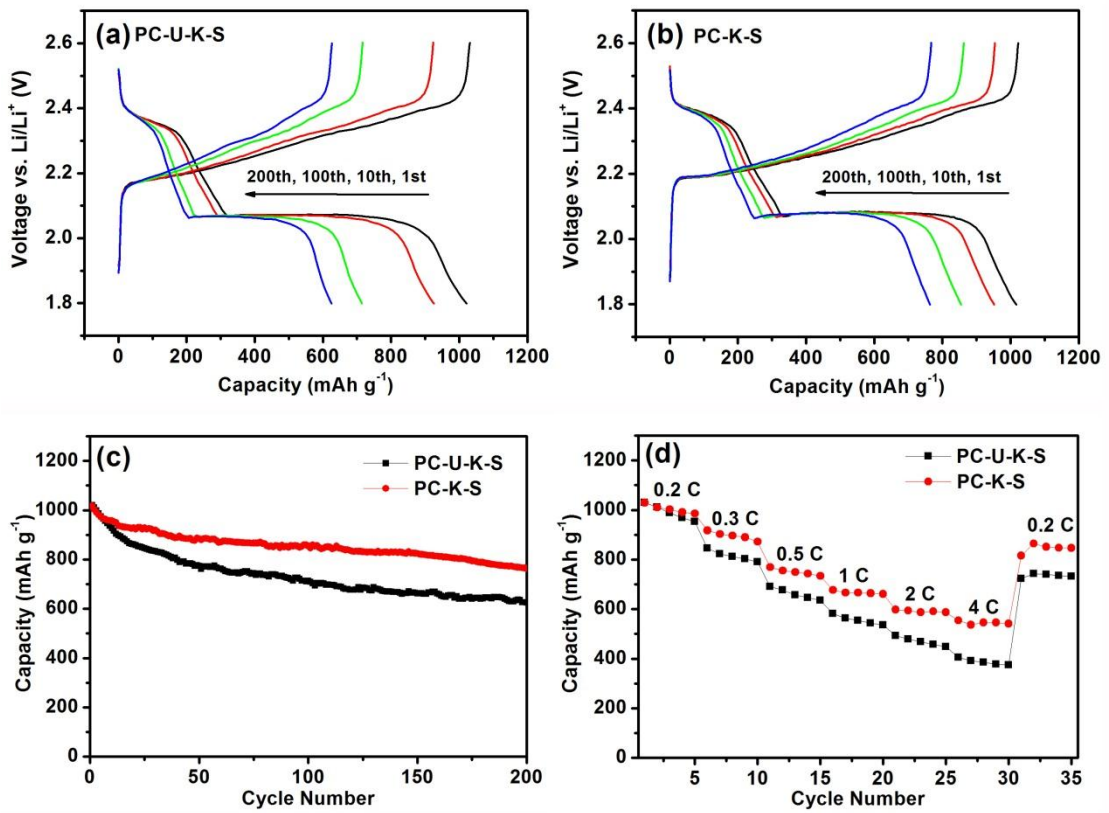

Figure 5.8 Discharge/charge voltage profiles of (a) PC-U-K-S and (b) PC-K-S electrodes at various cycles; (c) cycling performances of PC-U-K-S and PC-K-S electrodes at current density of 0.2 C; (d) rate capabilities of PC-U-K-S and PC-K-S electrodes.

Figure 5.8 (a, b) displays the discharge/charge voltage profiles of the PC-U-K-S and PC-K-S electrodes at various different cycles. Typical plateaus are observed, which are the characteristics of sulfur-based electrodes. The discharge plateau of the PC-U-K-S composite electrode obviously shrinks as the increase of cycle number, however, the PC-K-S electrode has a good overlap of discharge plateaus during the cycling tests, suggesting the excellent stability and reversibility of the PC-K-S electrode. After the 100th cycle, the retained discharge capacity for the PC-U-K-S composite electrode is 710 mAh g^{-1}, indicating a poor cycling performance. In

contrast, the capacity of the PC-K-S composite electrode capacity only drops to 850 mAh g^{-1} after the 100th cycle, with the retention rate of 83%. The cycling performances of the PC-U-K-S and PC-K-S are shown in Figure 5.8 (c). The initial discharge capacities for the PC-U-K-S and PC-K-S cathodes are 1020 and 1017 mAh g^{-1} at the rate of 0.2 C, respectively. After 200 cycles, the PC-K-S electrode retains a reversible capacity of 760 mAh g^{-1}, while only 620 mAh g^{-1} is left for the PC-U-K-S. Moreover, the Columbic efficiency of PC-K-S cell approaches 99% after several cycles, while the Columbic efficiency of PC-U-K-S cells only reaches 93% (Figure 5.9).

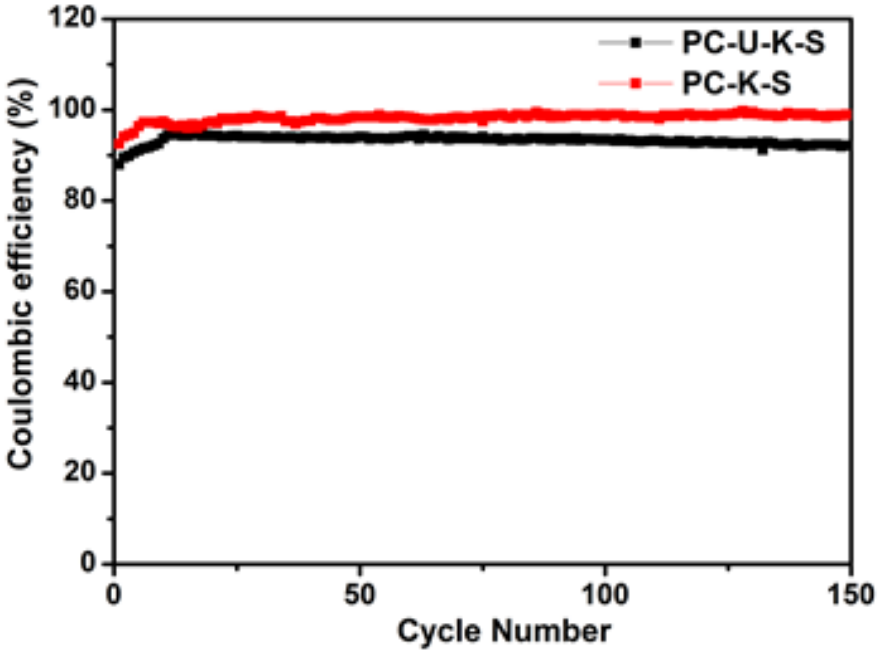

Figure 5.9 The efficiency of PC-U-K-S and PC-K-S cells as function of cycle number.

As is well-known, sulfur loading is an important factor that is correlated with the performance. Generally, the lower the sulfur loading, the better the performance of

the electrode, however, this is detrimental for practical applications, as high carbon content reduces the energy density per gram of cathode. The battery in our study possessed higher sulfur content than in most previous reports (Table 5.1), which could be one of the reasons for its a slightly lower capacity compared with those references in which the capacity is calculated based on sulfur only, such as microporous carbon (40% S) with capacity of 1142 mAh g^{-1} [24], and micro-mesoporous carbon sphere (40% S) with capacity of 900 mAh g^{-1} [42]. However, if calculation is based on the total mass of composite for carbon-sulfur electrodes, the capacity of our PC-K-S electrodes would be better than the reported data shown in Table 5.1.

Table 5.1 Selected properties of lithium-sulfur cathodes with different types of microporous carbon substrates

Microporous carbon type	S content (%)	Current rate	Initial capacity (mAh g^{-1})	Cycle number	Final capacity based on the weight of sulfur (mAh g^{-1})	Final capacity based on the weight of composite (mAh g^{-1})
Micro-macroporous carbon [this study]	68	0.2 C	1017	50 100 200	880 850 760	598 578 516
MOF-derived microporous carbon [21]	43	0.06 C	1450	100	490	210
Hierarchically porous honeycomb carbon [22]	66.3	2 C	923	100	564	373
Microporous carbon [24]	40	0.1 C	1674	200	1142	456
Hierarchically porous carbon [25]	54	0.1 C	1177	50	762	411
Hierarchically porous carbon monoliths [26]	75	0.1 C	1305	25	469	351
Biomass derived activated carbon [27]	60.1	0.2C	1258	100	750	450
Micro-mesoporous carbon spheres [42]	40	0.1 C	1550	100	900	360

The rate capability of the PC-U-K-S and PC-K-S electrodes is shown in Figure 5.8(d). The discharge capacity is decreased with the increase of rate from 0.2 C to 4 C. A satisfactory capacity of 550 mAh g^{-1} is obtained for the PC-K-S composite electrode, even at 4 C. The rate performance of the PC-K-S electrode is much better than that of the PC-U-K-S electrode, which may be attributed to the facile electronic/ionic transport and enhanced reaction kinetics in the PC-K-S composite.

It is reported that the greater the percentage of micropores in the total pore volume, the better the electrochemical performance that can be obtained [42]. In our study, interestingly, the performance of the PC-K-S composite electrode with micro-macroporous structure is much better than that of the PC-U-K-S composite electrode containing only micropores. This contradictory result could be attributed to the unique micro-macroporous interconnected framework of the PC-K carbon matrix. For the PC-U-K with micropores only, a significantly amount of sulfur is located on the surface of the PC-U-K-S composite instead of within the pores. It is hard for the micropores to be fully filled with sulfur just by capillary force. The PC-K has a three-dimensional hierarchically porous interconnected structure, however, and the macropores can supply channels for easy sulfur loading into the micropores. This can be concluded from the nitrogen adsorption isotherms of the PC-U-K-S and PC-K-S composites (Figure 5.10).

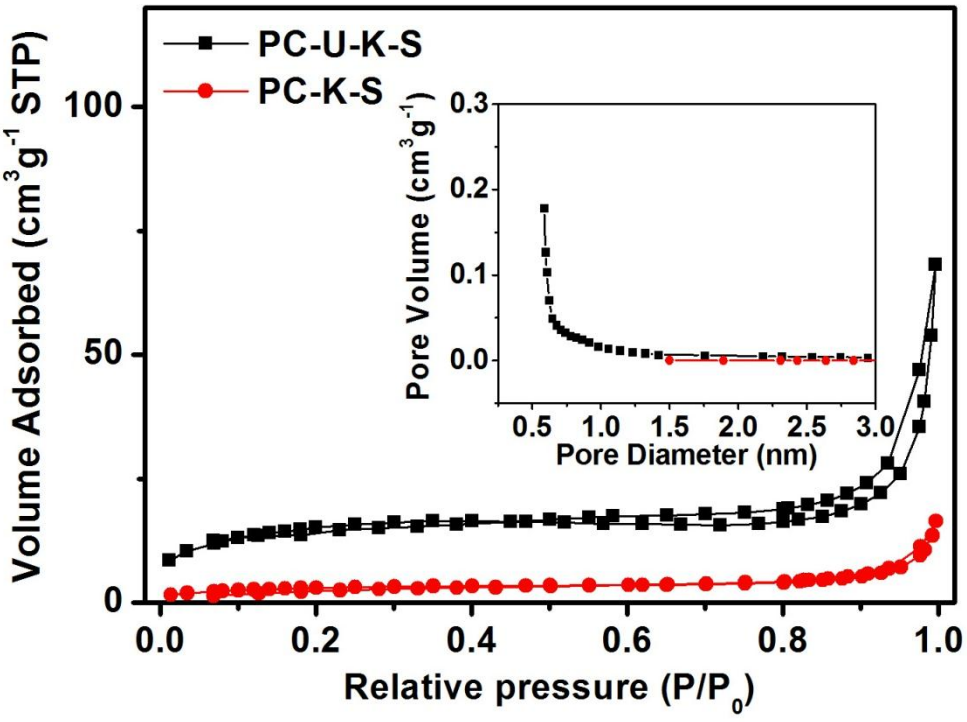

Figure 5.10 N_2 sorption isotherms of the PC-U-K-S and PC-K-S composites. Inset shows the pore-size distributions for the composites.

The BET surface area for the PC-U-K-S only decreased to 240 m^2 g^{-1}, and there is a broad peak centered at 1.0 nm, indicating that the micropores were not completely filled with sulfur, so that excess sulfur remained on the surface of the PC-U-K-S composite. However, the specific surface area for the PC-K-S composite significantly dropped to 42 m^2 g^{-1}, and the micropores almost disappeared completely, confirming that the storage of sulfur mainly occurs in the micropores. After the introduction of sulfur, the PC-K-S still maintained the original macroporous morphology, and no obvious bulk sulfur could be observed on the surface of the composite in the Figure 5.11.

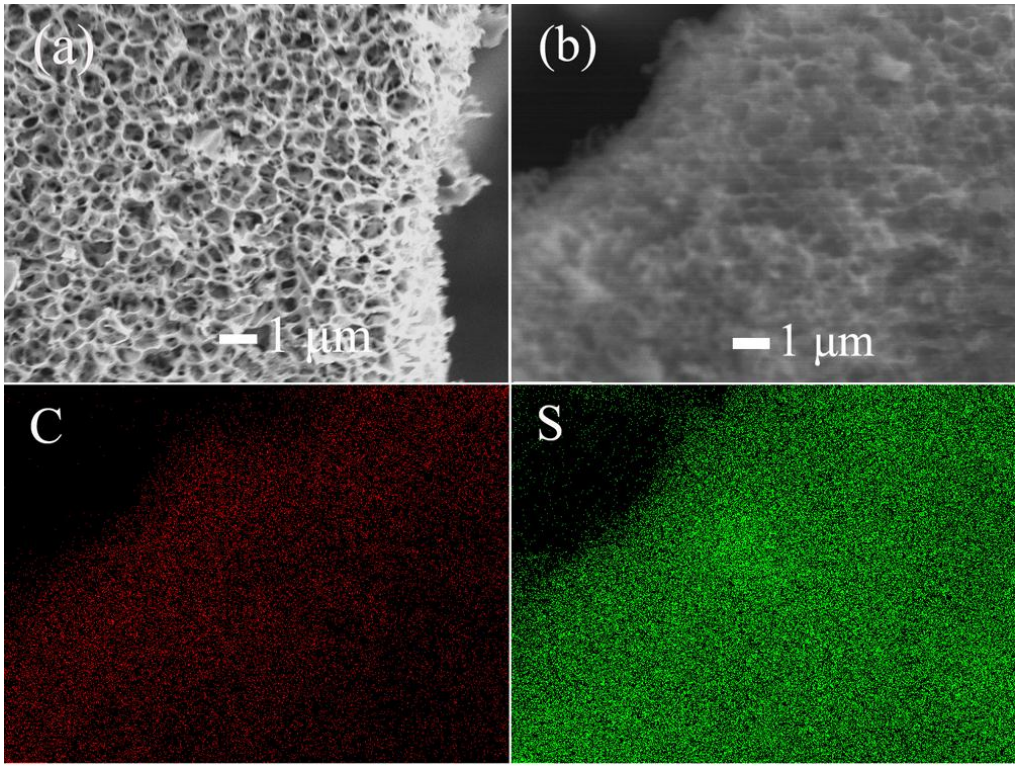

Figure 5.11 SEM images of PC-K-S composite, and corresponding elemental map images of carbon and sulfur.

Based on the observation above, we believe that the macropores play a role in supplying channels for sulfur loading into the micropores instead of encapsulating sulfur. Figure 5.11 (b) shows the element mapping of sulfur and carbon for the PC-K-S composite and confirms that the sulfur is homogeneously distributed in the framework of the hierarchically porous carbon. In addition, the macroporous structure connected with the micropores in the PC-K-S can facilitate fast transport of electrons/ions and electrolyte, which in turn enhances the electrochemical performance of the sulfur cathode.

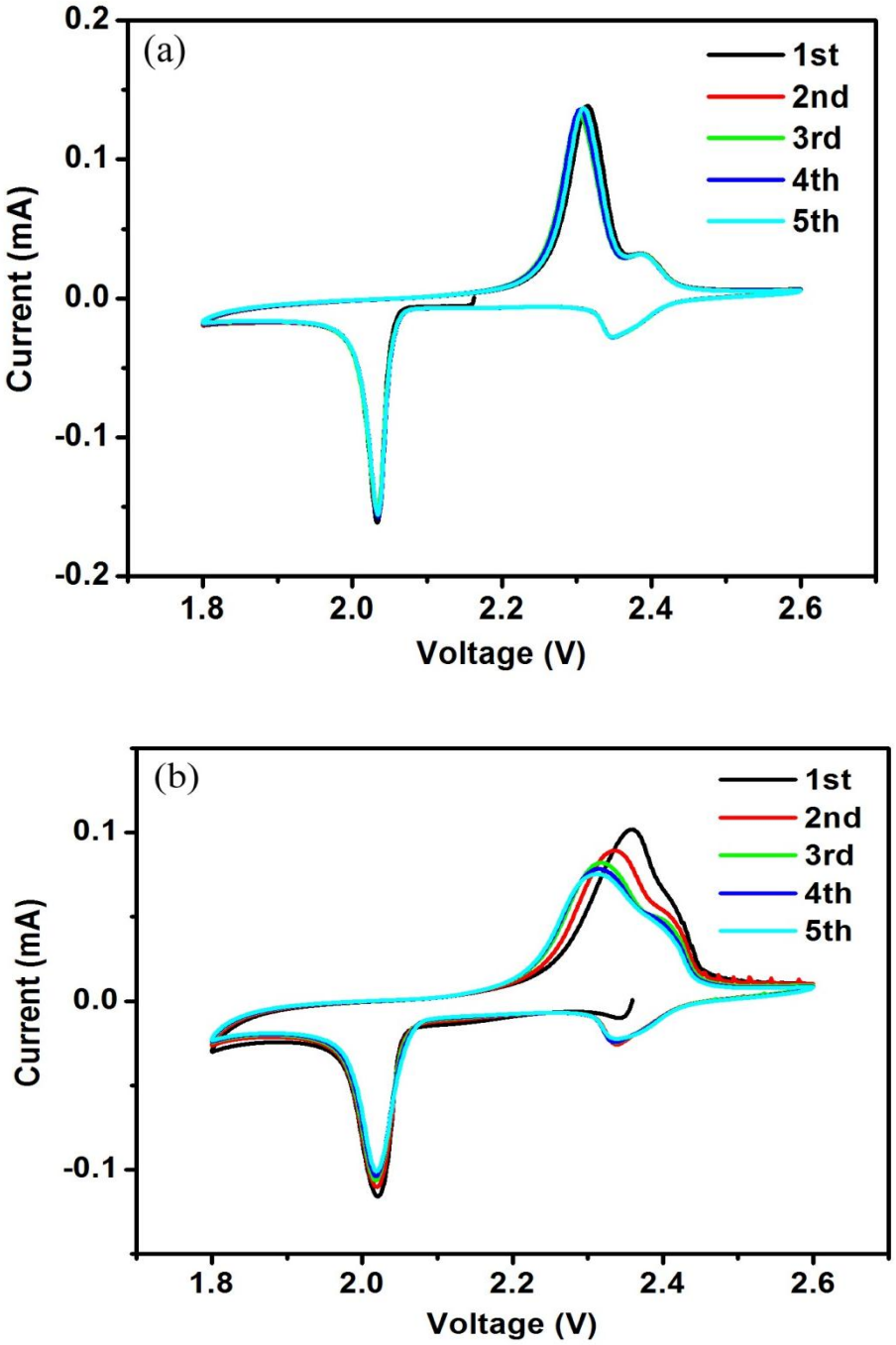

Figure 5.12 CV curves of the cell with (a) PC-K-S and (b) PC-U-K-S composites electrodes.

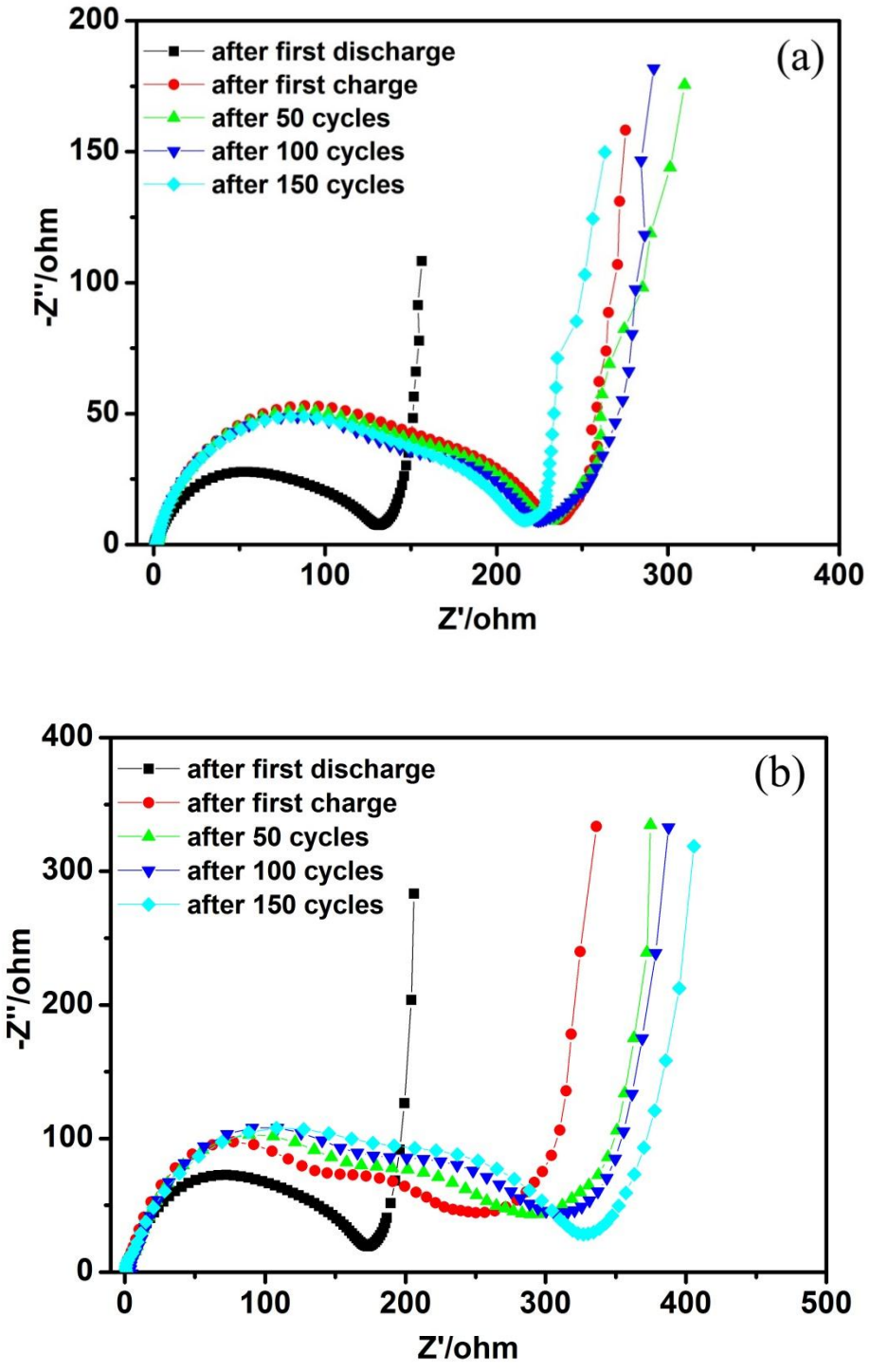

Figure 5.13 EIS spectra of the cell with (a) PC-K-S and (b) PC-U-K-S composites after cycles.

In order to further investigate the electrochemical reaction process, cyclic voltammetry (CV) and electrochemical impedance spectroscopy (EIS) analysis test

for the PC-K-S and PC-U-K-S electrodes was carried out (see Figure 5.12 and Figure 5.13). CV curves show typical reduction and oxidation peaks representing for reaction of sulfur with lithium during the charge-discharge processes. The sharp redox peaks with stable overlapping features for PC-K-S electrode confirm the high reversibility and excellent stability of electrode after first cycle [20, 43]. In addition, the impedance plots display a semicircular loop standing for the charge-transfer resistance (R_{ct}), which is mainly generated at the interface between the electrode and the electrolyte. Electrolyte resistance R_{ct} of PC-K-S cell remains unchanged even after 200 cycles, while R_{ct} of PC-U-K-S cell increases moderately with the increased cycles. This indicated that the polysulfides could be well confined in the PC-K-S electrode, and thus the dissolution of polysulfides into electrolyte and the increase of viscosity are successfully avoided. The charge-transfer resistance of PC-K-S is stabilized at around 200 Ω cm^2 (calculated after the electrode area normalization) after the first cycle, which suggests a stable electrochemical environment during the cycling process.

5.4 Conclusion

In summary, a hierarchically porous carbon material with high surface area has been prepared from cotton and used to fabricate a carbon/sulfur composite, which is then explored as cathode material for lithium/sulfur batteries. This unique micro-macroporous structure is found to be directly related to the battery performance. The macroporous structure of this carbon provides channels for sulfur to be loaded into micropores and enhances fast transport of electrons/ions and electrolyte. The

microporous structure can trap elemental S and Li polysulfides during cycling. As a result, the composite electrode exhibits an excellent capacity of 760 mAh g^{-1} after 200 cycles and a good rate capability. More importantly, the hierarchically porous carbon can be mass produced in a simple way at low cost, and the sulfur loading is higher than for most of the reported composites, which makes our S-based electrode highly promising for practical application in lithium-sulfur batteries.

5.5 References

[1] J. Shim, K. A. Striebel, E. J. Cairns, Journal of the Electrochemical Society, 149 (2002) A1321-A1325.

[2] P. G. Bruce, S. A. Freunberger, L. J. Hardwick, J. M. Tarascon, Nature Materials, 11 (2012) 19-29.

[3] M. K. Song, Y. G. Zhang, E. J. Cairns, Nano Letters, 13 (2013) 5891-5899.

[4] H. L. Wang, Y. Yang, Y. Y. Liang, J. T. Robinson, Y. G. Li, A. Jackson, Y. Cui, H. J. Dai, Nano Letters, 11 (2011) 2644-2647.

[5] L. C. Yin, J. L. Wang, F. J. Lin, J. Yang, Y. Nuli, Energy & Environmental Science, 5 (2012) 6966-6972.

[6] P. Novak, K. Muller, KSV. Santhanam, O. Haas, Chemical Reviews, 97 (1997) 207-281.

[7] Y. Yang, G. Y. Zheng, S. Misra, J. Nelson, M. F. Toney, Y. Cui, Journal of the American Chemical Society, 134 (2012) 15387-15394.

[8] N. Jayaprakash, J. Shen, S. S. Moganty, A. Corona, L. A. Archer, Angewandte Chemie International Edition, 50 (2011) 5904-5908.

[9] W. Ahn, K. B. Kim, K. N. Jung, K. H. Shin, C. S. Jin, Journal of Power Sources, 202 (2012) 394-399.

[10] Y.V. Mikhaylik, J. R. Akridge, Journal of the Electrochemical Society, 151 (2004) A1969-A1976.

[11] G. He, X. L. Ji, L. Nazar, Energy & Environmental Science, 4(2011) 2878-2883.

[12] W. Weng, V. G. Pol, K. Amine, Advanced Materials, 25 (2013) 1608-1615.

[13] X. B. Cheng, J. Q. Huang, H. J. Peng, J. Q. Nie, X. Y. Liu, Q. Zhang, F. Wei, Journal of Power Sources, 253 (2014) 263-268.

[14] S. S. Zhang, D. T. Tran, Electrochimica Acta, 114 (2013) 296-302.

[15] J. T. Lee, Y. Y. Zhao, H. Kim, W. I. Cho, G. Yushin, Journal of Power Sources, 248 (2014) 752-761.

[16] N. Azimi, W. Weng, C. Takoudis, Z. C. Zhang, Electrochemistry Communications, 37 (2013) 96-99.

[17] Y. Yang, G. H. Yu, J. J. Cha, H. Wu, M. Vosgueritchian, Y. Yao, Z. N. Bao, Y. Cui, ACS Nano, 5 (2011) 9187-9193.

[18] F. Wu, J. Z. Chen, L. Li, T. Zhao, R. J. Chen, The Journal of Physical Chemistry C, 115 (2011) 24411-24417.

[19] Y.Z. Fu, A. Manthiram, The Journal of Physical Chemistry C, 116 (2012) 8910-8915.

[20] L. F. Xiao, Y. L. Cao, J. Xiao, B. Schwenzer, M. H. Engelhard, L. V. Saraf, Z. M. Nie, G. J. Exarhos, J. A. Liu, Advanced Materials, 24 (2012) 1176-1181.

[21] H. B. Wu, S. Y. Wei, L. Zhang, R. Xu, H. H. Hng, X. W. Lou, Chemistry A European Journal, 19 (2013) 10804-10808.

[22] Y. H. Qu, Z. A. Zhang, X. H. Zhang, G. D. Ren, X. W. Wang, Y. Q. Lai, Y. X. Liu, J. Li, Electrochimica Acta, 137 (2014) 439-446.

[23] S. Y. Zheng, Y. Chen, Y. H. Xu, F. Yi, Y. J. Zhu, Y. H. Liu, J. H. Yang, C. S. Wang, ACS Nano, 7 (2013) 10995-11003.

[24] S. Xin, L. Gu, N. H. Zhao, Y. X. Yin, L. J. Zhou, Y. G. Guo, Journal of the American Chemical Society, 134 (2012) 18510-18513.

[25] G. Y. Xu, B. Ding, L. F. Shen, P. Nie, J. P. Han, X. G. Zhang, Journal of Materials Chemistry A, 1 (2013) 4490-4496.

[26] L. H. Yu, N. Brun, K. Sakaushi, J. Eckert, M. M. Titirici, Carbon, 61 (2013) 245-253.

[27] J. Zhang, J. Y. Xiang, Z. M. Dong, Y. Liu, Y. S. Wu, C. M. Xu, G. H. Du, Electrochimica Acta, 116 (2014) 146-151.

[28] M. S. Park, B. O. Jeong, T. J. Kim, S. Kim, K. Y. Kim, J. S. Yu, Y. Jung, Y. J. Kim, Carbon, 68 (2014) 265-272.

[29] M. Nagao, Y. Imade, H. Narisawa, R. Watanabe, T. Yokoi, T. Tatsumi, R. Kanno, Journal of Power Sources, 243 (2013) 60-64.

[30] T. Xu, J. X. Song, M. L. Gordin, H. Sohn, Z. X. Yu, S. R. Chen, D. H. Wang, ACS Applied Materials & Interfaces, 5 (2013) 11355-11362.

[31] C. D. Liang, N. J. Dudney, J. Y. Howe, Chemistry of Materials, 21 (2009) 4724-4730.

[32] X. Y. Tao, X. R. Chen, Y. Xia, H. Huang, Y. P. Gan, R. Wu, F. Chen, W. K. Zhang, Journal of Materials Chemistry A, 1 (2013) 3295-3301.

[33] N. Jayaprakash, J. Shen, S. S. Moganty, A. Corona, L. A. Archer, Angewandte Chemie International Edition, 50 (2011) 5904-5908.

[34] C. F. Zhang, H. B. Wu, C. Z. Yuan, Z. P. Guo, X. W. Lou, Angewandte Chemie International Edition, 51 (2012) 9592-9595.

[35] B. S. Lee, S. B. Son, K. M. Park, G. Lee, K. H. Oh, S. H. Lee, W. R. Yu, ACS Applied Materials & Interfaces, 4 (2012) 6701-6709.

[36] X. Y. Tao, J. T. Zhang, Y. Xia, H. Huang, J. Du, H. Xiao, W. K. Zhang, Y. P. Gan, Journal of Materials Chemistry A, 2 (2014) 2290-2296.

[37] S. Dorfler, M. Hagen, H. Althues, J. Tubke, S. Kaskel, M. J. Hoffmann, Chemical Communications, 48 (2012) 4097-4099.

[38] J. C. Guo, Y. H. Xu, C. S. Wang, Nano Letters, 11 (2011) 4288-4294.

[39] E. Raymundo-Pinero, P. Azais, T. Cacciaguerra, D. Cazorla-Amoros, A. Linares-Solano, F. Beguin, Carbon, 43 (2005) 786-795.

[40] C. Lai, X. Gao, B. Zhang, T. Yan, Z. Zhou, The Journal of Physical Chemistry C, 113 (2009) 4712-4716.

[41]A. T. Ward, The Journal of Physical Chemistry, 72 (1968) 4133-4139.

[42] H. Ye, Y. X. Yin, S. Xin, Y. G. Guo, Journal of Materials Chemistry A, 1 (2013) 6602-6608.

[43] G. C. Li, G. R. Li, S. H. Ye, X. P. Gao, Advanced Energy Materials, 2 (2012) 1238-1245.

6 LARGE-SCALE SYNTHESIS OF ORDERED MESOPOROUS CARBON FIBER AND ITS APPLICATION AS CATHODE MATERIAL FOR LITHIUM-SULFUR BATTERIES

6.1 Introduction

Due to its ultra-high energy density (theoretically 2567 Wh kg^{-1}) and high theoretical specific capacity (1675 mAh g^{-1}), the rechargeable lithium-sulfur (Li-S) battery has attracted enormous attention in the last several years [1-3]. Sulfur cathodes face several major challenges, however, which limit their practical applications, including the low conductivity of sulfur and lithium sulfide [4,5], as well as the large volume changes in the sulfur particles during charge and discharge processes. A more significant challenge that needs to be overcome is the high solubility of high-order polysulfide intermediates in organic electrolytes. The dissolved high-order polysulfides can diffuse from the cathode and react with the lithium anode either to generate insoluble lower-order polysulfides in the form of Li_2S or Li_2S_2, leading to the precipitation of these species on the surface during cyclic processes, or form soluble low-order polysulfides, which is then transported back to the cathode side, resulting in a shuttle reaction [6,7]. The shuttle reaction and deposition of Li_2S or Li_2S_2 on the Li anode lead to the low utilization of sulfur, low coulombic efficiency of the sulfur cathode, and fast capacity fading [8,9].

There are two basic strategies to address this problem. The major stream of Li-S research has focused on the design “inside” the cathode, confining sulfur within various kinds of porous matrixes, such as porous carbon [10-16] or graphene [17-19],

or applying surface coatings of conductive polymer [20-21] or metal oxides such as TiO_2 [22] or Al_2O_3 [23] to act as a physical barrier to prevent the soluble polysulfides from dissolving in the organic electrolyte. An alternative route has concentrated on the "outside" of the cathode, such as by modification of the electrolyte [24-26] and novel cell configurations [27-29].

Herein, we report a simple electrospinning deposition method (ESD), which can mass-produce ordered mesoporous carbon fiber (OMCF). Currently, the majority of carbon materials used for confining sulfur so far are difficult to be applied in practical applications due to their complicated preparation processing and high cost. The ESD method is considered a promising method to mass-produce one-dimensional (1D) carbon materials with the advantages of simplicity, efficiency, low cost, and high yield. We have employed 1D OMCF as an improved confinement matrix for high-level sulfur impregnation. The ordered mesoporous fibrous structure builds a framework of well-connected empty sites, which could encapsulate a large amount of sulfur. Furthermore, the OMCF framework could facilitate the transport of electrons and ions and the electrolyte diffusion, and retain the polysulfides, enhancing the reversibility of electrode, which is hardly achieved by random porous structures.

6.2 Experimental section

6.2.1 Synthesis of OMCF

The OMCF was synthesized through the electrospinning technique. In a typical synthetic process, 2 g F127 was put in 8 g of ethanol with 1.2 g 0.2 M HCl and stirred for 1 h at 40 ^{o}C to yield a transparent solution. Next, 6 g of 20 wt% resol ethanolic

solution and 1.8 g tetraethyl orthosilicate (TEOS) were added in that order. The resol precursor (Mw < 500) was synthesized on the basis of previous report [30]. After being stirred for 5 h, 3g 25% polyvinyl butyral (PVB) solution in ethanol was added to the mixture. Finally, a homogeneous solution was obtained after 4 h strong mechanical stirring. Triblock copolymer Pluronic F127 and resol are regarded as template and carbon source, respectively. The role of PVB is to improve the "spinnability" of the solution, while the TEOS acts as a skeleton in the formation process for the mesoporous structure, which can be removed in the next step. The experimental procedure and the formation of ideal mesoporous structure of OMCF are shown in Figure 6.1.

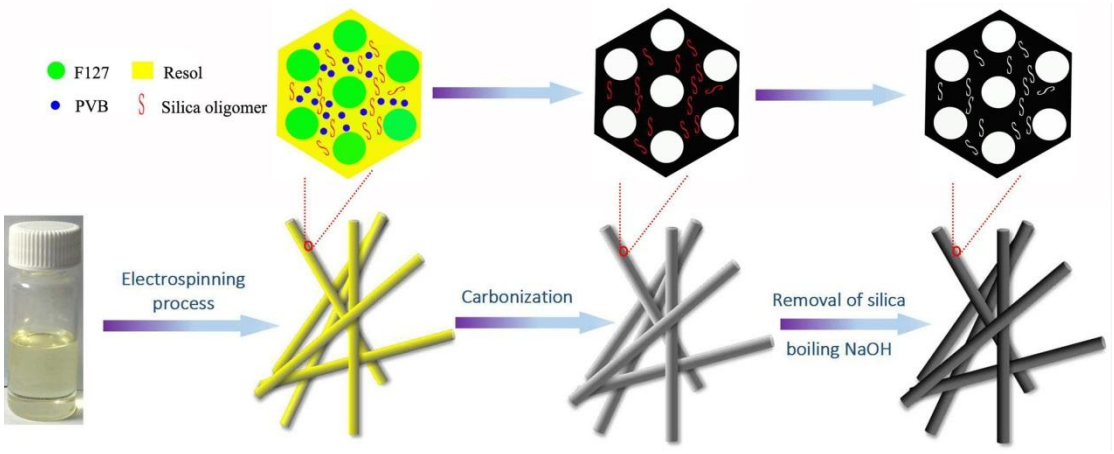

Figure 6.1 A schematic illustration of the experimental procedure and the formation of ideal mesoporous structure of OMCF.

During electrospinning process, the solution was loaded into a syringe with a metallic needle (inner diameter 0.5 mm) and a flow rate of 0.8 mL h^{-1} under the voltage of 14.5 kV. The distance from needle tip to stainless steel mesh collector was 12 cm. Then, the collected primary film was dried at room temperature for 24 h. The

as-prepared products were heat-treated at 700 ^{o}C for 2 h under flowing nitrogen gas. Afterwards, the resultant ordered mesoporous carbon–silica fiber was put into 2 mol L^{-1} boiling NaOH solution for 2 h to remove the silica to obtain OMCF. In our study, 0.2 g OMCF can be obtained per hour under our preparation condition, and the production can be easily scale-up. The control sample ordered mesoporous carbon powder (OMCP) was synthesized through the same process as the OMCF, but without electrospinning technique.

6.2.2 Fabrication of ordered mesoporous carbon fiber sulfur (OMCF-S) composite

The as-prepared OMCF and OMCP were mixed with sulfur in a weight ratio of 25:75 and heated to 160 ^{o}C in a sealed stainless steel autoclave for 24 h to facilitate sulfur diffusion into the carbon host to obtain the OMCF-S and ordered mesoporous carbon powder sulfur (OMCP-S) composite, respectively. Then, the OMCF-S and OMCP-S composite was heated at 200 ^{o}C and kept for 10 minutes under flowing argon gas (50 $cm^3 s^{-1}$) to vaporize the sulfur deposited on the outside surface of the composite.

6.2.3 Characterization

The crystal structures of the samples were carried out by powder X-ray diffraction (XRD, MMA GBC, Australia) and by Raman spectroscopy on an instrument (JOBIN YVON HR800) equipped with a 632.8 nm diode laser. Thermogravimetric analysis (TGA) was performed to measure the sulfur content with a METTLER TOLEDO TGA/DSC instrument with a heating rate of 10 ^{o}C min^{-1} from room temperature to 500 ^{o}C under a flow of argon. The specific surface areas and the pore size distribution

were analyzed by Brunauer–Emmett–Teller (BET) method and Barrett–Joyner–Halenda (BJH) model, respectively. The morphologies of the samples were analyzed by JEOL JSM-7500FA field-emission scanning electron microscopy (FESEM), and by JEOL 2011 transmission electron microscopy (TEM).

6.2.4 Electrochemical measurement

To prepare the working electrodes, the OMCF-S and OMCP-S composite was mixed with carbon black, poly(ethylene oxide) (PEO), and poly(vinylpyrrolidone) (PVP) (75:15:8:2 by weight) in deionized water to form a slurry, respectively. The slurry was then coated onto aluminium foil and dried at 50 ^{o}C for 24 h. Coin-type (CR2032) cells were assembled by inserting a carbonized filter paper between cathode and the separator in an argon-filled glove box. The electrolyte used was 1 M lithium bis(trifluoromethanesulfonyl)imide in a solvent mixture of 1,3-dioxolane (DOL): dimethoxyethane (DME) (1:1, v/v) containing $LiNO_3$ (1 wt%). The cells were galvanostatically cycled from 1.8 to 2.6 V by using LAND CT2001A instrument.

6.3 Results and discussion

Figure 6.2 presents SEM image of the resol/F127/TEOS/PVB precursor fibers before calcination. Obviously, the as-spun resol/F127/TEOS/PVB sample has good fibrous morphology with smooth surfaces and a uniform fiber diameter of less than 1 μm, indicating that the aqueous solution containing resol, PVB, and TEOS has excellent spinnability. From Figure 6.2 (b), it is found that the OMCF after heat-treatment and the removal of the silica still maintains this fibrous morphology, but exhibits a wrinkled surface morphology, mainly due to the large weight loss accompanied by

gas evolution and removal of silica. The TEM characterizations of the OMCF were performed to further investigate the ordered mesopore structure (Figure 6.2 (c) and 6.2 (d)). The OMCF shows ordered hexagonal mesostructure in large domains (mesopores with diameters of about 7 nm). The mesoporous structure is directly related to the battery performance of the sulfur cathode. Figure 6.2 (e) shows scanning TEM (STEM) and corresponding elemental mapping images of the OMCF-S composite, confirming that the sulfur is homogeneously distributed in the framework of the OMCF matrix.

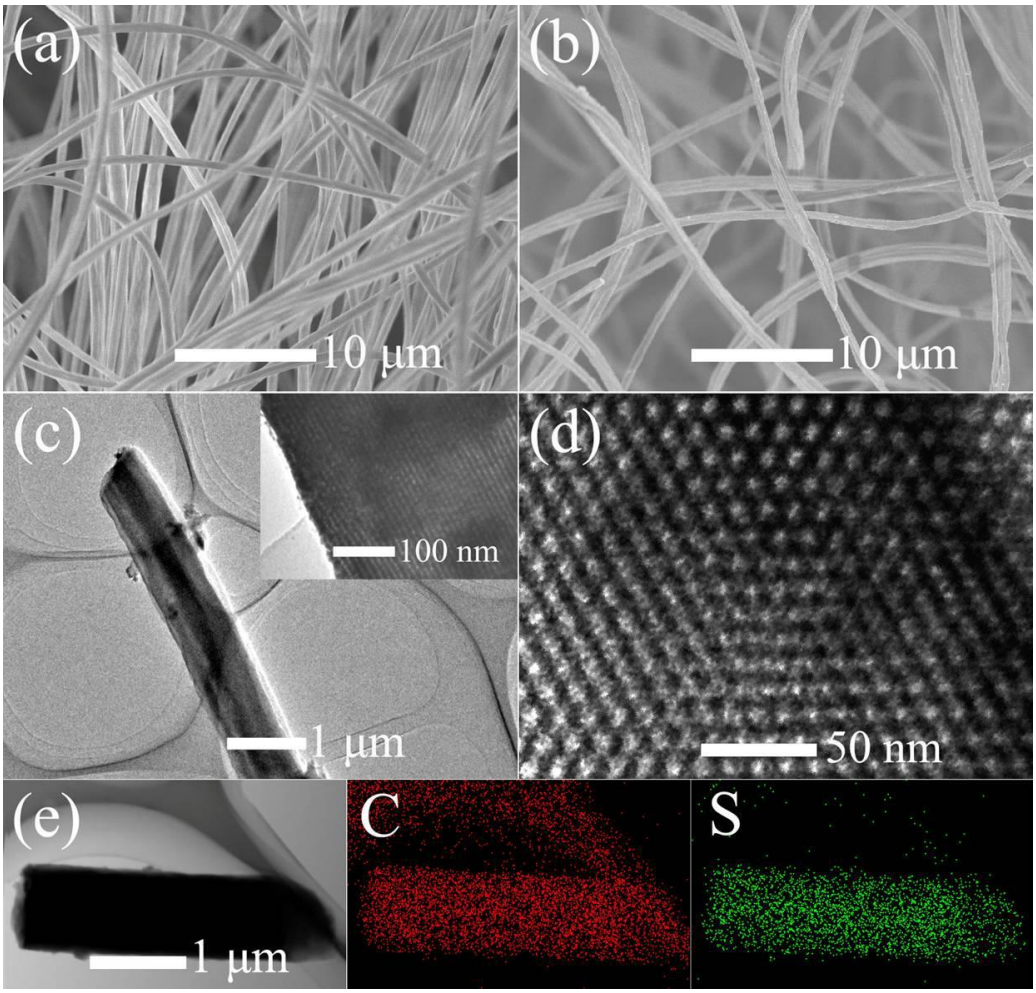

Figure 6.2 SEM images of (a) electrospun resol/F127/TEOS/PVB fiber and (b) OMCF; TEM images of OMCF at (c) low magnification, with the inset and (d)

showing high magnification; (e) STEM image of OMCF-S and corresponding elemental mapping images of C and S.

The N_2 sorption isotherms in Figure 6.3 (a) illustrate the variation in the structural features of the OMCF before and after sulfur loading. The isotherms of the OMCF and OMCF-S are type IV isotherms with hysteresis at relative pressure above 0.4, which is characteristic of mesopores.

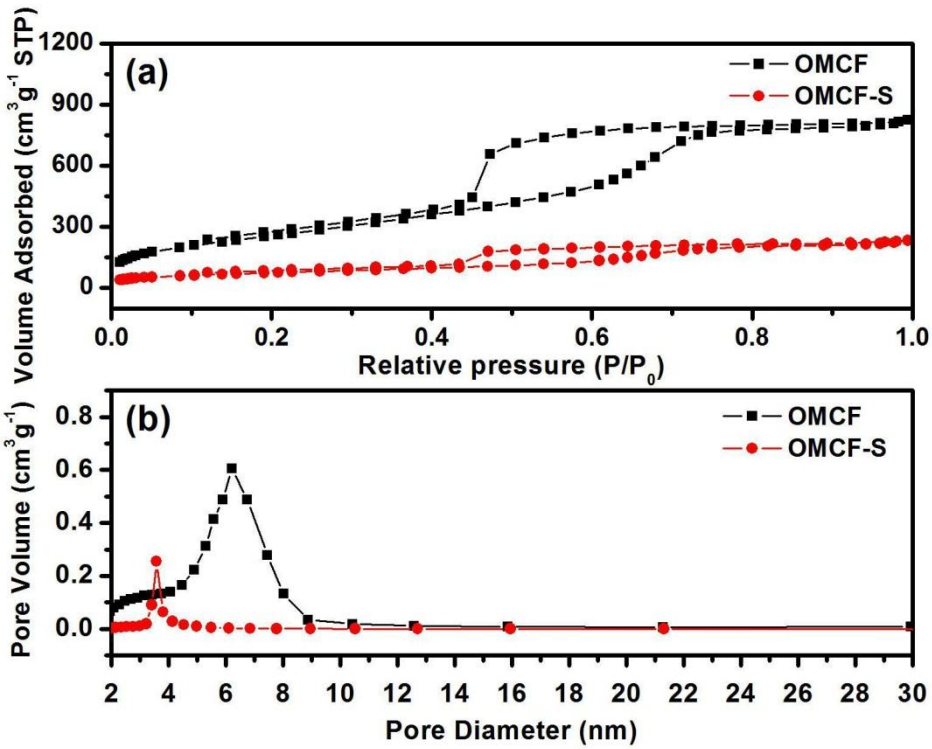

Figure 6.3 (a) N_2 sorption isotherms and (b) pore-size distributions of the OMCF and OMCF-S composite.

The OMCF host exhibits a high specific surface area of 1345 m^2 g^{-1} and a large pore volume of 1.21 cm^3 g^{-1}. After the sulfur is embedded, the surface area and pore volume decrease to 335 m^2 g^{-1} and 0.41 cm^3 g^{-1}, respectively. Meanwhile, the pore size in Figure 6.3 (b) displays a strong decrease as well, from 6.2 nm to 3.5 nm. This

indicates that a large proportion of the mesopores are filled with sulfur. The amount of sulfur in the OMCF-S composite is 63 wt%.

The XRD patterns for the OMCF, S, and OMCF-S are shown in Figure 6.4 (a). The low intensity and the high peak broadening are typical feature of amorphous carbon in the OMCF sample. No peaks corresponding to silica can be observed, suggesting that silica has been removed completely from the composite. In contrast, the pure elemental sulfur has well-defined diffraction peaks, corresponding to an orthorhombic structure. Although there is a substantial amount of sulfur (63%) in the OMCF-S composite, the signature peaks of elemental sulfur were not observed, indicating that the embedded sulfur in the composite exists in the form of small molecules and thus loses its characteristic of orthorhombic structure. This suggests good dispersion of the S within the porous carbon host [31]. Raman spectra of OMCF, S, and OMCF-S composite were also carried out to further observe their structure in Figure 6.4 (b). Sulfur shows a series of typical Raman peaks which can be assigned to the S-S bond [32], however, such typical sulfur peaks disappeared in the OMCF-S, indicating that sulfur is successfully embedded into the pores of the OMCF.

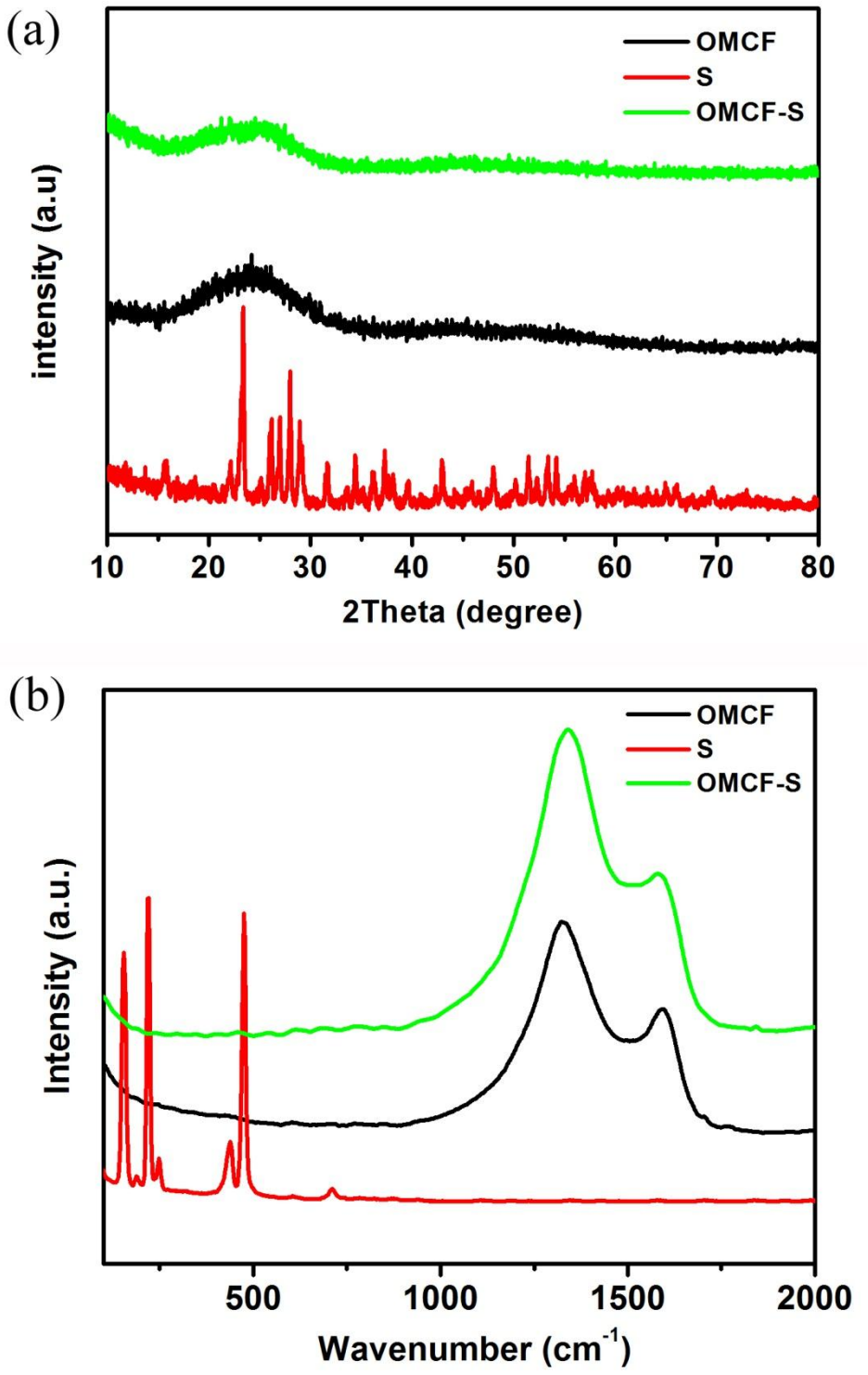

Figure 6.4 (a) XRD patterns and (b) Raman spectra of the OMCF, S, and OMCF-S composite.

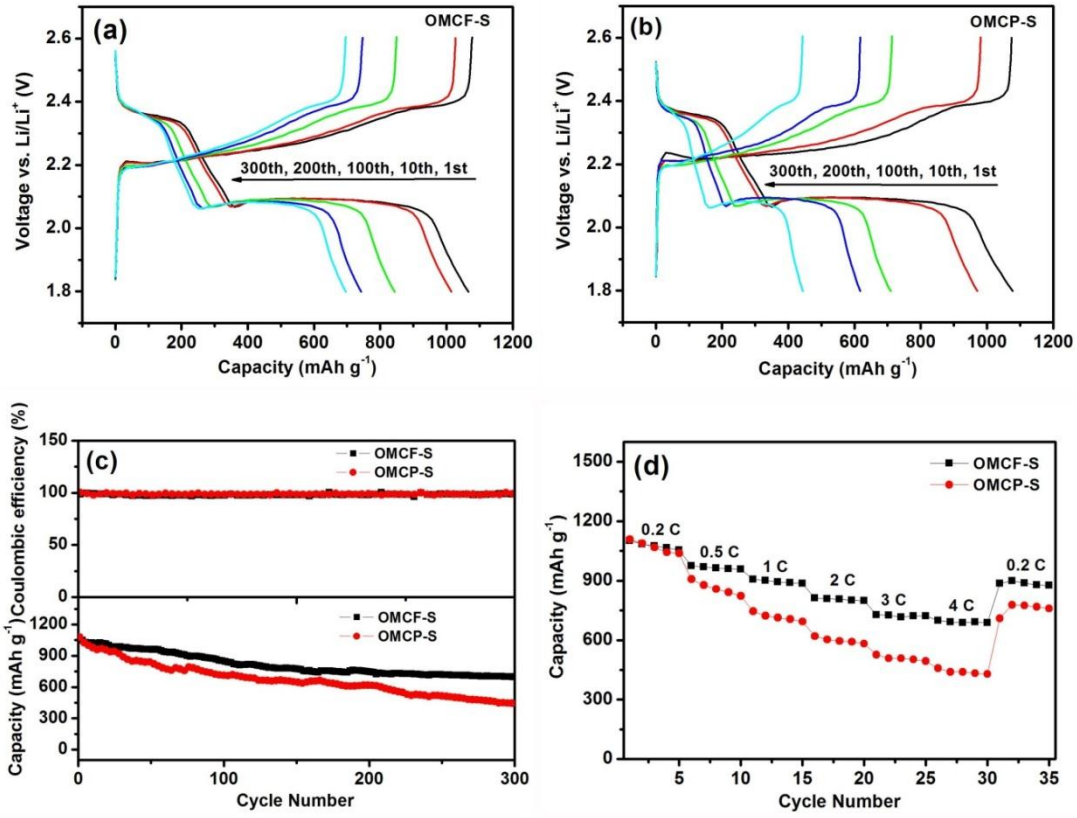

Figure 6.5 Voltage profiles of (a) OMCF-S and (b) OMCP-S for selected cycles; (c) cycling performances of OMCF-S and OMCP-S electrodes at 0.3 C; (d) rate capabilities of OMCF-S and OMCP-S electrodes.

Voltage profiles of the OMCF-S electrodes at various cycles are shown in Figure 6.5 (a). The control sample OMCP-S powder was synthesized through the same process as the OMCF, but without electrospinning technique. The OMCP also shows ordered mesoporous structure with pore size of about 7 nm (Figure 6.6 and Figure 6.7). The upper plateau at 2.3 V corresponds to the reduction of sulfur (S_8) to soluble lithium polysulfides (Li_2S_4), and the lower plateau at 2.1 V represents the further reduction of polysulfides to Li_2S_2 or Li_2S [3,19,33].

The discharge plateau of the OMCP-S composite electrode (in Figure 6.5 (b)) obviously shrinks with increased cycle number, however, the OMCF-S electrode has a good overlap of discharge plateaus during the cycling tests, suggesting the excellent stability and reversibility of the OMCF-S electrode. Figure 6.5 (c) displays the cycling performances of the OMCF-S and OMCP-S electrodes. The initial discharge capacities for the OMCF-S and OMCP-S electrodes were 1070 and 1080 mAh g^{-1} at 0.3 C, respectively. After 300 cycles, the OMCF-S electrodes retained a reversible capacity of 690 mAh g^{-1}, while only 450 mAh g^{-1} was left for the OMCP-S electrode. Even at the rate of 1 C, the OMCF-S electrodes can still maintain 570 mAh g^{-1} after 500 cycles, as shown in Figure 6.7, indicating a superior cycling performance compared to that of OMCP-S electrodes. The rate capability of the OMCF-S and OMCP-S electrodes is displayed in Figure 6.5 (d). The discharge capacity gradually reduced with the increase of rate from 0.2 C to 4 C. The OMCF-S electrode delivered a satisfactory capacity of 700 mAh g^{-1}, even at 4 C, but only a capacity of 440 mAh g^{-1} was obtained for OMCP-S electrode. The 1D interwoven fibrous mesoporous nanostructure with small dimension and large surface area can provide an effective conductive network for sulfur and polysulfides and facilitate the efficient contact between active materials and electrolyte. The ordered mesoporous structure can also effectively restrain the diffusion of long-chain polysulfides during cycling process. In addition, 1D architecture also possesses favourably structure stability, which can help to alleviate the structure damage caused by volume expansion and to keep the

integrity of the electrodes during the cycling process especially for long cycles. All these features result in such a good cycling and rate capabilities performance.

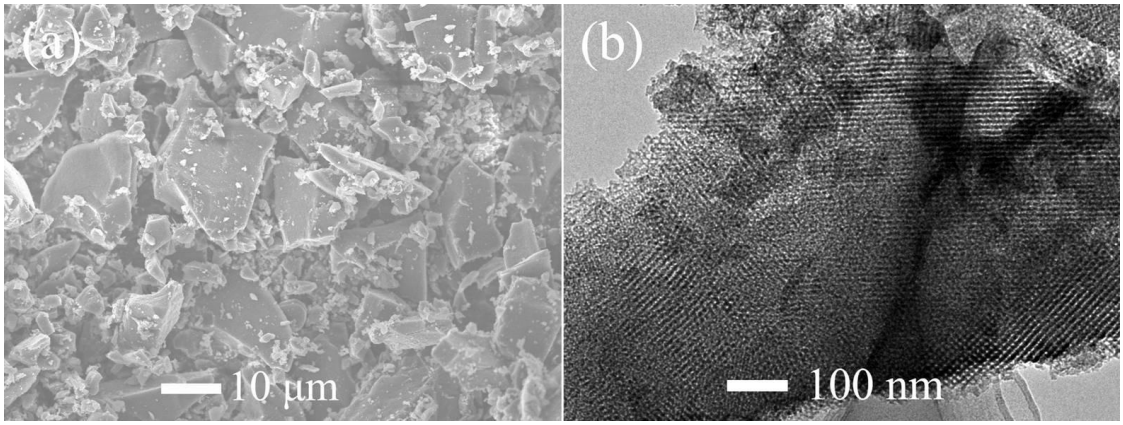

Figure 6.6 (a) SEM and (b) TEM image of OMCP.

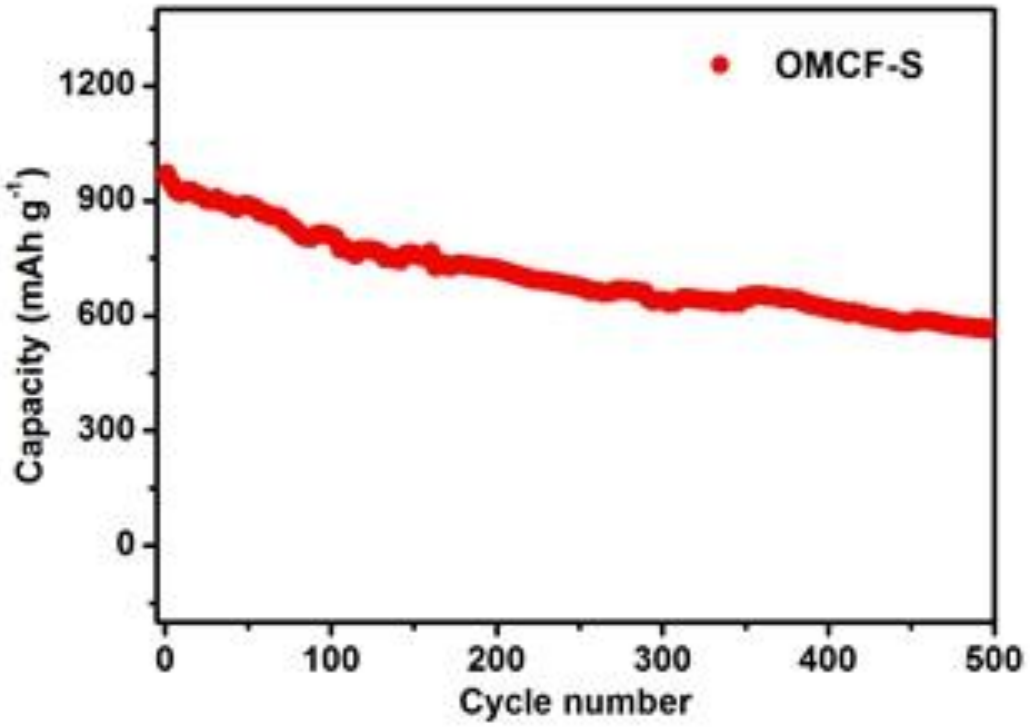

Figure 6.7 Cycling performances of OMCF-S electrodes at 1 C.

Figure 6.8 shows the CV profiles of the OMCF-S cell in the voltage range of 1.8-2.6 V with a scanning rate of 0.2 mV s^{-1}. Typical reduction and oxidation peaks representing for reaction of sulfur with lithium during the charge-discharge processes

can be observed [19,34]. The sharp redox peaks with stable overlapping features confirm the high reversibility and excellent stability of electrode after first cycle [20,35]. The electrochemical impedance spectroscopy (EIS) analysis for the OMCF-S electrode was also carried out are shown in Figure 6.9. All the EIS curves show a semicircular loop whose diameter represents the charge-transfer resistance. The semicircle at high frequency is associated with the charge transfer resistance (R_{ct}) of the sulfur electrode, which is mainly generated at the interface between the electrode and the electrolyte [36,37]. The electrolyte resistance R_{ct} remained unchanged even after 300 cycles, indicating that polysulfides were well constrained in the cathode and to the dissolution of polysulfides into electrolyte and the increase of viscosity were successfully avoided. The R_{ct} is stabilized at around 150 Ω cm^2 (calculated after the electrode area normalization) after the first cycle, suggesting a stable electrochemical environment in the batteries.

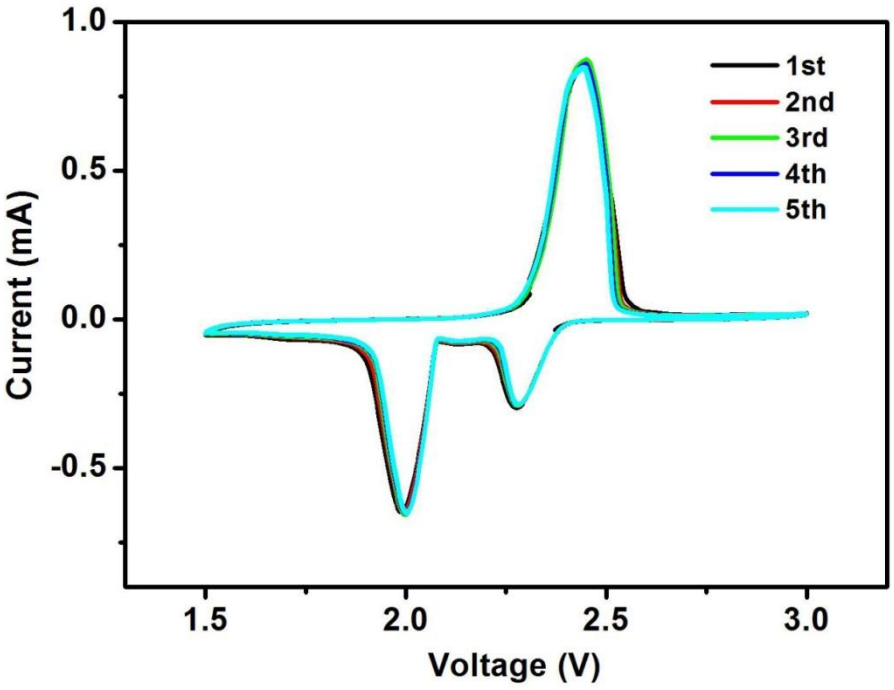

Figure 6.8 CV curves of the OMCF-S electrode before cycling.

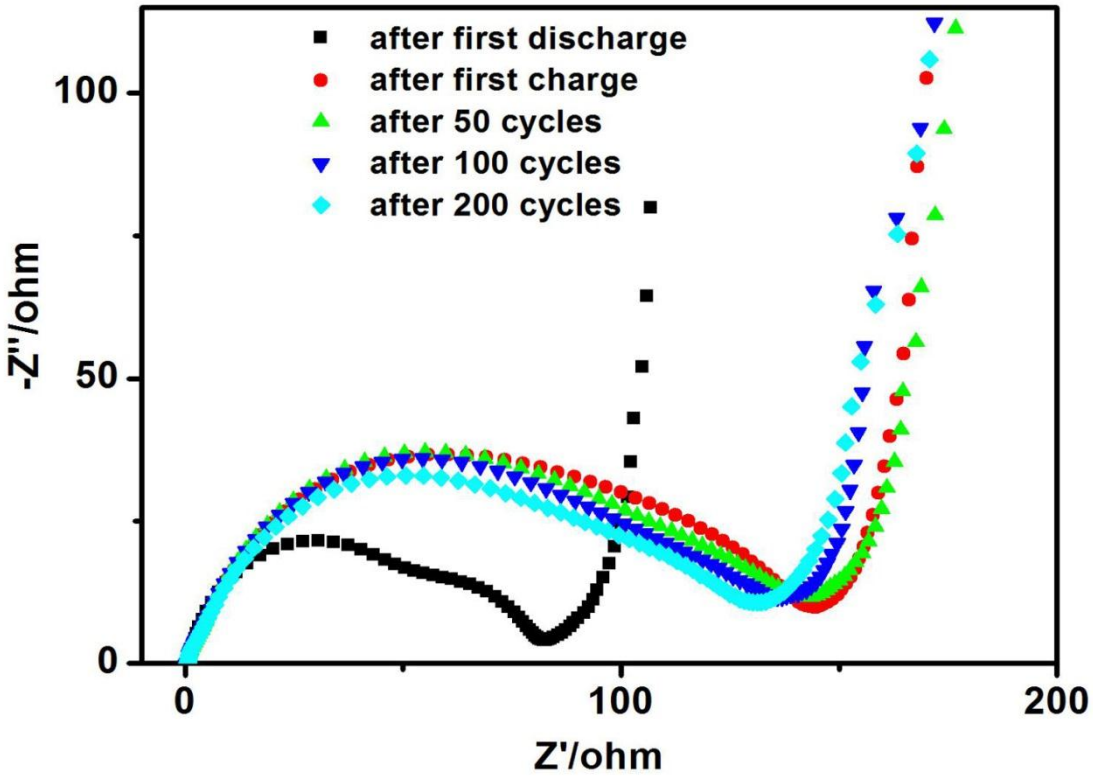

Figure 6.9 EIS spectra of the OMCF-S electrodes after cycles.

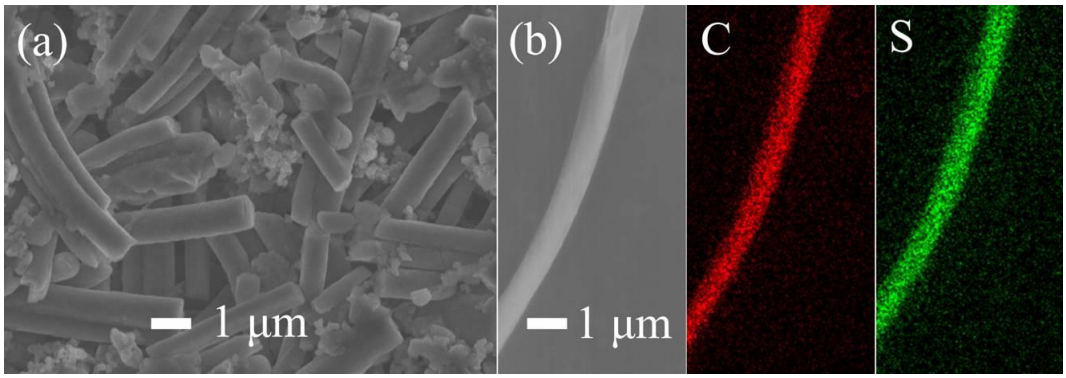

Figure 6.10 SEM images of (a) OMCF-S electrode after 100 cycles, and (b) corresponding elemental map images of carbon, and sulfur.

To further investigate the reason why the OMCF-S electrode shows enhanced performance of the lithium-sulfur battery compared to OMCP-S electrode, the microstructure of the OMCF-S electrode after 100 cycles for Li-S batteries was examined by SEM. The fibrous structure is still maintained is shown in the Figure 6.10, and no obvious change is observed. The elemental mapping results show that sulfur is still homogeneously distributed throughout the whole fiber, suggesting the excellent mechanical stability of the OMCF-S, which makes a great contribution to excellent electrochemical properties of OMCF-S electrode together with its ordered mesoporous structure.

6.4 Conclusions

In summary, ordered mesoporous carbon fibers were synthesized by the electrospinning technique and used to fabricate carbon-sulfur composite, which was then explored as a cathode material for lithium-sulfur batteries. Not only can the ordered mesoporous structure ensure good electrical pathways for the active sulfur, but it also can effectively trap soluble polysulfide intermediates during

charge-discharge processes. In addition, the OMCF-S composite has excellent mechanical stability during charge-discharge process. All the features lead to excellent electrochemical performance for OMCF-S electrode (690 mAh g^{-1} even after 300 cycles). In particular, the OMCF can be mass produced in a simple way at low cost, which makes our sulfur-based electrode highly promising for practical application in lithium-sulfur batteries.

6.5 References

[1] S. E. Cheon, S. S. Choi, J. S. Han, Y. S. Choi, B. H. Jung, H. S. Lim, Journal of the Electrochemical Society, 151 (2004) A2067-A2073.

[2] P. G. Bruce, S. A. Freunberger, L. J. Hardwick, J. M. Tarascon, Nature Materials, 11 (2012) 19-29.

[3] J. Shim, K. A. Striebel, E. J. Cairns, Journal of the Electrochemcial Society, 149 (2002) A1321-A1325.

[4] P. Novak, K. Muller, KSV. Santhanam, O. Haas, Chemical Reviews, 97 (1997) 207-281.

[5] Y. Yang, G. Y. Zheng, S. Misra, J. Nelson, M. F. Toney, Y. Cui, Journal of the American Chemical Society, 134 (2012) 15387-15394.

[6] Y. V. Mikhaylik, J. R. Akridge, Journal of the Electrochemcial Society, 151 (2004) A1969-1976.

[7] W. Ahn, K. B. Kim, K. N. Jung, K. H. Shin, C. S. Jin, Journal of Power Sources, 202 (2012) 394-399.

[8] H. L. Wang, Y. Yang, Y. Y. Liang, J. T. Robinson, Y. G. Li, A. Jackson, Y. Cui, H. J. Dai, Nano letters, 11 (2011) 2644-2647.

[9] B. L. Ellis, K. T. Lee, L. F. Nazar, Chemistry of Materials, 22 (2010) 691-714.

[10] J. C. Guo, Y. H. Xu, C. S. Wang, Nano Letters, 11 (2011) 4288-4294.

[11] H. B. Wu, S. Y. Wei, L. Zhang, R. Xu, H. H. Hng, X. W. Lou, Chemistry A European Journal, 19 (2013) 10804-10808.

[12] B. S. Lee, S. B. Son, K. M. Park, G. Lee, K. H. Oh, S. H. Lee, ACS Applied Materials & Interfaces, 4 (2012) 6701-6709.

[13] C. F. Zhang, H. B. Wu, C. Yuan, Z. P. Guo, X. W. Lou, Angewandte Chemie International Edition, 51 (2012) 9592-9595.

[14] S. Y. Zheng, Y. Chen, Y. H. Xu, F. Yi, Y. J. Zhu, Y. H. Liu, J. H. Yang, C. S. Wang, ACS Nano, 7 (2013) 10995-11003.

[15] M. S. Park, B. O. Jeong, T. J. Kim, S. Kim, K. Y. Kim, J. S. Yu, Y. Jung, Y. J. Kim, Carbon, 68 (2014) 265-272.

[16] N. Jayaprakash, J. Shen, S. S. Moganty, A. Corona, L. A. Archer, Angewandte Chemie International Edition, 50 (2011) 5904-5908.

[17] N. W. Li, M. B. Zheng, H. L. Lu, Z. B. Hu, C. F. Shen, X. F. Chang, Chemical Communications, 48 (2012) 4106-4108.

[18] L. W. Ji, M. Rao, H. M. Zheng, L. Zhang, Y. C. Li, W. H. Duan, Journal of the American Chemical Society, 133 (2011) 18522-18525.

[19] J. Z. Wang, L. Lu, M. Choucair, J. A. Stride, X. Xu, H. K. Liu, Journal of Power Sources, 196 (2011) 7030-7034..

[20] L. F. Xiao, Y. L. Cao, J. Xiao, B. Schwenzer, M. H. Engelhard, L. V. Saraf, Advanced Materials, 24 (2012) 1176-1181.

[21] Y. Yang, G. H. Yu, J. J. Cha, H. Wu, M. Vosgueritchian, Y. Yao, ACS Nano, 5 (2011) 9187-9193.

[22] Z. W. Seh, W. Y. Li, J. J. Cha, G. Y. Zheng, Y. Yang, M. T. Mcdowell, Nature Communications, 4 (2013) 1331.

[23] H. Kim, J. T. Lee, D. C. Lee, A. Magasinski, W. I. Cho, G. Yushin, Advanced Energy Materials, 3 (2013) 1308–1315.

[24] S. S. Zhang, D. T. Tran, Electrochimica Acta, 114 (2013) 296-302.

[25] W. Weng, V. G. Pol, K. Amine, Advanced Materials, 25 (2013) 1608-1615.

[26] N. Azimi, W. Weng, C. Takoudis, Z. C. Zhang, Electrochemistry Communications, 37 (2013) 96-99.

[27] Y. S. Su, A. Manthiram, Nature Communications, 3 (2012) 1166.

[28] Y. S. Su, A. Manthiram, Chemical Communications, 48 (2012) 8817-8819.

[29] X. G. Han, Y. H. Xu, X. Y. Chen, Y. C. Chen, N. Weadock, J. Y. Wan, Nano Energy, 2 (2013) 1197-1206.

[30] C. F. Xue, B. Tu, D. Y. Zhao, Advanced Functional Materials, 18 (2008) 3914-3421.

[31] C. Lai, X. Gao, B. Zhang, T. Yan, Z. Zhou. The Journal of Physical Chemistry C, 113 (2009) 4712-4716.

[32] A. T. Ward, The Journal of Physical Chemistry, 72 (1968) 4133-4139.

[33] L. X. Yuan, J. K. Feng, X. P. Ai, Y. L. Cao, S. L. Chen, H. X. Yang, Electrochemistry Communications, 8 (2006) 610-614.

[34] GM Zhou, DW Wang, F Li, PX Hou, LC Yin, C Liu, Energy & Environmental Science, 5 (2012) 8901-8906.

[35] G. C. Li, G. R. Li, S. H. Ye, X. P. Gao, Advanced Energy Materials, 2 (2012) 1238-1245.

[36] S. S. Zhang, Electrochimica Acta, 70 (2012) 344-348.

[37] L. X. Yuan, X. P. Qiu, L. Q. Chen, W. T. Zhu, Journal of Power Sources, 189 (2009) 127-132.

7 A STRATEGY FOR CONFIGURATION OF AN INTEGRATED FLEXIBLE SULFUR CATHODE FOR HIGH-PERFORMANCE LITHIUM-SULFUR BATTERIES

7.1 Introduction

Lithium-sulfur (Li-S) batteries show great potential for the next generation of lithium-ion batteries, as sulfur features high theoretical capacity (1675 mAh g^{-1}), high specific energy density (2600 Wh kg^{-1}), cost effectiveness, and nontoxicity [1-3]. Nevertheless, the broad application of Li-S batteries is limited by several persistent problems, including the low electronic conductivity of sulfur and its discharge product, the high solubility and diffusivity of polysulfide intermediates in organic electrolytes, and the related side reaction "shuttle effect", as well as volume expansion caused by the intercalation of Li into the sulphur [4-7]. Therefore, the key points for the development of Li-S batteries are to improve the conductivity of the sulfur cathode, enhance the tolerance for volume expansion, maintain the soluble polysulfides within the cathode region and limit polysulfides diffusion. In the past few years, much effort has been devoted to addressing these scientific issues by constructing nanostructured sulfur composite cathodes, so as to confine the sulfur or lithium polysulfide within a conductive framework, consisting of such materials as nanoporous carbon [8-12], graphene [13,14], conductive polymer [15-17], and metal oxides [5,18-21]. Although employing a matrix to constrain the sulfur could significantly improve the conductivity and alleviate the dissolution of polysulfides, there is still a significant amount of polysulfides dissolved into the electrolyte, especially under long cycling

and high sulfur loading. Recently, novel configurations of Li-S cell have been considered as an alternative approach to address the shuttle effect [22-27]. Many advanced interlayers fabricated from microporous carbon [23], carbon nanotubes [24], carbon nanofibers [25], graphene [26], and carbonized paper have been inserted between the cathode and separator in the cell configuration, which could greatly decrease the internal charge transfer resistance and trap the soluble polysulfides, resulting in improved utilization efficiency of the active materials and enhanced cyclability of batteries. On the other hand, functionalizing the separator in Li-S batteries is also an effective route to preventing the diffusion of polysulfides across the separator. This can be achieved by introducing a coating layer on the cathode side of separator, such as with Nafion-coated, carbon-coated and graphene-oxide-coated separators [28-32], in order to localize the polysulfides in the cathode region, thus improving the cycling stability and rate capability. A complicated synthesis process and significant additional cost would be introduced in applying these strategies, however, so a much simpler and more cost effective construction would be more desirable for the large-scale fabrication and real application.

Inspired by this need, herein, we have designed for the first time an integrated flexible cathode architecture consisting of carbon/sulfur/carbon sandwich structure spread directly on a polypropylene (PP) separator (CSC@separator) via the simple doctor blading technique, in which commercial sulfur and Super P carbon (surface area of 64.56 $m^2 g^{-1}$, Figure 7.1) are used as the raw materials directly to be directly coated on the PP separator as the sulfur layer and carbon layers, respectively.

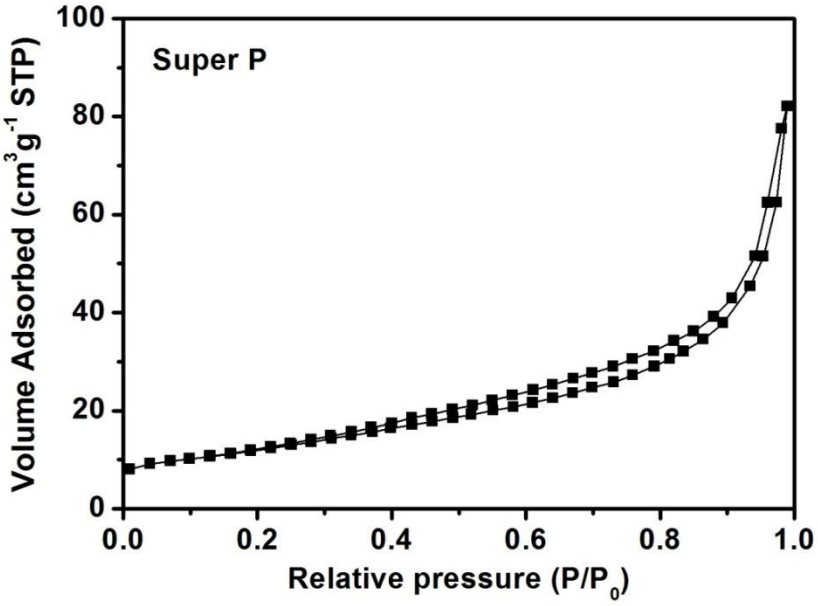

Figure 7.1 N_2 isotherm of Super P.

7.2 Experimental Section

7.2.1 Preparation of sulfur active material

Commercial conductive carbon (Super P) and sulfur were mixed together in weight ratios of 15:85 and 7:3, respectively, and heated to 160 ^{o}C in a sealed stainless steel autoclave for 24 h to facilitate sulfur diffusion into the carbon host. The content of sulfur in the composite determined by thermal gravimetric analysis is up to 81% and 63 %, respectively.

7.2.2 Fabrication of CSC@separator cathode

The integrated CSC@separator electrode was fabricated by the slurry casting technique on one side of a Celgard 2400 polypropylene (PP) separator. The slurry C for the carbon coating layer was prepared by mixing Super P and polyvinylidene difluoride (PVDF) in N-methyl-2-pyrrolidinone (NMP). The slurry S for the sulfur

layer was synthesized by mixing sulfur active material (81%, sulfur content) and binder without any additional conductive carbon in the weight ratio of 85:15. In a typical procedure, slurry C was coated on one side of the PP separator using blade coating method. After drying at 60 ^{o}C for 24 h, slurry S was coated on the surface of the carbon layer, and then another carbon layer was coated on the surface of sulfur layer after drying to obtain the integrated CSC@separator cathode. The weight of two carbon coating layers is only 0.38-0.52 mg cm^{-2}, much lighter than the weight of the sulfur layer at 1.0-1.4 mg cm^{-2}. Even including the weight of the carbon coating layers, the content of sulfur in the whole electrode is still around 50%.

7.2.3 Fabrication of S@Al foil cathode

For comparison, a conventional S@Al foil sulfur electrode was also prepared by the casting method. A slurry was made of the sulfur active material (63%, sulfur content), Super P, and binder in a certain weight ratio to make sure the same content of sulfur as in the CSC@separator electrode.

7.2.4 Characterization

The morphologies and structures of the as-prepared CSC@separator and S@Al foil electrodes were analysed by field-emission scanning electron microscopy (FESEM; JEOL JSM-7500FA). The load-strain curves of the pristine separator and the CSC@separator were tested using Tensile & Compression Testers (INSTRON 5943). The contents of polysulfides in the DOL/DME solutions in the cells with these electrodes after different cycle number were characterized with a UV-3600 spectrophotometer (Shimadzu).

7.2.5 Electrochemical measurements

Coin-type (CR2032) cells were assembled in an argon-filled glove box. The electrolyte used was 1 M lithium bis(trifluoromethanesulfonyl)imide in a solvent mixture of 1,3-dioxolane (DOL): dimethoxyethane (DME) (1:1, v/v), containing $LiNO_3$ (2 wt%). Cyclic voltammetry (CV) and electrochemical impedance spectroscopy (EIS) measurements were performed on a Biologic VMP3 electrochemical workstation at different scan rates. The coin cells were galvanostatically charged-discharged between 1.8 and 2.6 V (vs. Li/Li^+) by using a cell test instrument (CT2001A, LAND, China). The self-discharge behaviour of the cells employing S@Al foil and CSC@separator electrodes was measured by testing the first discharge capacity of the cells after different resting time.

7.3 Results and discussions

A schematic illustration of the cell configuration of a conventional electrode and the CSC@separator electrode is shown in Figure 7.2(a) and (b). Compared to the conventional electrode configuration, the CSC@separator electrode, where the CSC sandwich layers are directly coated on separator without any usage of aluminium (Al) foil as substrate, greatly reduces the weight of the electrode (since the weight of the substrate is reduced significantly by about 78% when the separator replaces Al foil, with 1.13 mg cm^{-2} for the separator and 5.30 mg cm^{-2} for Al foil) and exhibits excellent flexibility and high mechanical strength. The two carbon layers next to the sulfur layer could not only act as double current collectors from top to bottom to accelerate electron transport into the active material and thus to enhance sulfur

utilization, but also serve as physical barriers to buffer the volume changes caused by the conversion from sulfur to lithium polysulfides during cycling, preventing active material exfoliation and maintaining the integrity of the whole electrode. In addition, the double carbon coating layers work as effective reservoir to trap the dissolved polysulfides within the cathode region, without affecting the lithium ion diffusion, resulting in suppression of the shuttle effect and improved long-lasting cycling stability. Lastly, the utilization of commercial sulfur powders and Super P carbon as raw materials and the mature doctor blade process make it an easy, low-cost, and scalable approach.

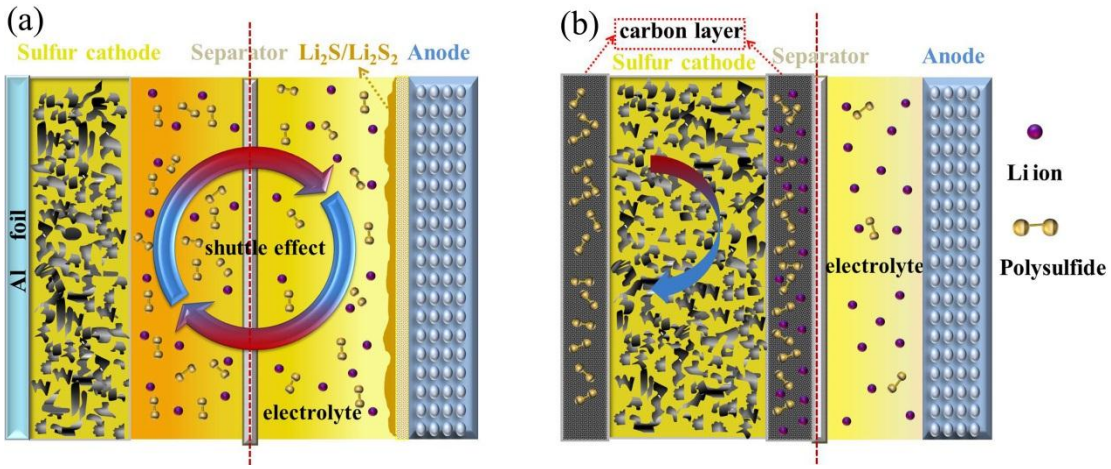

Figure 7.2 A schematic illustration of Li-S cells configuration employing (a) conventional electrode and (b) integrated sandwich structured electrode.

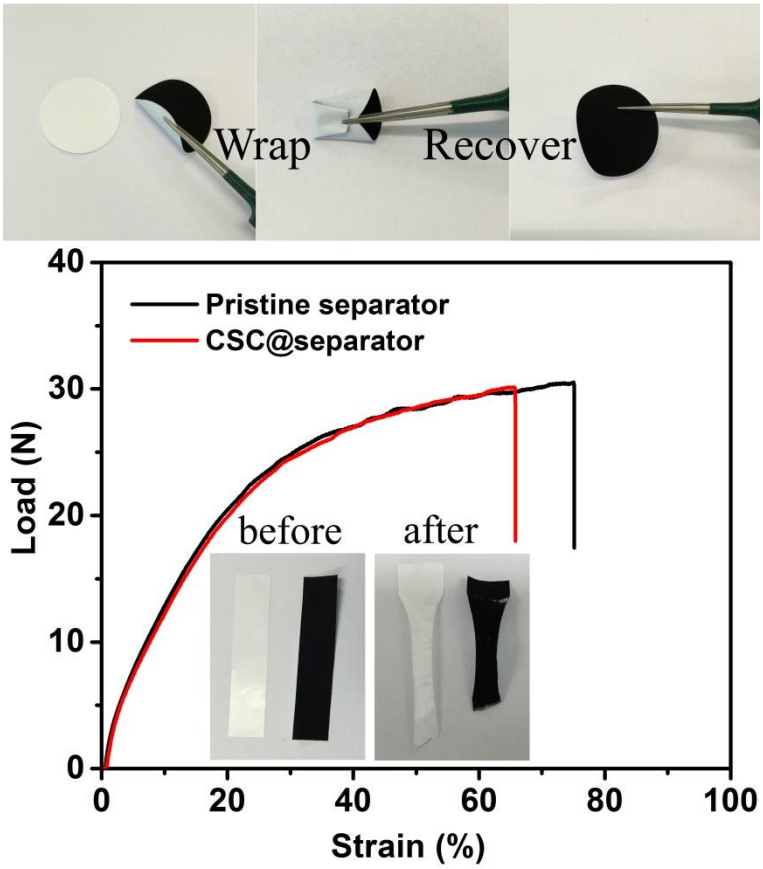

Figure 7.3 Digital photographs and load-strain curves of pristine separator and CSC@separator electrode, demonstrating excellent flexibility and high mechanical strength.

Figure 7.3 shows digital photographs of the as-prepared integrated CSC@separator electrode. The unique integrated electrode shows excellent flexibility, strong adhesion, and high mechanical strength (load-strain curve). The bare separator displays a highly nanoporous structure with pore size around several hundred nanometers, as shown in Figure 7.4 (a). In contrast, the CSC@separator electrode shows nanoparticle clusters on one side (Figure 7.4 (b)), while the other side of the electrode still keeps its nanoporous structure (Figure 7.5). The loose structure of the carbon coating layer ensures that the liquid electrolyte penetrates easily into the whole sandwich structure

and so that the electrochemical reactions proceed, which is consistent with the calculation of the lithium ion diffusion coefficient.

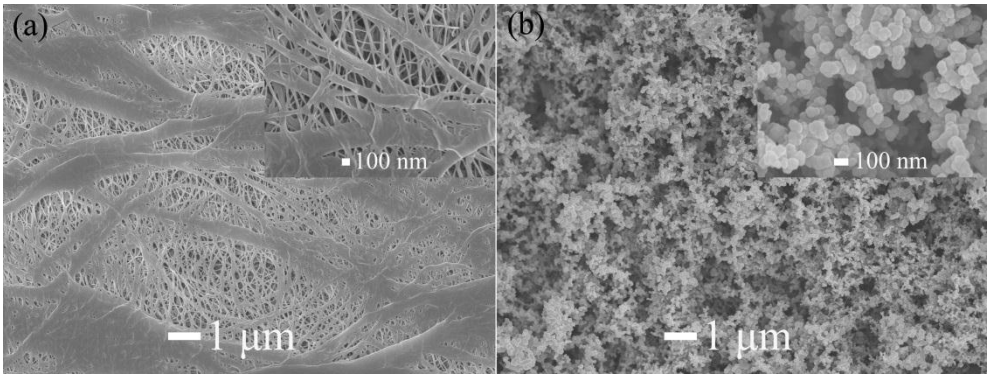

Figure 7.4 SEM images of the surface of (a) the pristine separator and (b) the CSC@separator electrode.

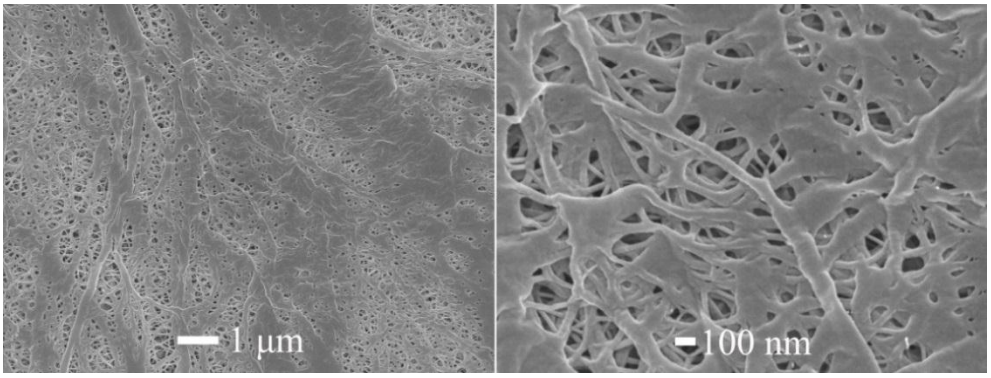

Figure 7.5 SEM images of CSC@separator electrode on the anode side.

The sandwich structure of the electrode can be further examined in the cross-sectional scanning electron microscope (SEM) image shown in Figure 7.6. The sandwich structure strongly adheres to the separator as an integrated electrode. The thicknesses of the carbon coating layers and the sulfur layer are about 10 μm and 20 μm, respectively. The elemental mapping results clearly confirm the layered carbon/sulfur/carbon sandwich structure. The weight of two carbon layers is around 0.38-0.52 mg cm^{-2}, much lighter than the weight of the sulfur layer at 1.0-1.4 mg cm^{-2}.

Even including the weight of the carbon coating layers, the content of sulfur in the whole electrode is around 50%.

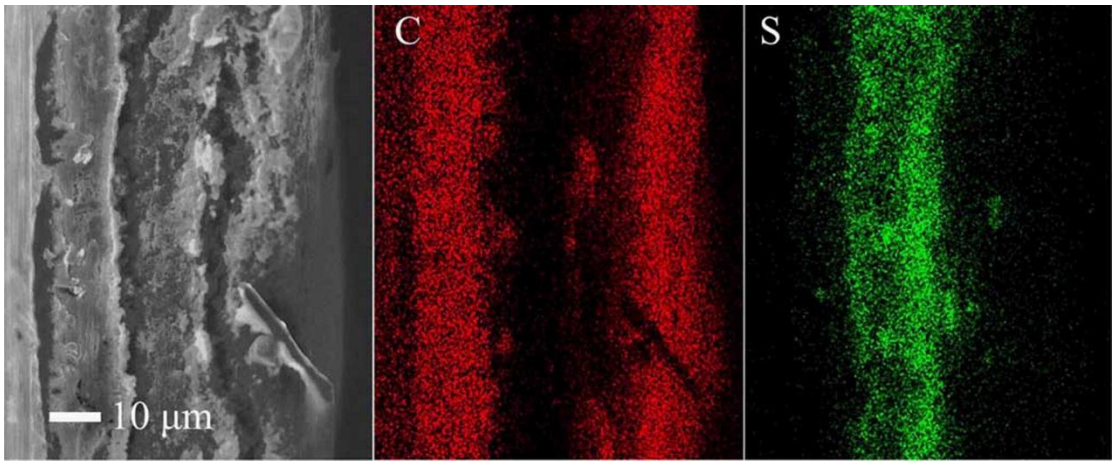

Figure 7.6 SEM images of cross-section of CSC@separator electrode and corresponding elemental mapping of carbon ad sulfur.

To demonstrate the effectiveness of this unique CSC@separator electrode, a series of electrodes were prepared for comparison, including a sulfur layer coated on the separator (S@separator), a dual sulfur/carbon layer coated on the separator (SC@separator), a dual carbon/sulfur layer coated on the separator (CS@separator), and the same sulfur content mixed with super P and binder coated on Al foil by the traditional electrode fabrication technique (S@Al foil). As shown in Figure 7.7 (a), surprisingly, all kinds of integrated separator electrodes display enhanced utilization efficiency of sulfur and cycling stability at current density of 0.2 C (1C=1000 mA g^{-1}) compared to the S@Al foil electrode. The CSC@separator electrode shows the highest reversible capacity and the best cycling stability, indicating enhanced sulfur utilization, which is attributed to the integrated structure of the electrode and decreased charge transfer resistance (Figure 7.7 (b)). Furthermore, the

CSC@separator electrode shows overlapping voltage plateaus and lower polarization compared to the conventional S@Al foil electrode (Figure 7.7 (c) and (d)). The charge-discharge potential difference (ΔE) of the cells with CSC@separator electrode remains almost constant with cycle number, while the ΔE increases with cycling for the cell with S@Al foil electrode (Figure 7.8).

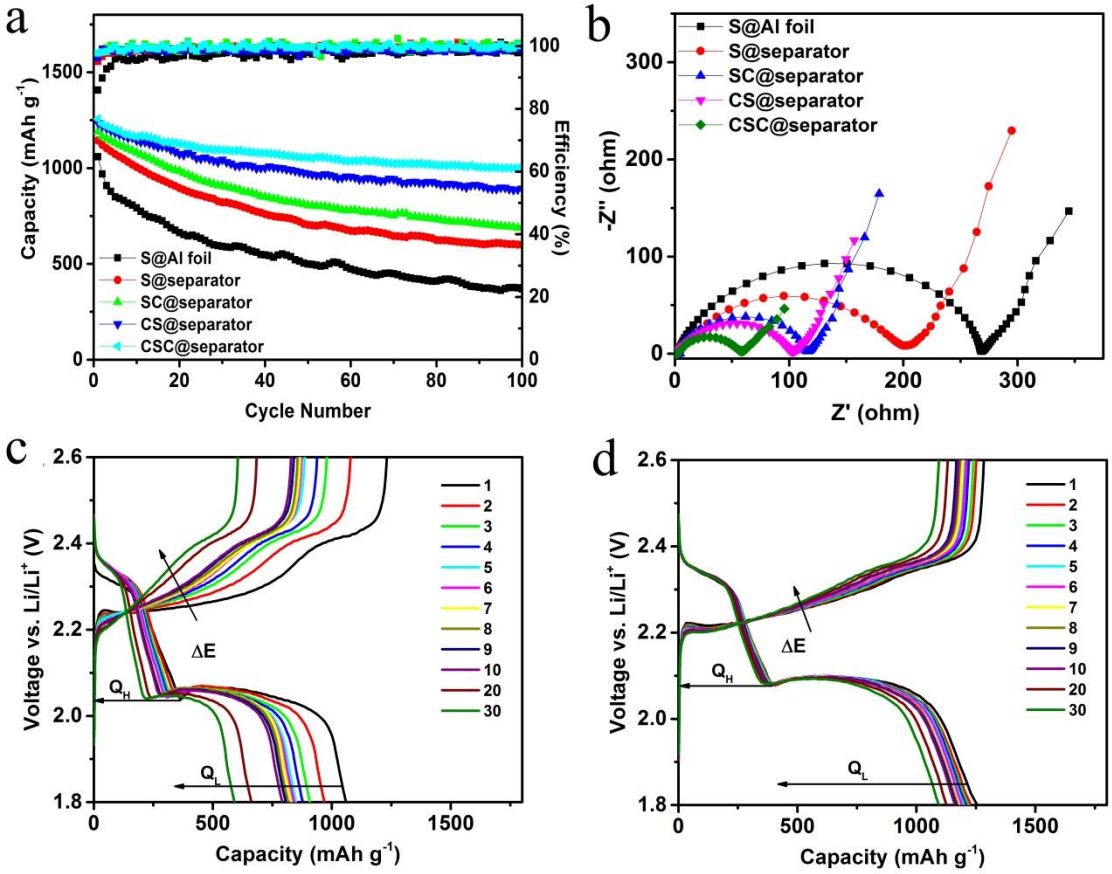

Figure 7.7 (a) Cycling stability at 0.2C (1C=1000 mA g^{-1}) and (b) electrochemical impedance spectroscopy of Li-S cells employing S@Al foil, S@ separator, SC@separator, CS@separator, and CSC@separator electrodes. Discharge-charge profiles for selected cycles of Li-S cells with (c) S@Al foil and (d) CSC@separator electrodes.

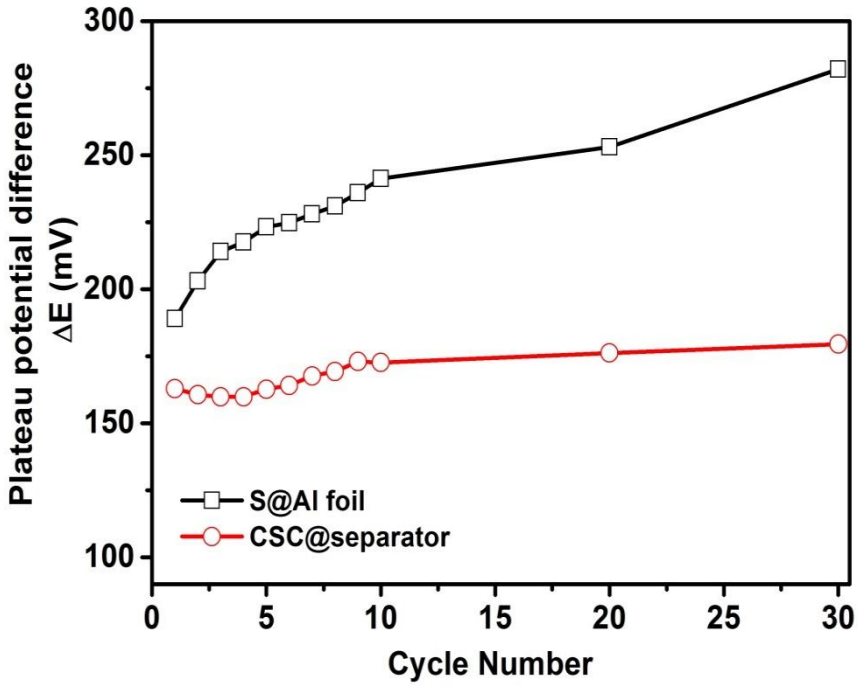

Figure 7.8 Potential difference (ΔE) between the charge and discharge plateaus at different cycle numbers for cells containing S@Al foil and CSC@separator electrodes.

A similar tendency for ΔE can be observed when the cells are tested at different current densities (Figure 7.9), indicating improved redox reaction kinetics and reversibility of the system. It was reported that the upper discharge plateau at 2.3 V represents the reduction reaction from sulfur to high-order soluble polysulfides30. Therefore, the high retention rate of discharge capacity (QH) (Figure 7.10), corresponding to the upper plateau for the CSC@separator electrode, indicates that the carbon coating layers have strong polysulfide-trapping capability.

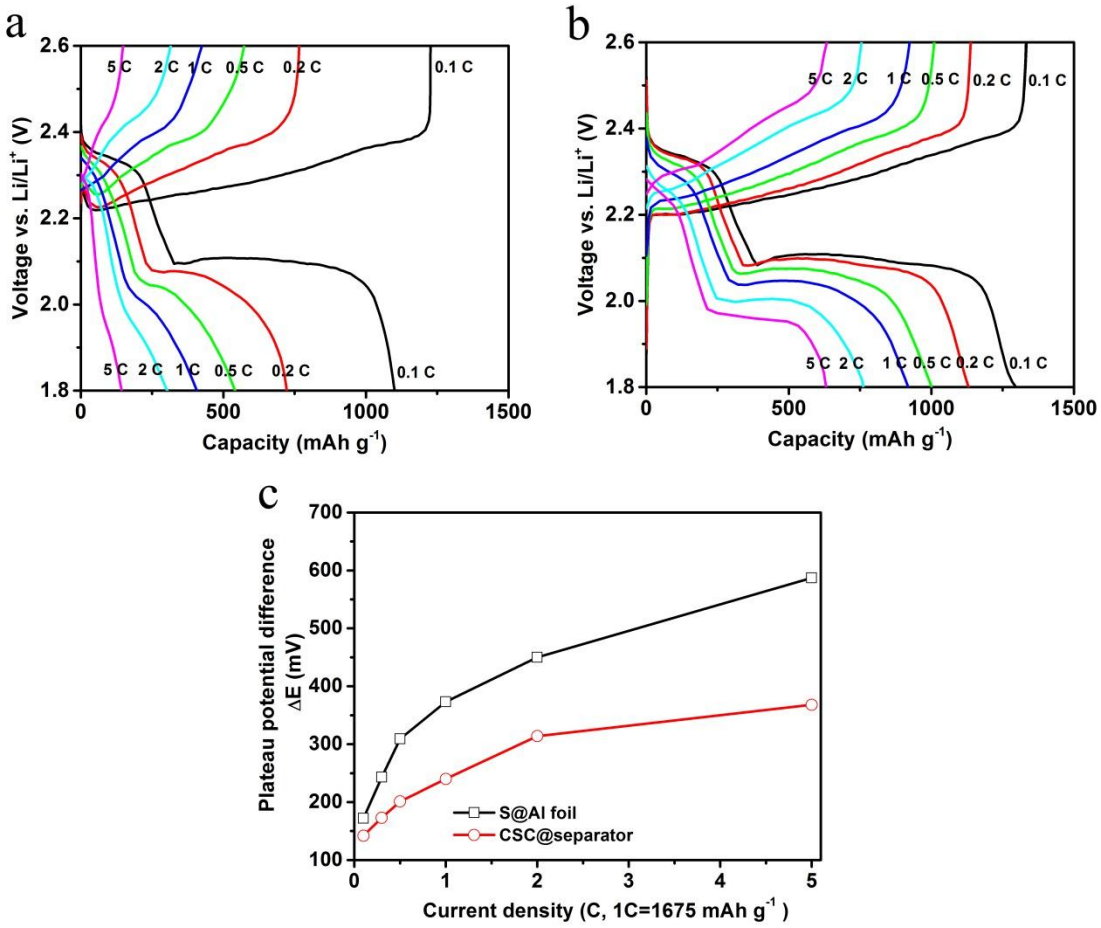

Figure 7.9 Discharge-charge curves of Li-S cells with (a) S@Al foil and (b) CSC@separator electrodes at different current densities. (c) Potential difference (ΔE) between the charge and discharge plateaus at different current densities.

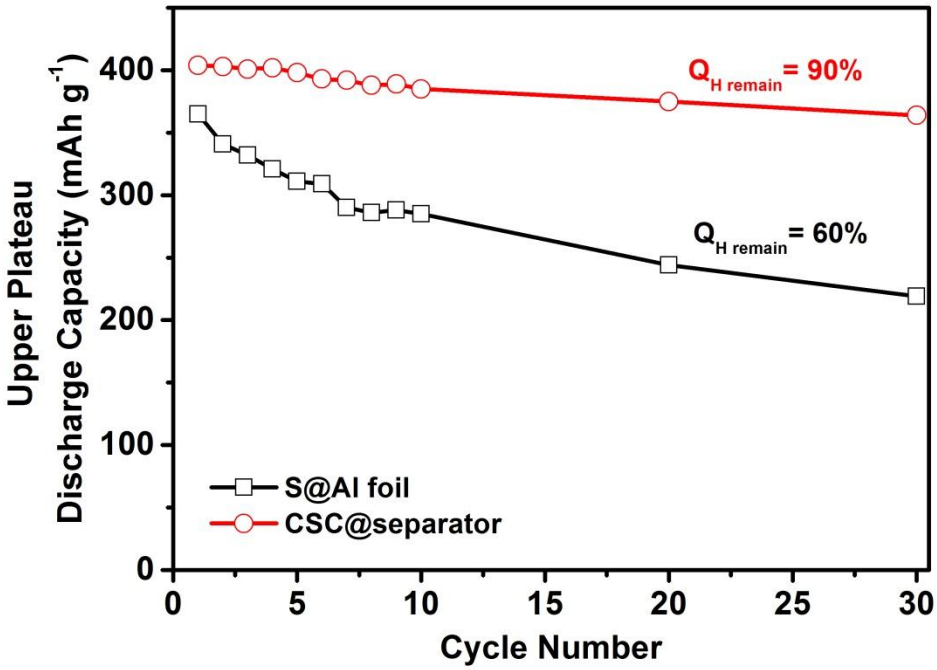

Figure 7.10 Upper plateau discharge capacity of cells using S@Al foil and CSC@separator electrodes at different cycle numbers.

The long-term cycling stability of the CSC@separator electrode was studied at 0.6 C for 500 cycles (Figure 7.10), and it was found that the capacity stabilized around 730 mAh g^{-1}, corresponding to 71.2% capacity retention of its initial capacity and a small capacity fading of only 0.058% per cycle. It is important to point out that our integrated CSC@separator electrode prepared from commercial sulfur and Super P can still exhibit such a good electrochemical performance. If nanostructured sulfur materials, such as porous carbon-sulfur composite and sulfur-TiO_2 yolk shell nanoarchitecture, can be used to as raw materials to fabricate the sulfur layer in our novel configuration design, much superior electrochemical performance could definitely be obtained.

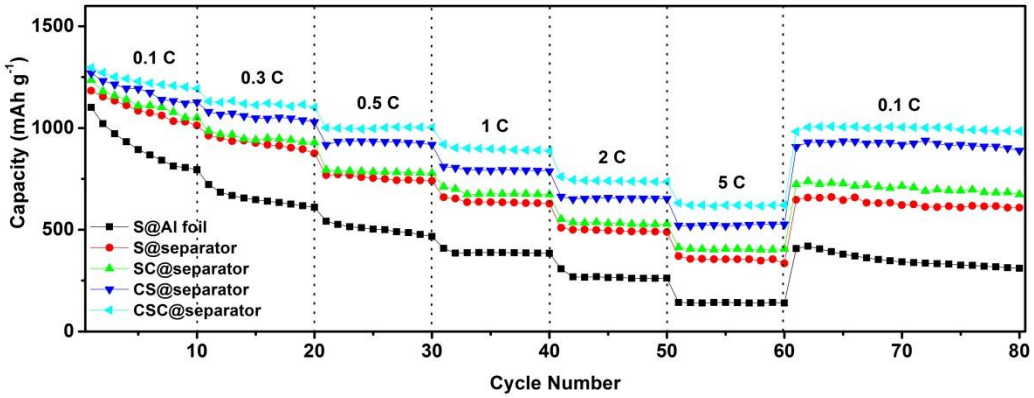

Figure 7.11 Rate capability of Li-S cells with S@Al foil, S@ separator, SC@separator, CS@separator, and CSC@separator electrodes.

Figure 7.11 displays the rate performance of S@Al foil and a series of integrated electrodes. The highly reversible CSC@separator electrode delivered capacities of 1220, 1120, 1000, 900, 740, and 620 mAh g^{-1} at 0.1, 0.3, 0.5, 1, 2, and 5 C, respectively, confirming the excellent rate capability due to the close contact between the sulfur and the carbon layers, excellent electronic transport, and improved reaction kinetics. It should be also pointed out that the introduction of the double carbon coating layers does not notably degrade the lithium ion conductivity, as confirmed by the similar diffusion coefficients of S@Al foil (1.67×10^{-8} cm^2 s^{-1} at the anodic peak at 2.45 V) and the CSC@separator electrodes (1.50×10^{-8} cm^2 s^{-1}, Figure 7.13).

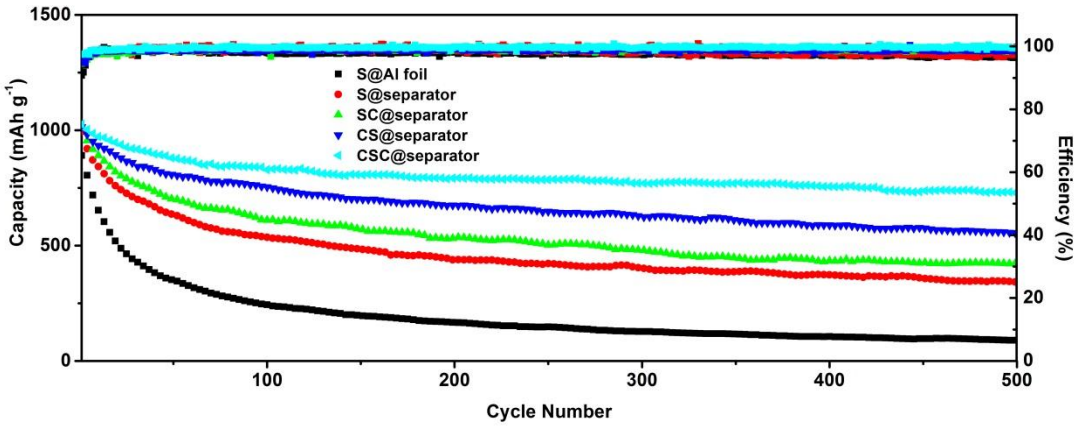

Figure 7.12 Long-term cycling performance of Li-S cells with S@Al foil, S@ separator, SC@separator, CS@separator, and CSC@separator electrodes at 0.6 C.

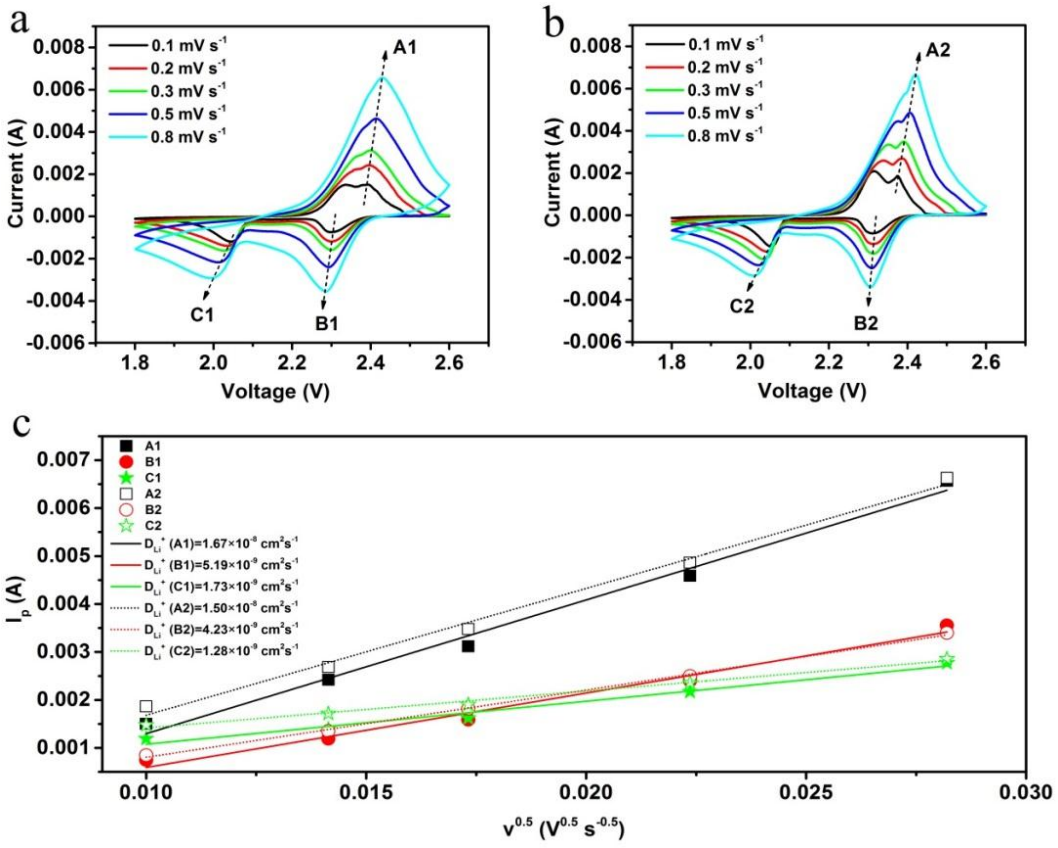

Figure 7.13 CV curves at different scan rates of Li-S cells with (a) S@Al foil and (b) CSC@separator electrodes. (c) Peak currents versus $V^{0.5}$ $s^{-0.5}$ and the corresponding linear fits.

The lithium-ion diffusion coefficient (DLi^+) can be calculated based on the Randles-Sevcik equation:

$$i_p = 0.4463nF\sqrt{\frac{nFD}{RT}}AC\sqrt{v}$$

Where ip represents peak current, n is the number of electrons, F is the Faraday constant, R is the gas constant, T is the temperature, A is the surface area of the electrode, D is the diffusion coefficient, C stands for the concentration of lithium-ions in the electrolyte, and v is the voltage scanning rate.

The integrated CSC@separator electrode also offers notable improvement of the self-discharge behaviour in Li-S batteries. The severe self-discharge behaviour mainly arises from the dissolution of sulfur during long-term storage, as can be clearly observed in the cells with S@Al foil electrode (Figure 7.14 (a) and Figure 7.15), while the cell with CSC@separator electrode shows almost repeated discharge curves (Figure 7.14 (b)), indicating that the sulfur materials are well controlled within the double carbon layers, resulting in low self-discharge constant Ks of 0.0293 per week (Figure 7.14 (c) and Table 8.1). The static electrochemical stability of the S@Al foil electrode and the CSC@separator electrodes is shown in Figure 7.14 (d) and (e). After resting for 4 weeks, the cell with CSC@separator electrode still shows good cycling stability with high initial capacity retention of 81.3%. In addition, the CSC@separator electrode after 20 cycles delivered much higher static reversible capacity after resting for 3 weeks. The significantly improved static capacity retention indicates that the double carbon coating layer in the sandwich structure serves as a protective layer for

the sulfur cathode, preventing the sulfur material from dissolving into the electrolyte and thus eliminating the severe self-discharge problem that occurs in the conventional Li-S cells.

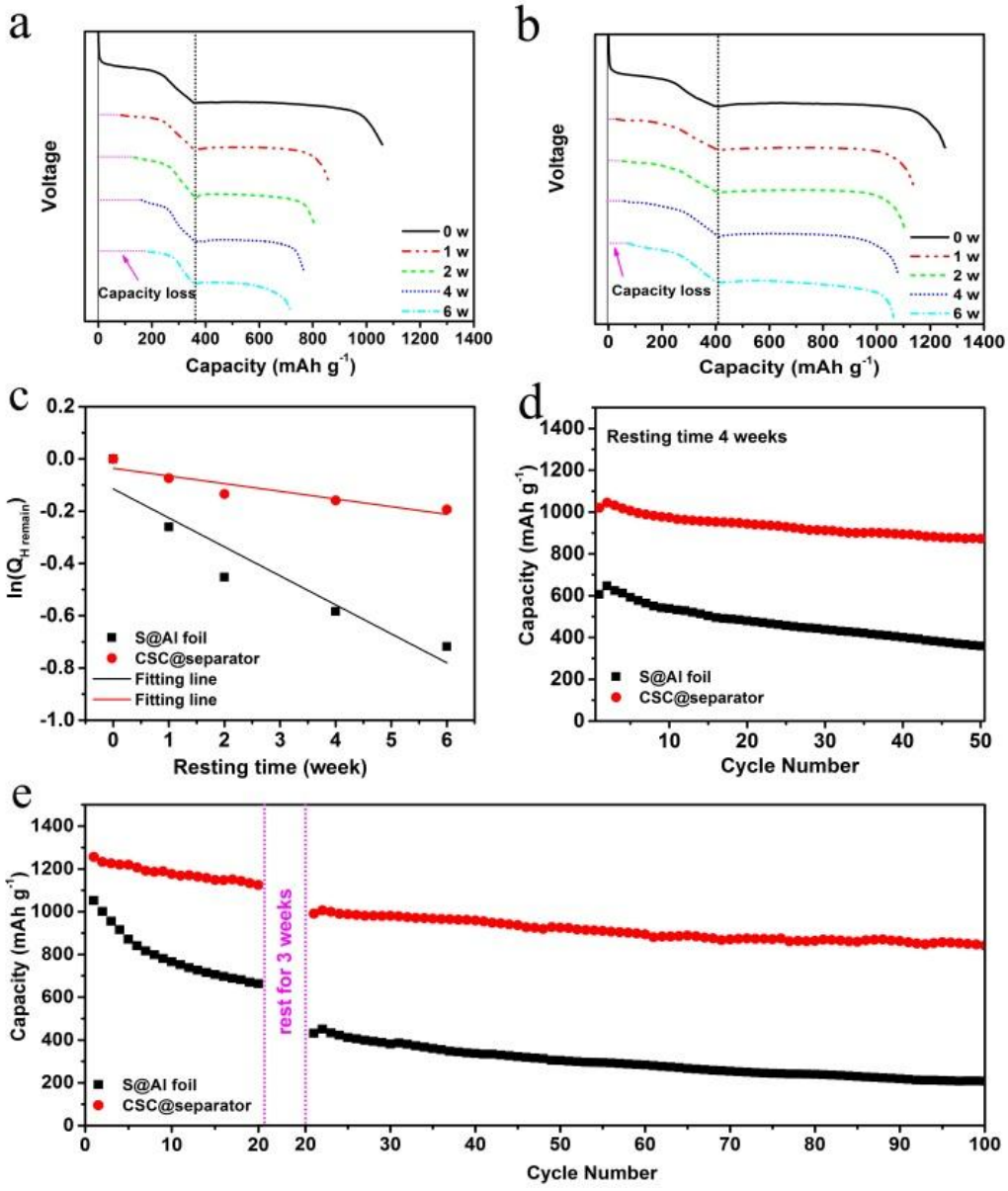

Figure 7.14 (a) Initial discharge profiles of Li-S cells with S@Al foil and (b) CSC@separator electrodes after different open-circuit durations at current density of 0.2 C. (c) Natural logarithm of the retention rate of upper plateau discharge capacity as a function of resting time for calculating the self-discharge constant. (d) Cycling

performances of the cells containing S@Al foil and CSC@separator electrodes after 4 weeks storage and (e) with 3 weeks resting time after 20 cycles at 0.2 C.

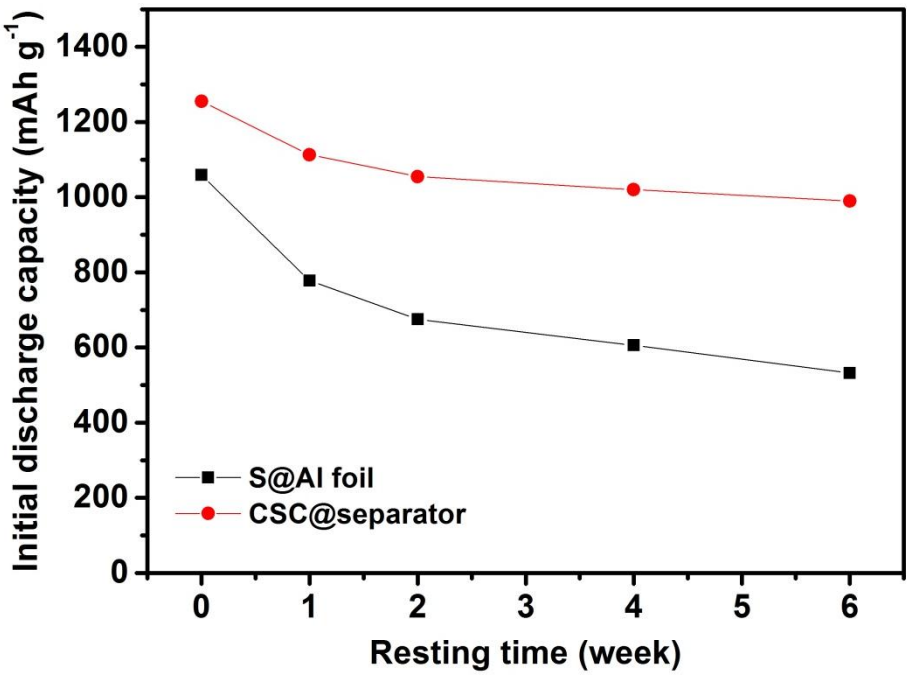

Figure 7.15 Initial discharge capacity of Li-S cells with S@Al foil and CSC@separator electrodes after different resting times.

Table 7.1 Self-discharge constant of Li-S cells with different electrodes.

Electrode	Self-discharge constant Ks (per week)
S@Al foil	0.1107
CSC@separator	0.0293

The self-discharge constant of cells containing S@Al foil and CSC@separator electrodes can be calculated by the following equation:

$$\ln(Q_{H\,remain}) = \ln\left(\frac{Q_H}{Q_{H0}}\right) = -\mathrm{K_s} \times \mathrm{T_R} \quad (1)$$

Q_H and Q_H^o are the upper plateau discharge capacity of Li-S cells without a resting time and the initial upper plateau discharge capacity of the cells after a period of storage time, respectively. Ks is the self-discharge constant, while TR stands for the resting time (weeks).

Figure 7.16 (a) presents digital photographs of S@Al foil electrode and CSC@separator electrode after 100 cycles. A small amount of active materials exfoliated from S@Al foil electrode. In contrast, the CSC@separator electrode maintained a good appearance, without any obvious exfoliation or changes, indicating that the integrated CSC@separator electrode has good structural stability. Furthermore, the cycled S@Al foil and CSC@separator electrodes were examined by ultraviolet-visible (UV-vis) absorption spectroscopy. The colour of the DOL/DME solutions for the S@Al foil electrodes changed from colourless to yellow with increasing cycle number, while no noticeable colour change can be observed for the CSC@separator electrodes, even after 200 cycles (Figure 7.17).

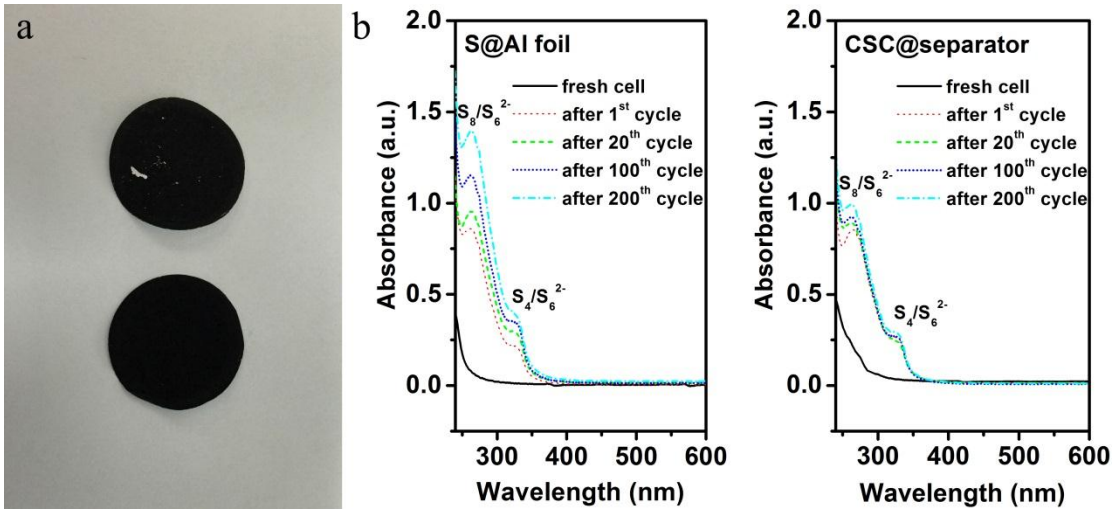

Figure 7.16 (a) Digital photographs of S@Al foil (top) and CSC@separator electrodes (bottom) after 100 cycles. (b) UV-vis absorption spectra of DOL/DME solution with S@Al foil electrode and CSC@separator electrode at various cycle numbers.

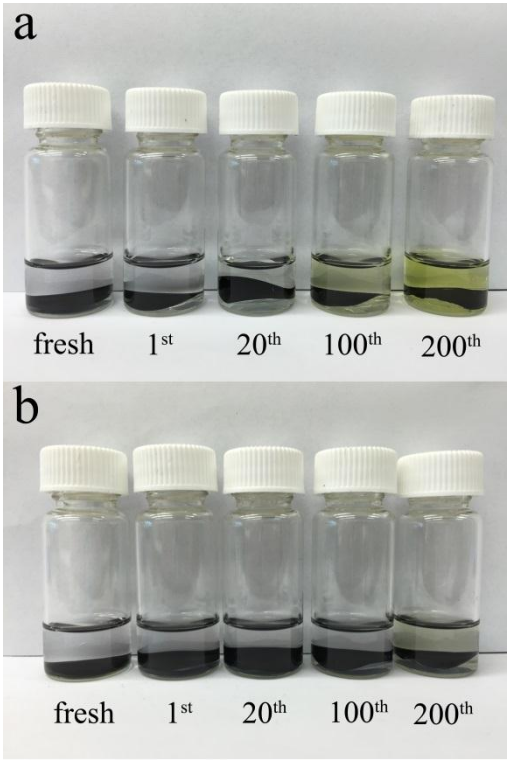

Figure 7.17 Typical colours of the DOL/DME solutions with cycled (a) S@Al foil electrodes and (b) CSC@separator electrodes

The similar intensities of the peaks for the CSC@separator electrodes at different cycles indicate similar content of polysulfides in the electrolyte, confirming a low rate of polysulfide diffusion and effective absorption by the double carbon layers (Figure 7.16 (b)).

The morphology of the cycled S@Al foil electrode and CSC@separator electrodes was studied by SEM (Figure 7.18). After 100 cycles, the surface of the S@Al foil electrode became denser and large particle aggregation can be clearly observed. The elemental mapping and energy-dispersive X-ray (EDX) spectroscopy results revealed that the particle aggregates are rich in sulfur. In contrast, the CSC@separator electrode shows no obvious changes compared to the fresh electrode, and no particle aggregation and only a weak signal of sulfur can be observed, suggesting that the diffusion of polysulfide is controlled within the two carbon layers, which makes a great contribution to the cycling stability.

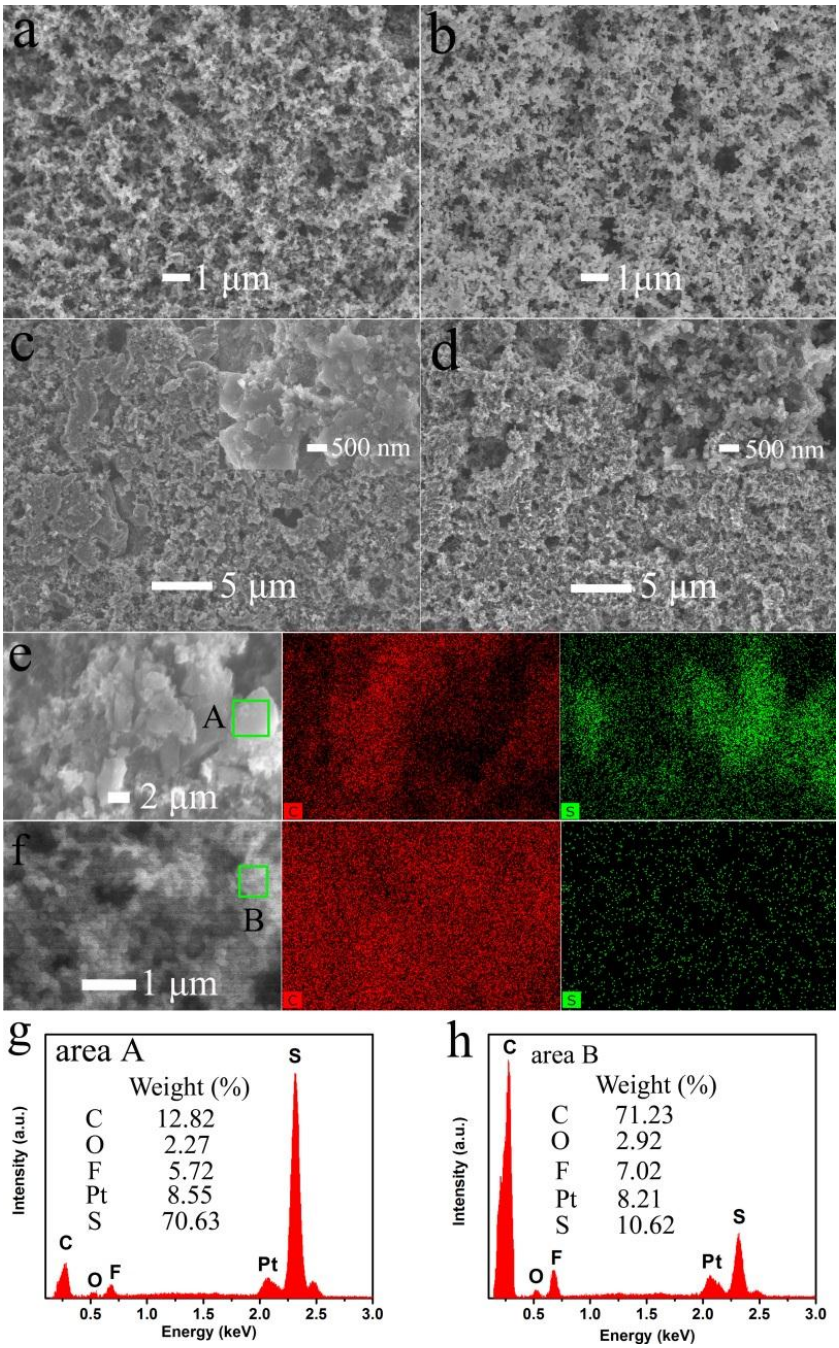

Figure 7.18 SEM images of the S@Al foil electrode (a) before and (c) after 100 cycles, and of the CSC@separator electrode (b) before and (d) after 100 cycles, and corresponding elemental mapping of carbon and sulfur for (e) S@Al foil and (f) CSC@separator electrodes after 100 cycles. EDX spectra for selected areas of cycled (g) S@Al foil electrode and (h) CSC@separator electrode.

To further confirm the effects of the carbon layer towards suppressing the diffusion of the polysulfides, a schematic illustration of polysulfide diffusion in the CSC@separator electrode are shown in Figure 7.19. The sandwich structure of the CSC@separator electrode could well maintained after cycles, which could control the diffusion of polysulfides, buffer the volume changes during cycling, and maintain the integrity of the whole electrode.

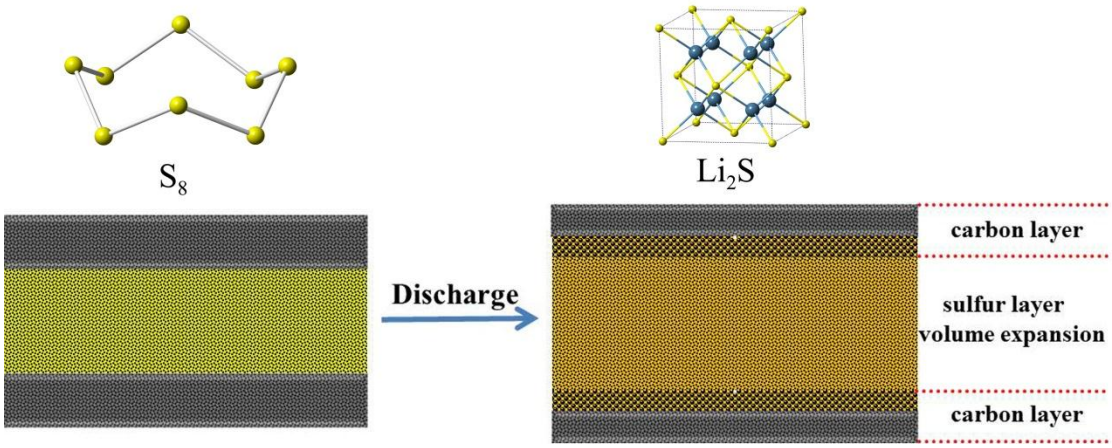

Figure 7.19 Schematic illustration of polysulfide diffusion, with trapping in the carbon layer.

To further understand why the integrated electrode could delivery more stable capacity than the conventional S@Al foil electrode, the cycling performance of a half-covered S@separator electrode was tested (Figure 7.20). Apparently, there is a small amount of Super P in the S@separator electrode, which could easily disperse into the nanopores of the separator and act as a complete physical barrier to prevent polysulfide diffusion to the anode side for a fully covered S@separator electrode. There is still half uncovered area, however, in the half-covered S@separator electrode, resulting in poor cycling performance.

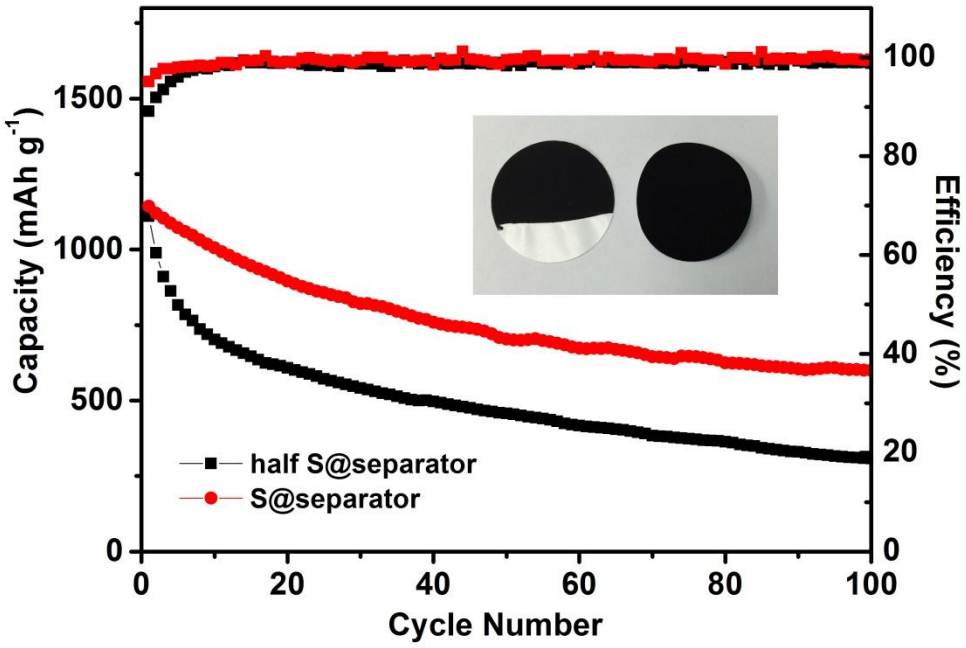

Figure 7.20 Comparison of cycling performance of Li-S cells with S@separator and half S@separator electrodes.

Overall, this unique design for the integrated sandwich electrode has three important characteristics, imparting the CSC@separator electrode with excellent electrochemical performance. First, the double carbon coating layers play the role of current collectors to offer continuous electron transfer pathways from top to bottom, improve the electronic conductivity, and decrease the internal charge transfer resistance, enhancing the sulfur utilization. Second, the double carbon coating layer could tolerate volume expansion without causing the active material to exfoliate from the electrode and thus maintain the integrity of the electrode. As the last but the most important one, the carbon layers could serve as effective barriers to control the diffusion of the polysulfides and keep them within the cathode region, eliminating the

shuttle effect and self-discharge behaviour to a large extent. The shuttle factor for the CSC@separator electrode is 0.067, much lower than that for the S@Al foil electrode (0.42, Table 7.2). Commonly, no matter how sophisticated the nanostructured sulfur cathode is in a conventional Li-S cell, it is inevitable that small amounts of polysulfides will dissolve into the electrolyte and then diffuse across the nanoporous separator, leading to the capacity fading. In our design, however, the dissolved polysulfides must travel through the carbon coating layer before the separator, fully encountering the absorption effect of the carbon layer.

Table 7.2 Calculation of shuttle factor for Li-S cells using the conventional S@Al foil and CSC@separator electrodes.

Electrode	Shuttle Factor
S@Al foil	0.4196
CSC@separator	0.0666

The shuttle factor suggested by Mikhaylik and Akridge1 is defined to reflect the extent of the shuttle effect. The shuttle factor is expressed as:

$$f = k_s \cdot Q_H / I \quad (2)$$

Where k_s is the heterogeneous reaction constant related to polysulfide diffusion and reaction, Q_H is the theoretical charge/discharge capacity of the high plateau, and I is the charge/discharge current. Based on a previous report, the relationship between the Coulombic efficiency and the shuttle factor can be expressed as follows:

$$C_{eff} = \frac{2 + (ln(1+f))/f}{2 - (ln(1-f))/f}$$

7.4 Conclusions

In conclusion, for the first time, we have successfully designed and prepared a unique flexible cathode architecture consisting of a carbon/sulfur/carbon sandwich structure coated directly on a polypropylene separator via the doctor blade method. The CSC@separator cathode delivered a high reversible capacity of 730 mAh g^{-1} over 500 cycles, with capacity decay as small as 0.058% per cycle and a low self-discharge constant of 0.0293 per week. The improved performance is attributed to the enhanced electronic conductivity, toleration of volume expansion, and control of the polysulfide diffusion of the unique integrated sandwich structured electrode. Together with the simple and scalable nature of its fabrication, our integrated sandwich structured electrode is highly promising for practical application in Li-S batteries.

7.5 Reference

[1] S. E. Chen, S. S. Choi, J. S. Han, Y. S. Choi, B. H. Jung, H. S. Lim, Journal of the Electrochemical Society, 151 (2004) A2067-A2073.

[2] X. L. Ji, K. T. Lee, L. F. Nazar, Nature Materials, 8 (2009) 500-506.

[3] P. G. Bruce, S. A. Freunberger, L. J. Hardwick, J. M. Tarascon, Nature Materials, 11 (2012) 19-29.

[4] Y. Yang, G. Y. Zheng, S. Misra, J. Nelson, M. F. Toney, Y. Cui, Journal of the American Chemical Society, 134 (2012) 15387-15394.

[5] Z. Li, J. T. Zhang, X. W. Lou, Angewandte Chemie International Edition, 54 (2015) 12886-12890.

[6] N. Jayaprakash, J. Shen, S. S. Moganty, A. Corona, L. A. Archer, Angewandte Chemie International Edition, 50 (2011) 5904-5908.

[7] H. L. Wang, Y. Yang, Y. Y. Liang, J. T. Robinson, Y. G. Li, A. Jackson, Y. Cui, H. J. Dai, Nano Letters, 11(2011) 2644-2647.

[8] C. F. Zhang, H. B. Wu, C. Yuan, Z. P. Guo, X. W. Lou, Angewandte Chemie International Edition, 51 (2012) 9592-9595.

[9] Q. Pang, J. T. Tang, H. Huang, X. Liang, C. Hart, K.C. Tam, L.F. Nazar, Advanced Materials, 27 (2015) 6021-6028.

[10] L. N. Wang, Y. Zhao, M. L. Thomas, H. Byon, Advanced Functional Materials, 24 (2014) 2248–2252.

[11] J. X. Song, M. L. Gordin, T. Xu, S. R. Chen, Z. X. Yu, H. Sohn, J. Lu, Y. Ren, Y. H. Duan, D. H. Wang, Angewandte Chemie International Edition, 127 (2015) 4399-4403.

[12] Q. Sun, X. Fang, W. Weng, J. Deng, P. N. Chen, J. Ren, G. Z. Guan, M, Wang, H. S. Peng, Angewandte Chemie International Edition, 54 (2015) 10539-10544.

[13] M. Q. Zhao, Q. Zhang, J. Q. Huang, G. L. Tian, J. Q. Nie, F. Wei, Nature Communications, 5 (2014) 3410.

[14] J. P. Rong, M. Y. Ge, X. Fang, C. W. Zhou, Nano Letters, 14 (2014) 473–479.

[15] J. L. Wang, Y. S. He, J. Yang, Advanced Materials, 27 (2015) 569-575.

[16] L. F. Xiao, Y. L. Cao, J. Xiao, B. Schwenzer, M. H. Engelhard, L. V. Saraf, Z. M. Nie, G. J. Exarhos, J. Liu, Advanced Materials, 24 (2012) 1176-1181.

[17] K. Park, J. H. Cho, J. H. Jang, B. C. Yu, A. T. De La Hoz, K. M. Miller, C. J. Ellison, J. B. Goodenough, Energy & Environmental Science, 8 (2015) 2389-2395.

[18] X. Liang, A. Garsuch, L. F. Nazar, Angewandte Chemie International Edition, 127 (2015) 3979-3983.

[19] Z. W. Seh, W. Y. Li, J. J. Cha, G. Y. Zheng, Y. Yang, M. T. McDowell, P. C. Hsu, Y. Cui, Nature Communications, 4 (2013) 1331.

[20] Q. Pang, D. Kundu, M. Cuisinier, L. F. Nazar, Nature Communications, 5 (2014) 4759.

[21] Z. Liang, G. Y. Zheng, W. Y. Li, Z. W. Seh, H. B. Yao, K. Yan, D. S. Kong, Y. Cui, ACS Nano, 8 (2014) 5249-5256.

[22] K. E. Hendrickson, L. Ma, G. Cohn, Y. Y. Lu, L. A. Archer, Advanced Science, 2 (2015) 1500068.

[23] S. H. Chung, A. Manthiram, Nature Communications, 3 (2012) 1166.

[24] S. Y. Sheng, A. Manthiram, Chemical Communications. 48 (2012) 8817-8819.

[25] J. Q. Huang, B. A. Zhang, Z. L. Xu, S. Abouali, M. A. Garakani, J. Q. Huang, J. K. Kim, Journal of Power Sources, 285 (2015) 43-50.

[26] X. F. Wang, Z. X. Wang, L. Q. Chen, Journal of Power Sources. 242 (2013) 65-69.

[27] S. H. Chung, A. Manthiram, Chemical Communications, 50 (2014) 4184-4187.

[28] J. Q. Huang, Q. Zhang, H. J. Peng, X. Y. Liu, W. Z. Qian, F. Wei, Energy & Environmental Science, 7 (2014) 347-353.

[29] J. Balach, T. Jaumann, M. Klose, S. Oswald, J. Eckert, L. Giebeler, Advanced Functional Materials, 25 (2015) 5285-5291.

[30] S. H. Chung, A. Manthiram, Advanced Materials, 26 (2014) 7352-7357.

[31] H. B. Yao, K. Yan, W. Y. Li, G. Y. Zheng, D. S. Kong, Z. W. Seh, V. K. Narasimhan, Z. Liang, Y. Cui, Energy & Environmental Science, 7 (2014) 3381-3390.

[32] J. Q. Huang, T. Z. Zhuang, Q. Zhang, H. J. Peng, C. M. Chen, F. Wei, ACS Nano, 9 (2015) 3002-3011.

8 A NOVEL TYPE OF ONE-DIMENSIONAL ORGANIC SELENIUM-CONTAINING FIBERS WITH SUPERIOR PERFORMANCE FOR LITHIUM-SELENIUM AND SODIUM-SELENIUM BATTERIES

8.1 Introduction

The rechargeable lithium-sulfur (Li-S) battery has attracted enormous attention in the past several years due to its high energy density and ultra-high theoretical specific capacity (2567 Wh kg^{-1} and 1675 mAh g^{-1}, respectively) [1-3]. Selenium, as a congener of sulfur, possesses similar chemical behavior and could react with lithium to form selenides. The theoretical gravimetric capacity of selenium electrode (675 mAh g^{-1}) is lower than that of sulfur, however, the theoretical volumetric capacity of selenium (3253 mAh cm^{-3}) is comparable to that of sulfur (3467 mAh cm^{-3}) [4-7]. More importantly, the electrical conductivity of selenium is much higher than that of sulfur [5]. These features of Se make it an attractive alternative candidate for cathode material in lithium-ion batteries as well as sodium-ion batteries. Due to the similarity to sulfur, however, the selenium cathodes also suffer from the dissolution issue of high-order polyselenides, leading to the low utilization of selenium, low coulombic efficiency of the selenium cathode, and fast capacity fading.

At present, study on selenium cathode is at a very early stage. Several attempts have been applied to enhance the electrochemical properties of selenium-based cathodes. Amine's group [5] firstly conducted work on Se/CNT composite as a cathode material, and the Se/CNT composite electrode could deliver a capacity of 300 mAh g^{-1} after 100 cycles for rechargeable lithium battery. Guo et al. [6] prepared Se/CMK-3

composite with a reversible capacity of 600 mAh g^{-1} after 50 cycles by using a simple thermal-treatment method. Wang et al. [7] synthesized nano-Se_8-carbon composite containing 30% selenium and the obtained Se_8/C composite electrodes demonstrated excellent electrochemical performance and could remain capacity of 480 mAh g^{-1} in Li-Se batteries for 1000 cycles, and 340 mAh g^{-1} in Na-Se batteries for 380 cycles. To date, all the research on the selenium cathode for energy storage has been focused on "physical" methods to confine selenium in a porous matrix to prevent soluble polyselenides from dissolving in the organic electrolyte [5-10]. It is clear that trapping selenium in the porous matrix by such a physical method is an effective approach to solve the dissolution problem. On the other hand, using a "chemical" method involving functional groups and the unique chain structure of the polymer maybe a more efficient strategy to confine the selenium compared to the physical method because it can yield excellent stability and activity. Herein, we report a novel type of organic selenium-containing fiber material, in which the Se is trapped in energy-storing selenium side chains in an organic carbon skeleton matrix. This novel fibrous material was prepared by heating polyacrylonitrile-Se (PAN-Se) fibers via the electrospinning technique under vacuum, in which trigonal Se is converted into chain-like Sex molecular groups that are bonded to the carbonized polymer during the calcination process. The conductive carbon skeleton can effectively confine the selenium by forming a stable structure connected to the selenium side chains. Given the high electrochemical activity of the selenium side chains linked to the organic carbon and the strong interaction between them, this novel selenium cathode shows

excellent stability during lengthy electrochemical cycling for both lithium-ion and sodium-ion batteries.

8.2 Experimental

8.2.1 Preparation of carbonized polyacrylonitrile/selenium (CPAN/Se) fibers

The carbonized polyacrylonitrile/selenium composite (CPAN/Se) fibers were synthesized through the electrospinning technique. In a typical synthetic procedure, 1 g PAN was dissolved in 10 g dimethylformamide (DMF) and stirred for 24 h at 70^{o}C to yield a clear solution. Next, 0.8 g selenium powder was added into the solution. Finally, a homogeneous suspension was obtained after 4 h strong mechanical stirring. During electrospinning process, the solution was loaded into syringe with a metallic needle (inner diameter 0.5 mm) under applied voltage of 16.2 kV. The distance from needle tip to stainless steel mesh collector was about 11 cm. Then, the collected primary film was dried at 100 ^{o}C for 24 h. The obtained products were heat-treated at 600 ^{o}C for 5 h in vacuum with a heating rate of 5 ^{o}C min^{-1} to achieve the CPAN/Se composite. Control sample, carbonized PAN/Se powder (CPAN/Se powder), was prepared by the same process but without electrospinning technique. The PAN powders were mixed with selenium powders (5:4 by weight) and then heated at 600 ^{o}C for 5 h in vacuum to obtain CPAN/Se powder.

8.2.2 Materials Characterization

The crystal structure of the samples were examined with X-ray diffraction diffractometer (XRD, MMA GBC, Australia) with Cu Kα radiation. Raman spectroscopy on an instrument (JOBIN YVON HR800) equipped with a 632.8 nm

diode laser and Fourier-transform infrared spectroscopy (FT-IR) were carried out to characterize the chemical bonds in each sample. The selenium content of composite was measured by Thermogravimetric analysis/differential scanning calorimetry (TGA/DSC) type instrument (METTLER TOLEDO, Switzerland) at a heating rate of 10 ^{o}C min^{-1} from room temperature to 750 ^{o}C under argon atmosphere. X-ray photoelectron spectroscopy (XPS) analysis was conducted on a VG Scientific ESCALAB 2201XL system with aluminum Kα X-ray radiation. JEOL JSM-7500FA Field-emission scanning electron microscopy (FESEM) and JEOL 2011 transmission electron microscopy (TEM) were employed to investigate the morphologies of the samples.

8.2.3 Electrochemical measurement

The CPAN/Se fibers and CPAN/Se powders (75% by weight) were mixed with super-P (15%) and PCDF (10%) in NMP solution to form the slurry for the electrode preparation, respectively. After that, the working electrodes were prepared by coating the slurry onto aluminium foil current collector then dried at 50 ^{o}C for 24 h. Coin-type (CR2032) cells were assembled in an argon-filled glove box, with 1 M $LiPF_6$ in a mixture of ethylene carbonate/diethylcarbonate (EC/DEC, 1:1, v/v) as the electrolyte for Li-Se batteries and 1 M $NaClO_4$ in a mixture of ethylene carbonate/diethyl carbonate (EC/DEC, 1:1, v/v) as the electrolyte for Na-Se batteries. Cells with CPAN electrodes were also prepared using the same procedure. The coin cells were galvanostatically charged-discharged from 0.8 to 3.0 V for Li-Se batteries and from

0.5 to 2.5 V for Na-Se batteries using a cell test instrument (CT2001A, LAND, China).

8.3 Results and discussions

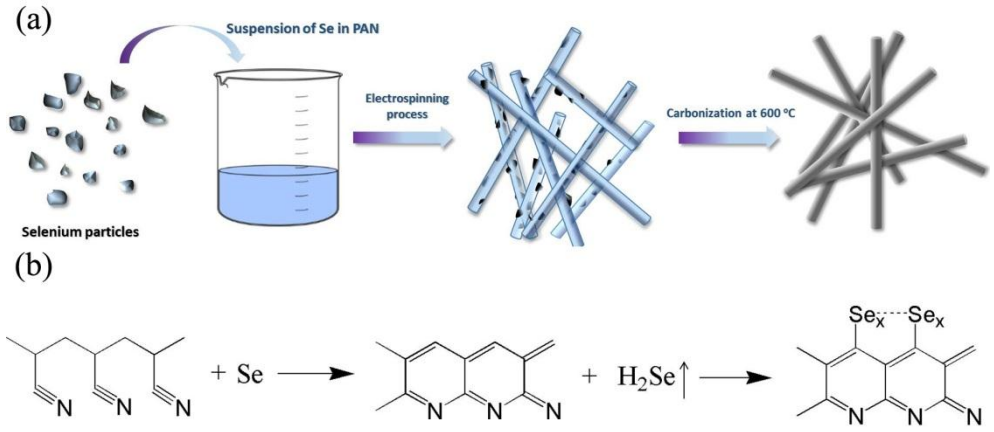

Figure 8.1 (a) A schematic illustration of the experimental procedure; (b) the ideal structure of CPAN/Se and its reaction process.

The experimental procedures are illustrated in Figure 8.1. First of all, selenium powders were added into the PAN solution to form a stable suspension due to the suitable viscosity of the PAN solution, although selenium powders are insoluble in DMF (Figure 8.1 (a)). Next, one-dimensional (1D) PAN-Se fibers were prepared by the electrospinning technique. Finally, the as-spun PAN-Se fibers were heated at 600 ^{o}C for 5 h to obtain CPAN/Se composite fibers. During the thermal treatment, the reactions of PAN with selenium are summarized as follows (Figure 8.1 (b)): When the PAN-Se fibers are heated, Se plays the role of a reducer in facilitating the dehydrogenation and cyclization of PAN, resulting in a conductive main chain with generation of H_2Se as a by-product. Meanwhile, the highly polar -CN functional groups can be cyclized in form of a stable and conductive heterocyclic compound.

Subsequently, at relatively high temperature, elemental selenium is subject to being cleaved into selenium free radicals and intercalated into the heterocyclic compound, which then acts as energy-storing side chains with various lengths, or to forming covalent bonds with the carbon atoms in the PAN-derived carbon matrix. A similar reaction has been reported in sulfur-based composites [11-13]. This novel type of selenium in the CPAN matrix acts as an important role in the electrochemical properties of the CPAN/Se electrodes for both Li-Se and Na-Se cells.

Figure 8.2 presents SEM images of the as-spun PAN-Se fibers and CPAN/Se fibers. The as-spun PAN-Se sample has good fibrous morphology with smooth surfaces, except for a few large particles located on the surface, indicating that most of the selenium powders were wrapped inside of the PAN fibers during the electrospinning process. Figure 8.2 (a) inset is an SEM image of the selenium powders, in which the particle size was mainly less than 200 nm. The 1D fibrous morphology was preserved during the carbonization step, and no particles were left on the surfaces of the fibers, suggesting that a complete reaction between Se and PAN had occurred. The element mapping indicates that all the elements (carbon, nitrogen, and selenium) are uniformly distributed over the whole fiber.

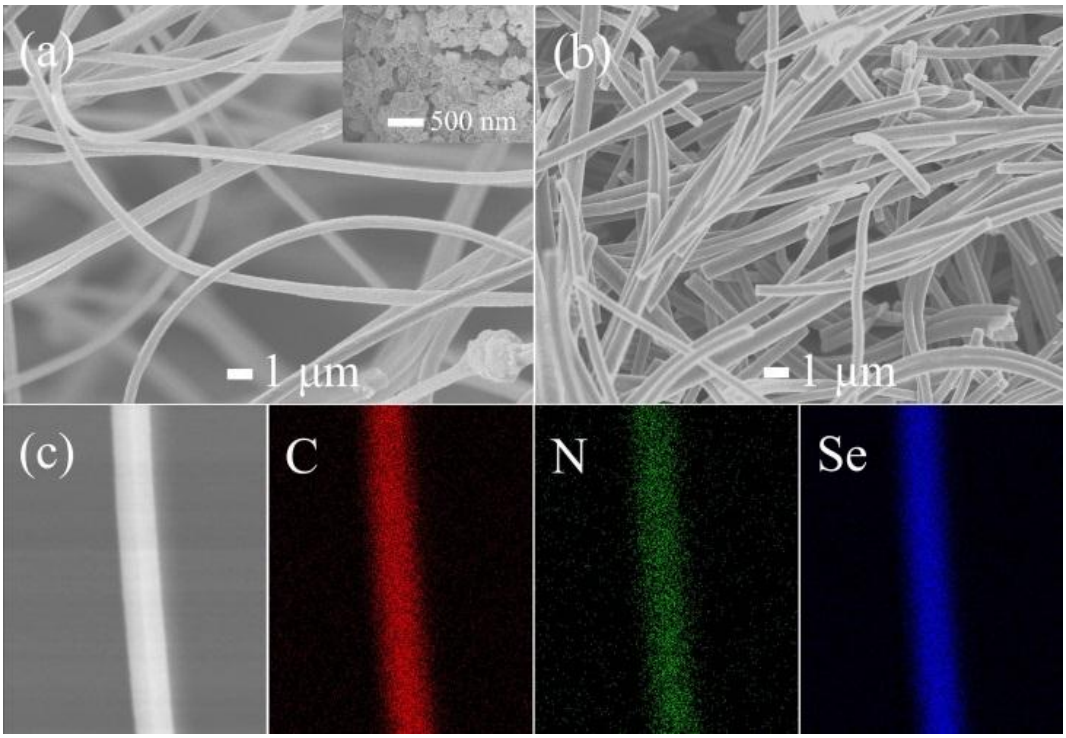

Figure 8.2 SEM images of (a) as-spun PAN-Se fibers, with the inset showing an image of the selenium powders, (b) CPAN/Se fibers, and (c) a single PAN/Se fiber and the corresponding elemental mapping images of carbon, nitrogen, and selenium.

Transmission electron microscopy (TEM) was employed to further investigate the microstructure of the PAN-Se and CPAN/Se fibers in Figure 8.3. Before calcination, it is clear that the selenium powders are well distributed throughout the whole fiber (Figure 8.3 (a)), and high resolution TEM (HRTEM) image (Figure 8.3 (b)) and selected area electron diffraction (SAED) pattern (Figure 8.3 (c)) indicate that the selenium powders are present in the form of the crystal structure in the fiber. The surface of the fiber becomes much smoother, however, and no obvious particles can be seen on the CPAN/Se fibers (Figure 8.3 (d)) after the carbonization process. From HRTEM image (Figure 8.3 (e)) and the SAED pattern (Figure 8.3 (f)) of the CPAN/Se composite, it can be concluded that the CPAN/Se composite has an

amorphous structure, suggesting that selenium could react with PAN during the carbonization process and exist in form of amorphous structure in the CPAN matrix.

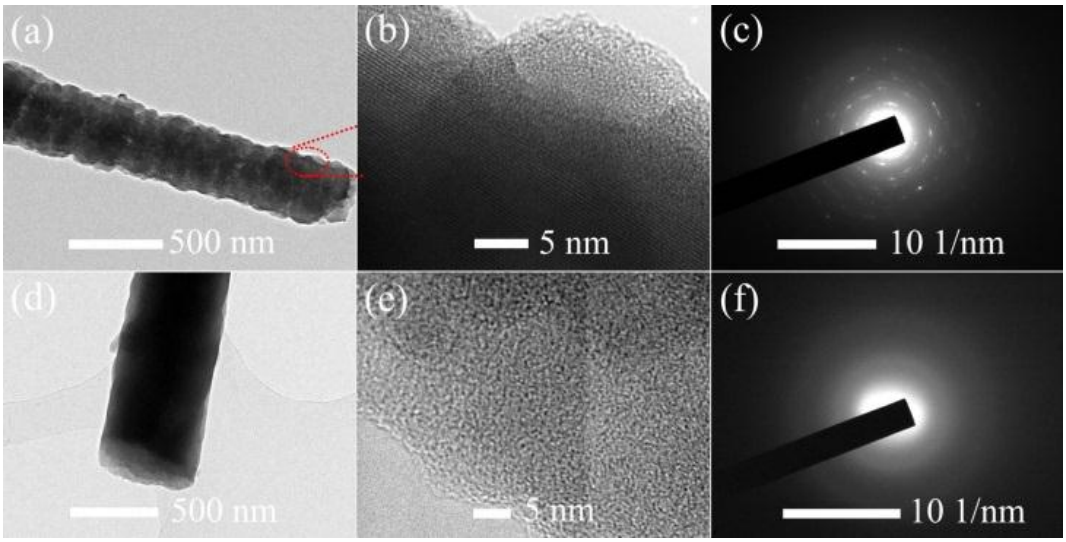

Figure 8.3 TEM image (a), HRTEM image (b), and SAED pattern (c) for PAN-Se fiber; TEM image (d), HRTEM image (e), and SAED pattern (f) of CPAN/Se fiber.

Figure 8.4 (a) shows the XRD patterns of the elemental selenium, CPAN, and CPAN/Se. The pristine Se possesses trigonal structure, while the CPAN/Se has amorphous structure. Although there is a substantial amount of selenium (36%, in Figure 8.5 and Figure 8.6) in the CPAN/Se composite, the peaks of elemental selenium could not be observed, suggesting that the embedded selenium in the composite exists in the form of small molecules rather than Se_8 and thus loses its characteristic of trigonal structure.

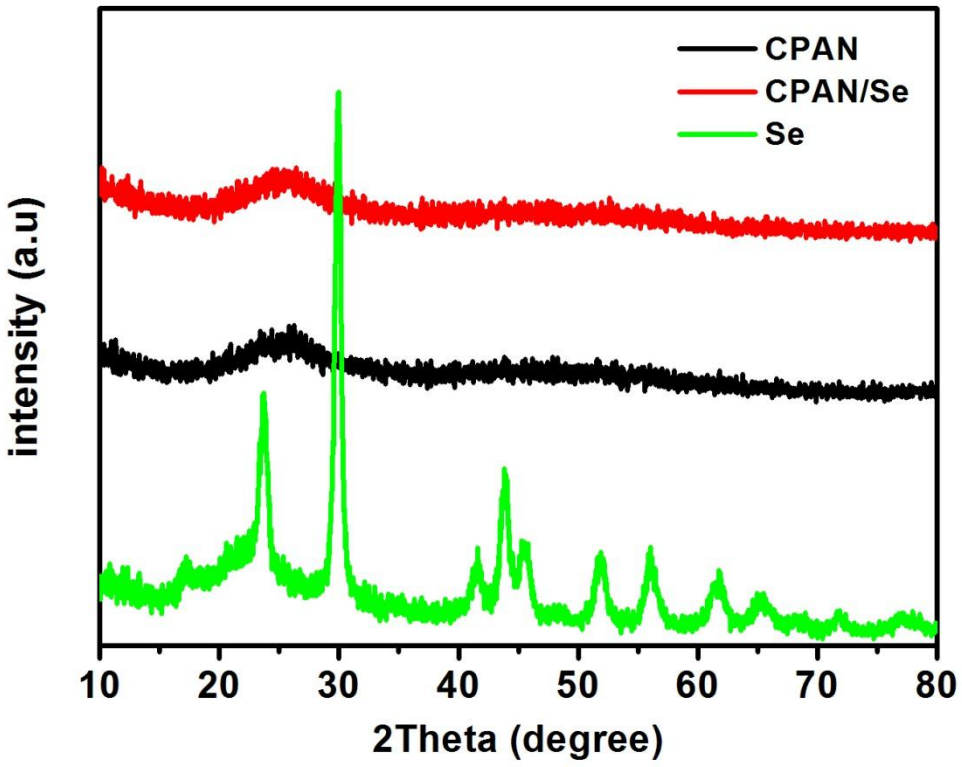

Figure 8.4 XRD patterns of Se, CPAN, and CPAN/Se fibers.

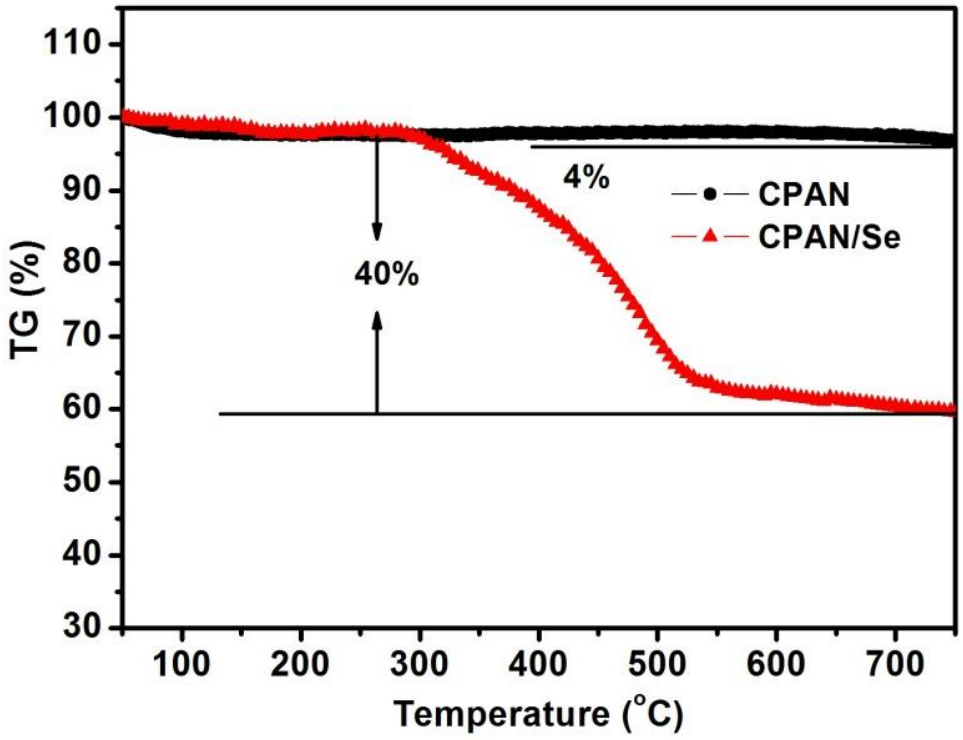

Figure 8.5 TGA curves of CPAN and CPAN/Se fiber under argon atmosphere.

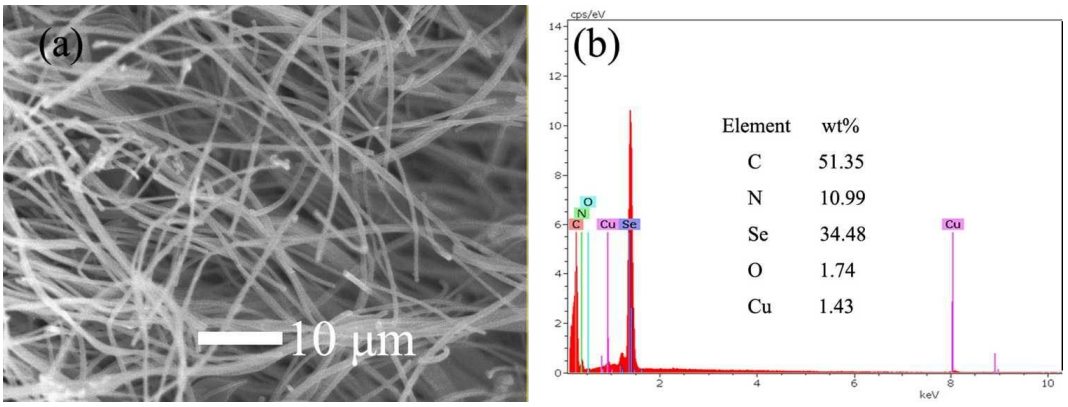

Figure 8.6 (a) SEM image of CPAN/Se fibers, (b) elemental information obtained by EDX characterization for the entire area (62 × 47 μm^2) shown in (a). The detected Cu on the CPAN/Se fiber sample is attributed to the copper substrate.

Figure 8.7 presents the Se 3d XPS spectra for pristine Se and CPAN/Se. In the pristine Se, the Se $3d_{5/2}$ and $3d_{3/2}$ peaks centered at 55.8 and 56.7 eV, which could be assigned to metallic selenium. The Se $3d_{5/2}$ and $3d_{3/2}$ peaks move towards higher binding energy in the CPAN/Se, however, which means that the Se has formed bonds with other atoms in the composite to yield selenium-containing heterocyclic compounds. There is evidence in the literature that the 3d peak could change when Se is combined with other atoms [4,14,15].

The existence of the C-Se bond is the key to judge whether Se is incorporated into the PAN-based polymer matrix. Therefore, Raman and Fourier-transform infrared (FT-IR) spectroscopy were performed to further examine the chemical bonds in CPAN/Se. Figure 8.8 displays the FT-IR spectra of the CPAN and CPAN/Se. Both the CPAN and the CPAN/Se exhibit peaks at 1590, 1295, and 833 cm^{-1} corresponding to the C=C bond, C=N bond, and C-N bond, respectively [16-19], suggesting the formation of a heterocyclic compound in the carbonization process. The new peak at 523 cm^{-1}

corresponds to torsion of rings in which a C-Se bond is contained [20], and the peak located at 438 cm^{-1} could be also attributed to the C-Se bending vibration [19], indicating the formation of C-Se bonds after the dehydrogenation and cyclization process. In the Raman spectroscopy (Figure 8.9), the elemental selenium shows three peaks located at 138, 231, and 458 cm^{-1}, respectively. CPAN/Se exhibits distinctive peaks at 198 and 288 cm^{-1}, however, indicating that the atomic configuration of CPAN/Se has changed markedly after the reaction with selenium. The peaks centered at 198 and 288 cm^{-1} can be attributed to the C-Se stretching vibration and the C-Se-Se group vibration [19].

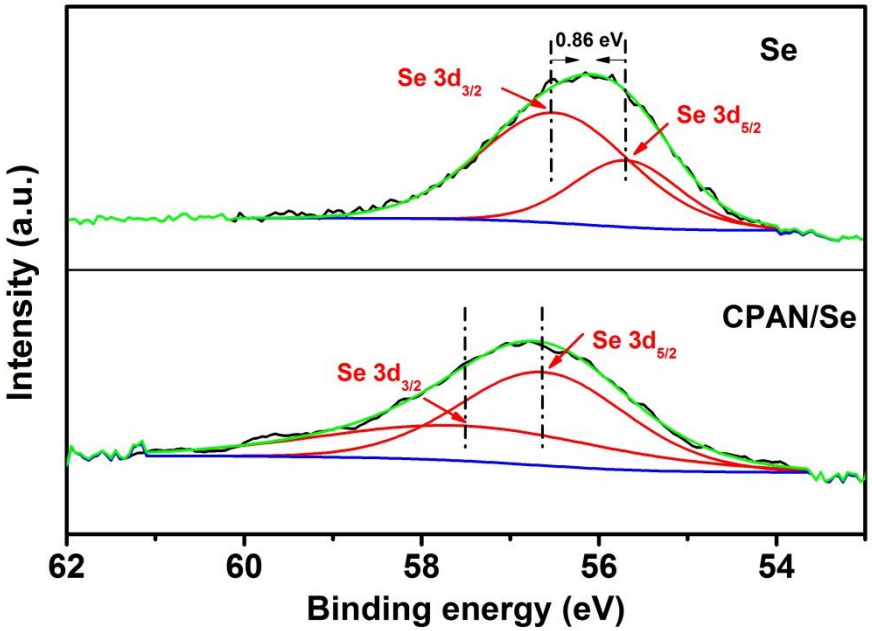

Figure 8.7 XPS spectra of Se and CPAN/Se fibers for Se 3d

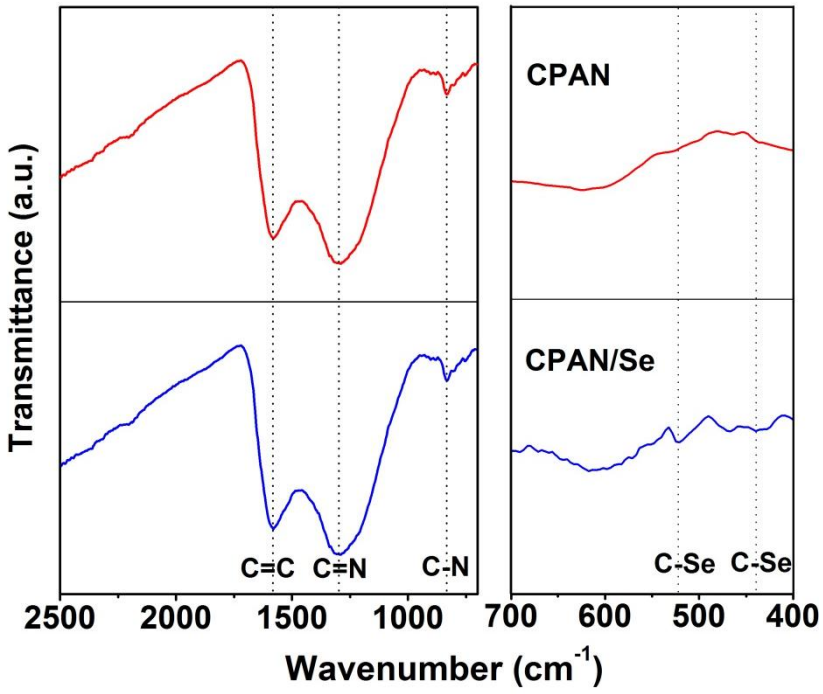

Figure 8.8 FT-IR spectra of CPAN, and CPAN/Se fibers

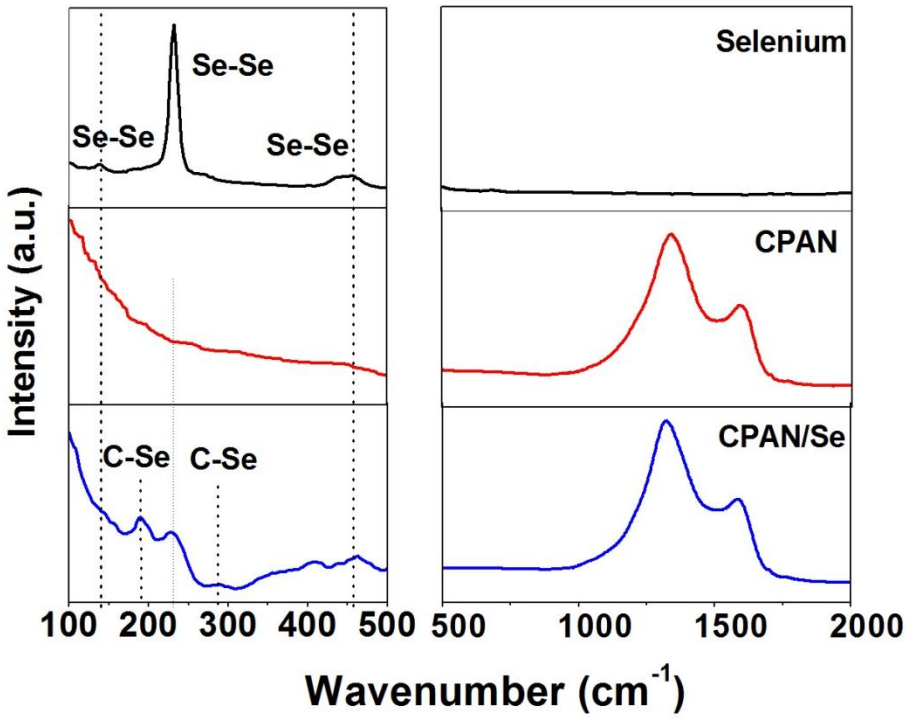

Figure 8.9 Raman spectra of Se, CPAN, and CPAN/Se fibers

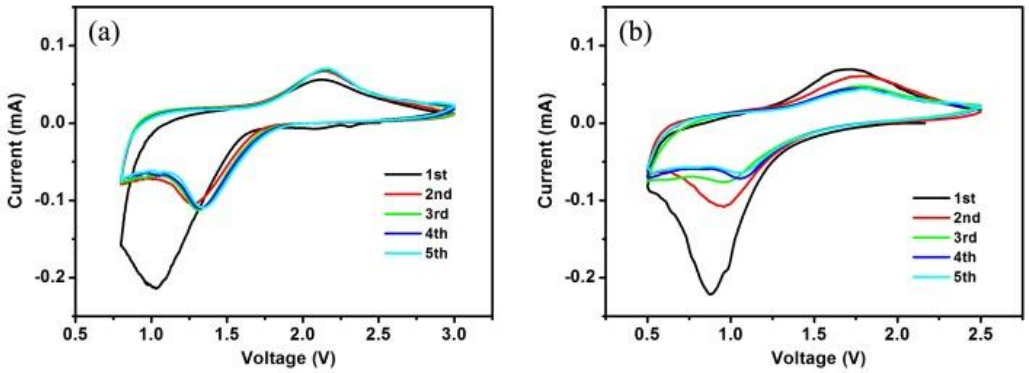

Figure 8.10 Cyclic voltammograms of the CPAN/Se fiber electrodes in (a) Li-Se and (b) Na-Se batteries at a scan rate of 0.1 mV/s.

Cyclic voltammetry (CV) tests for CPAN/Se batteries were performed in the voltage window from 0.8 V to 3 V vs. Li^+/Li, and 0.5 V to 2.5 V vs. Na^+/Na, respectively. Typical CV of the CPAN/Se electrodes in Li-Se and Na-Se cells are displayed in Figure 8.10. There is only one pair of reversible redox peaks for Li-Se batteries in the CV curves, suggesting that the CPAN/Se electrode experiences a single phase transition reaction from Sex chain to insoluble Li_2Se without formation of soluble intermediate phase Li_2Se_x ($x \geq 4$) in carbonate electrolyte, which is in agreement with previous reports [6,7]. During the first scan, the curve shows a cathodic peak at 1.0 V and an anodic peak at 2.2 V for the Li-Se batteries. After the first scan, the cathodic peak shifts towards the positive direction, while the anodic peak remains at 2.2 V. The interaction between organic selenium and the CPAN matrix during the first lithiation may lead to more potential peak in the first cycle. It is believed that the complex bond formed between selenium and the heterocyclic compound will affect the reaction of selenium and lithium, which needs additional energy to dissociate selenium from the complex bond, leading to a more negative potential [12]. The CPAN/Se cathode in

Na-Se batteries exhibits similar phenomenon to that in Li-Se batteries, as well as having lower redox potentials.

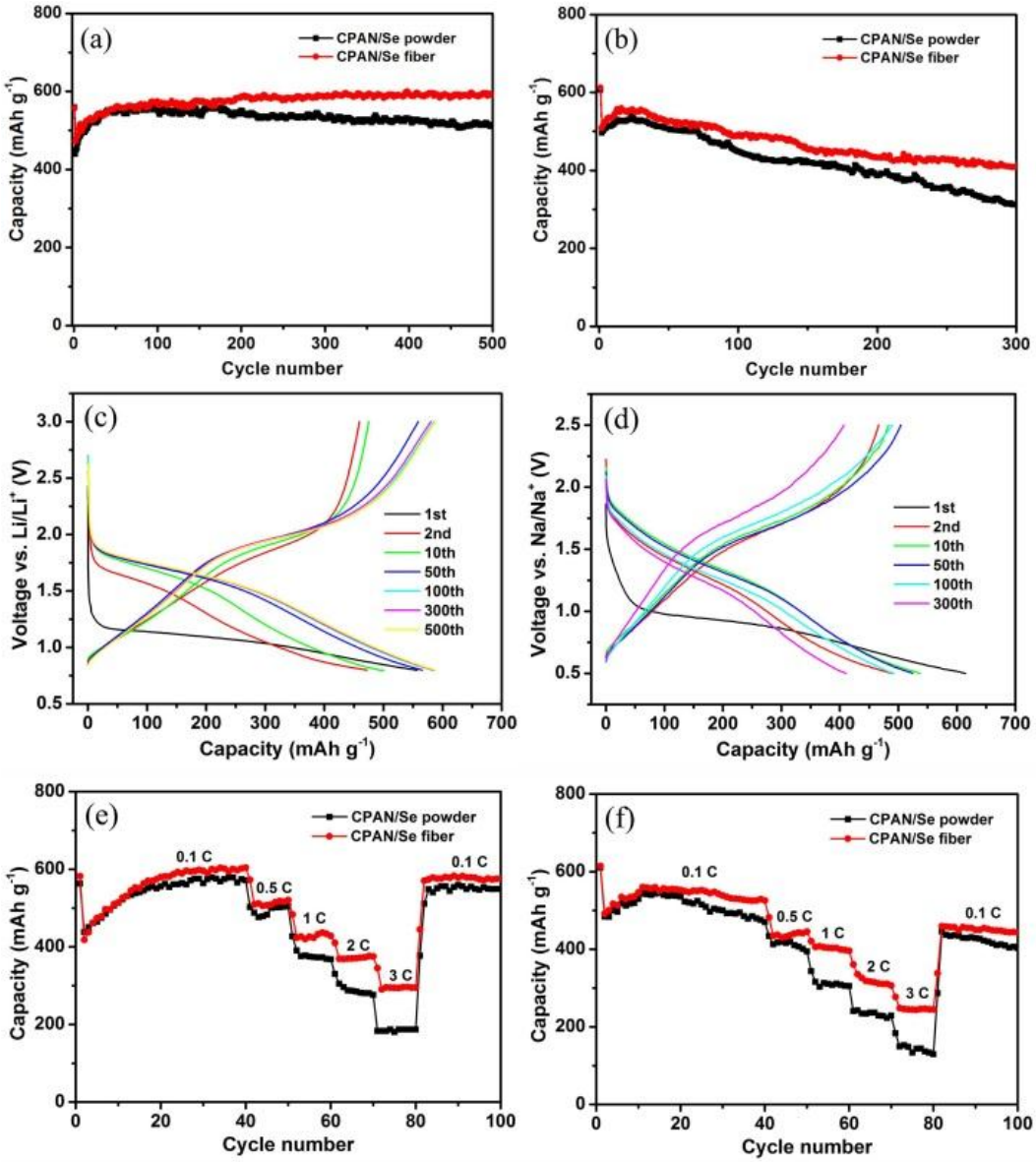

Figure 8.11 Cycling performance of CPAN/Se fiber and powder electrodes at 0.3 C for (a) Li-Se and (b) Na-Se batteries; discharge/charge voltage profiles of CPAN/Se fiber electrode at selected cycles for (c) Li-Se and (d) Na-Se batteries; rate capabilities of CPAN/Se fiber and powder electrodes for (e) Li-Se and (f) Na-Se batteries.

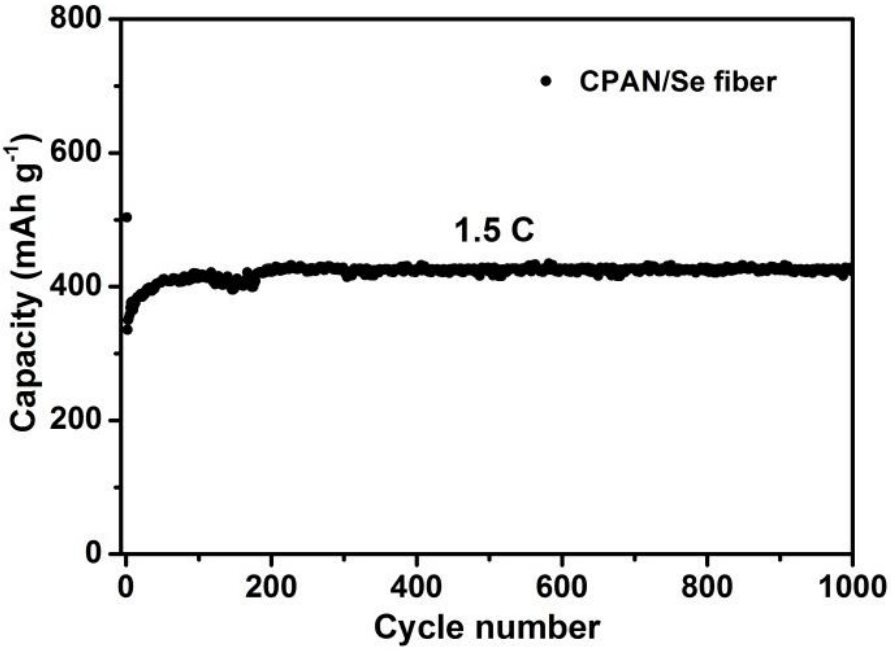

Figure 8.12 Cycling performance of CPAN/Se fiber electrode at current density of 1.5 C (1000 mA g^{-1}) for Li-Se batteries.

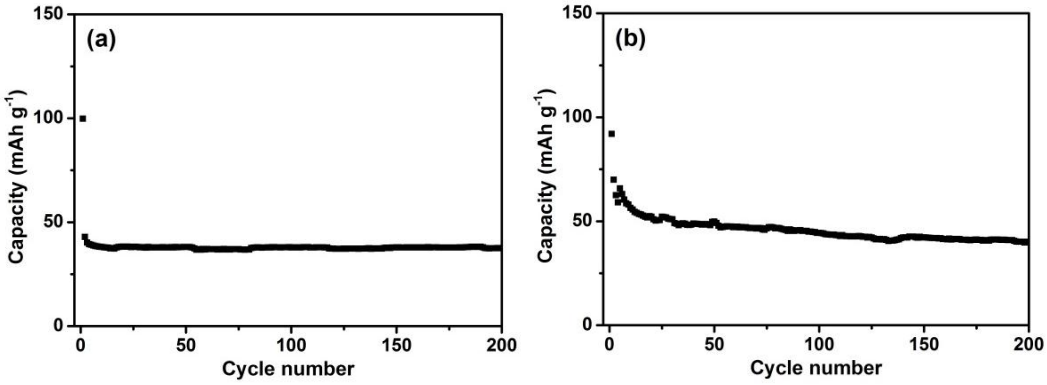

Figure 8.13 Cycling performance of pristine Se electrodes for Li-Se and Na-Se batteries tested at 200 mA g^{-1}.

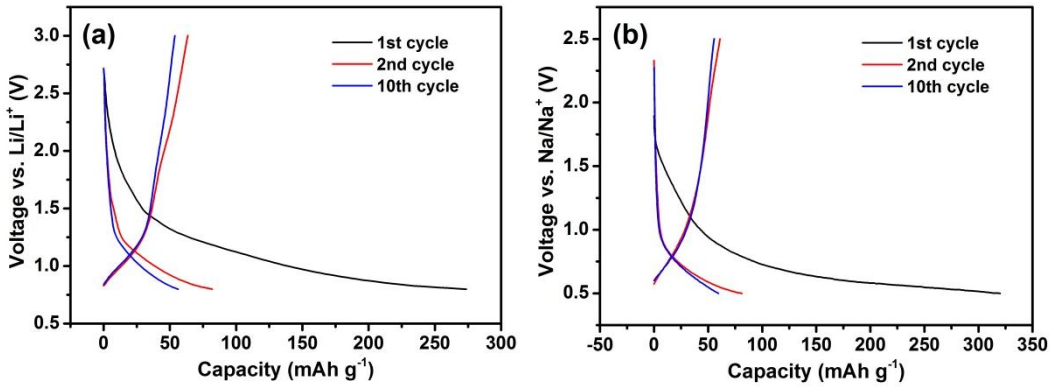

Figure 8.14 Discharge/charge voltage profiles of CPAN, carbon black and PVDF composite (in the weight ratio of 75:15:10) for lithium-ion and sodium-ion batteries tested at 200 mA g^{-1}.

Figure 8.11 (a) and (b) displays the cycling performance of the CPAN/Se fiber and powder cathodes in Li-Se and Na-Se batteries at 0.3 C. Excellent cycling stability in both Li-Se and Na-Se batteries can be obtained. Compared to CPAN/Se powder electrode, the CPAN/Se fiber electrode could deliver a capacity of nearly 600 mAh g^{-1} without any capacity loss after 500 cycles in Li-Se batteries. Even at the rate of 1.5 C, the CPAN/Se fiber electrodes can still maintain more than 400 mAh g^{-1} for 1000 cycles (Figure 8.12), indicating a superior cycling performance compared to that of pristine Se electrodes for Li-Se and Na-Se batteries (Figure 8.13). Such superior capacity of CPAN/Se is a combined outcome from its unique chemical structure. The carbon-based skeleton matrix supports high electrical conductivity, and the PAN-derived carbon-based matrix can confine the selenium during the charge and discharge processes by forming stable energy-storing side chains where selenium free radicals are intercalated into the heterocyclic compound. Furthermore, the presence of nitrogen atoms in the heterocyclic compound linked to selenium side chains could

enhance the electronic conductivity [21,22], which additionally contributes to the exceptional electrochemical performance. Most of all, the interaction between selenium and conductive heterocyclic compound greatly improves the cycling stability of the CPAN/Se electrodes in the low-cost carbonate-based electrolyte and provides a new strategy to develop Se-based cathodes for renewable energy storage.

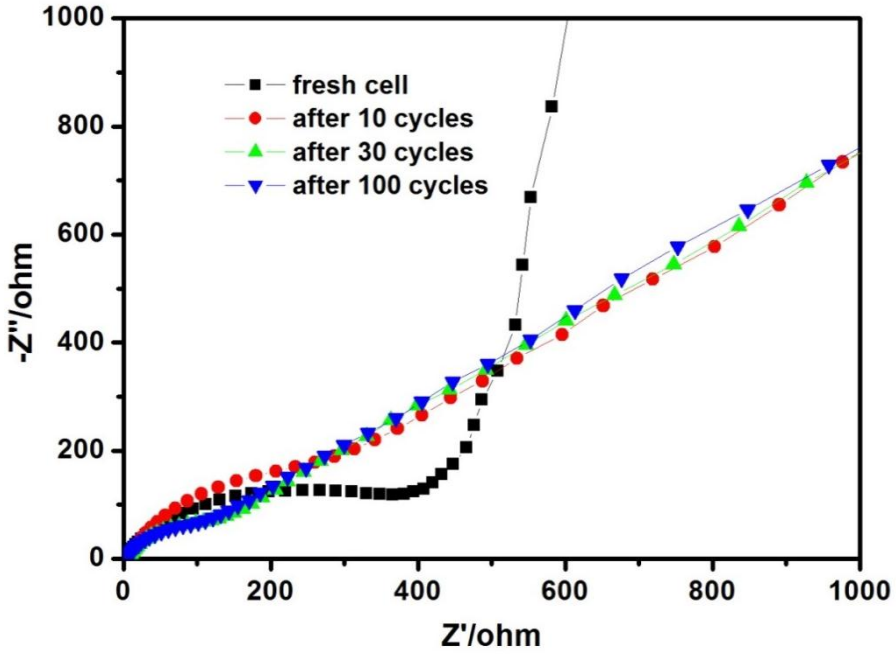

Figure 8.15 EIS spectra of the CPAN/Se fiber cell before test and after cycles.

It is worth noting that the CPAN/Se electrodes for Li-Se batteries deliver an initial discharge capacity of 560 mAh g^{-1}, however, the discharge capacity drops to 460 mAh g^{-1} in the second cycle before increasing to 600 mAh g^{-1} in subsequent cycles. This interesting phenomenon is different from previous result [5-8]. Therefore, the electrochemical performance of CPAN electrode (Figure 8.14) was tested to investigate the higher initial discharge capacity. The CPAN electrode displayed an irreversible capacity of nearly 300 mAh g^{-1} in the first discharge. A long potential

plateau between 1.1 V and 0.8 V is initially present in the CPAN electrode, but it disappears in the second cycle, which is in agreement with the lower plateau of CPAN/Se fiber electrode for the first discharge in Figure 8.11 (c). This can explain its higher initial discharge capacity. In addition, the increase of capacity between the 3rd and the 30th cycle demonstrates a possible activation process in the electrode materials. Accordingly, the increase of the capacity was accompanied by the reduced electrode impedance (Figure 8.15). The fresh CPAN/Se cell shows a large charge transfer resistance. The reason is that the high degree of carbonization at higher temperature causes the active selenium to be deeply enveloped within the amorphous carbon skeleton. Therefore, lithium can only access to the surface of partial active selenium. The whole active selenium could work normally again only after the activation process with longer cycles, resulting in reduced charge transfer resistance in subsequent cycles. As a result, the discharge capacity is improved between the 3rd and the 30th cycles and the reduced impedance in the second cycle shifts the lithiation potential to a higher value as demonstrated in the CV curves in Figure 8.10. For the sodium batteries, the CPAN/Se also demonstrates good cycling performance. In this study, the CPAN/Se shows higher initial discharge capacity and a similar trend in regards to capacity to that in the Li-Se batteries, retaining 410 mAh g^{-1} after 300 cycles. Commonly, electrodes in sodium-ion batteries display worse reaction kinetics and inferior electrochemical properties than that in lithium-ion batteries due to the fact that the sodium ion is much bigger than lithium ion.

The rate performance of the CPAN/Se fiber and CPAN/Se powder electrodes is shown in Figure 8.11 (e) and (f). The CPAN/Se fiber electrodes also show good rate capability in both lithium-ion and sodium-ion batteries. The control sample CPAN/Se powders were synthesized through the same heat-treatment process as for CPAN/Se fibers, but based on a mixture of PAN and selenium powders. The CPAN/Se powders consist of round particles with diameter of 250 nm (Figure 8.16 and 8.17). At low rates, both CPAN/Se powder and fiber electrodes show similar rate performance, however, the CPAN/Se fibers exhibit superior rate performance at higher rates. In particular, the CPAN/Se fiber electrode can retain capacity of 290 mAh g^{-1} even at 3 C and recover to 600 mAh g^{-1} after the rate is returned to 0.1 C, but the CPAN/Se powders just deliver 180 mAh g^{-1}. The 1D fibrous nanostructure with smaller dimensions and large surface area can facilitate efficient contact between the active materials and the electrolyte, and provide more active sites for electrochemical reactions. In addition, the 1D architecture also possesses favourable structural stability, which can help to alleviate the structural damage caused by volume expansion and to keep the integrity of the electrodes during the charge-discharge process especially at high rate or after long-term cycling. All these characteristics result in such a good rate capabilities. For the Na-Se batteries, the capacity of the CPAN/Se fibers is decreased from 550 to 245 mAh g^{-1} with the increase of rate from 0.1 C to 3 C.

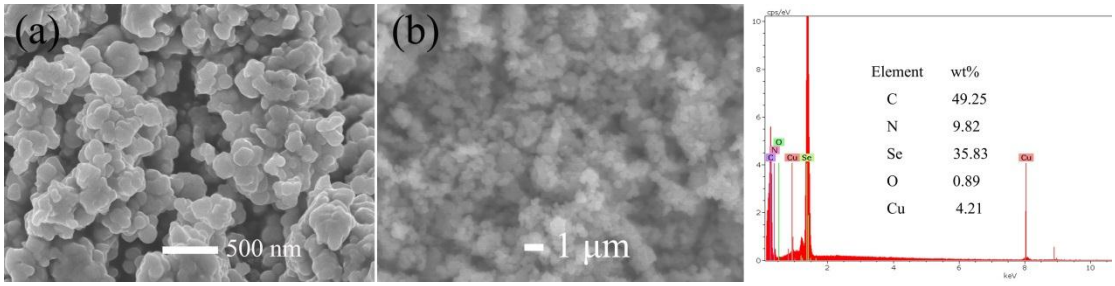

Figure 8.16 (a) SEM image of CPAN/Se powders, (b) elemental information obtained by EDX characterization for the entire area (21 × 16 μm^2) shown in (b). The detected Cu on the CPAN/Se powder sample is attributed to the copper substrate.

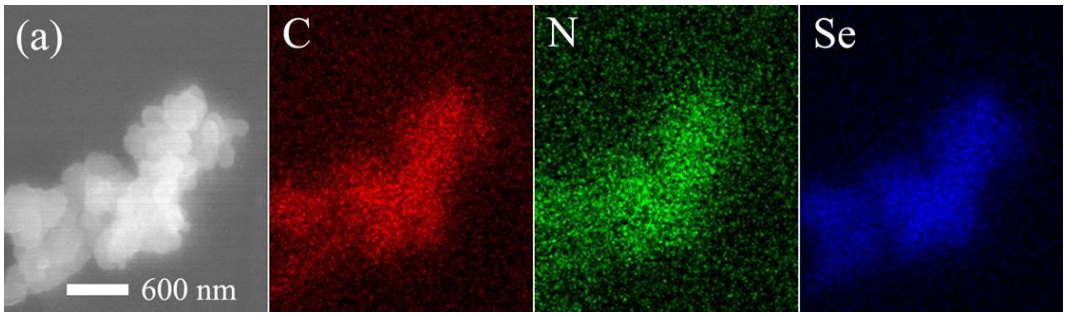

Figure 8.17 (a) SEM image of PAN/Se powders and the corresponding elemental map images of (b) carbon and (c) selenium.

To further investigate the reason why the CPAN/Se electrode shows such a superior electrochemical performance, the microstructure of the CPAN/Se fiber electrode after 100 cycles for Li-Se batteries was examined by SEM. The fibrous structure (Figure 8.18 (a)) is still maintained, and no obvious change is observed. The element mapping results (Figure 8.18 (b)) show that the selenium is still homogeneously distributed throughout the whole fiber, suggesting the excellent mechanical stability of the CPAN/Se fibers. Together with its unique chemical structure, excellent electrochemical properties of CPAN/Se can be achieved.

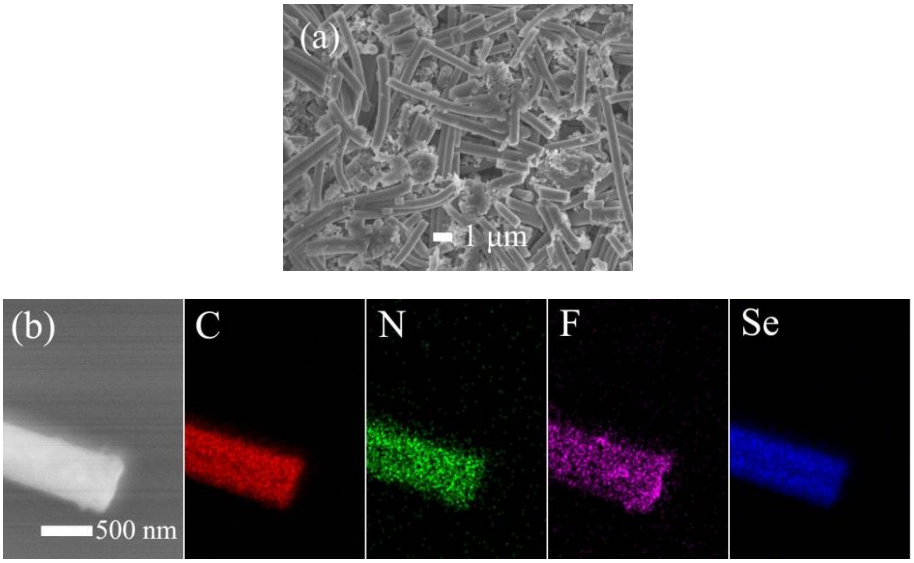

Figure 8.18 (a) SEM images of CPAN/Se fiberS after 100 cycles for Li-Se batteries, and (b) corresponding elemental map images of carbon, nitrogen, fluorine, and selenium. The detected fluorine is attributed to the electrolyte ($LiPF_6$).

8.4 Conclusion

In summary, a novel type of selenium fibers were simply prepared by electrospinning technique. Selenium exists in the carbonized PAN matrix in form of energy-storing selenium side chains. Such a unique chemical structure not only enhances the electrical conductivity, but also can confine selenium during the charge and discharge processes, leading to superior long-term cycling stability and good rate performance. The CPAN/Se electrodes could remain a reversible capacity of 600 mAh g^{-1} for 500 cycles in Li-Se battery and 410 mAh g^{-1} for 300 cycles in Na-Se battery. In addition, this novel material exhibits superior electrochemical performance and it can be easily achieved manufacturing process, which makes our Se-based electrode highly promising for practical energy storage.

8.5 References

[1] P. G. Bruce, S. A. Freunberger, L. J. Hardwick, J. M. Tarascon, Nature Materials, 11 (2012) 19-29.

[2] M. K. Song, Y. G. Zhang, E. J. Cairns, Nano Letters 13 (2013) 5891-5899.

[3]H. L. Wang, Y. Yang, Y. Y. Liang, J. T. Robinson, Y. G. Li, A. Jackson, Y. Cui, H. J. Dai, Nano letters, 11 (2011) 2644-2647.

[4] Y. J. Cui, A. Abouimrane, J. Lu, T. Bolin, Y. Ren, W. Weng, C. J. Sun, V. A. Maroni, S. M. Heald, K. Amine, Journal of the American Chemical Society, 135 (2013) 8047-8056

[5] A. Abouimrane, D. Dambournet, K. W. Chapman, P. J. Chupas, W. Weng, K. Amine, Journal of the American Chemical Society, 134 (2012) 4505-4508.

[6] C. P. Yang, S. Xin, Y. X. Yin, H. Ye, J. Zhang, Y. G. Guo, Angewandte Chemie International Edition, 52 (2013), 8363-8367.

[7] C. Luo, Y. H. Xu, Y. J. Zhu, Y. H. Liu, S.Y. Zheng, Y. Liu, A. Langrock, C. S. Wang, ACS Nano, 7 (2013) 8003-8010.

[8]L. L. Liu, Y. Y. Hou, X. W. Wu, S. Y. Xiao, Z. Chang, Y. Q. Yang, Y. P. Wu, Chemical Communications, 49 (2013) 11515-11517.

[9]L. L. Liu, Y. Y. Hou Y. Q. Yang, M. X. Li, X. W. Wang, Y. P. Wu, RSC Advances, 4 (2014) 9086-9091.

[10] S. F. Jiang, Z. A. Zhang, Y. Q. Lai, Y. H. Qu, X. W. Wang, J. Li, Journal of Power Sources, 267 (2014), 394-404.

[11] J. L.Wang, J. Yang, J. Y. Xie, N. X. Xu, Advanced Materials, 14 (2002) 963.

[12]J. L.Wang, J. Yang, C. R. Wan, K. Du, J. Y. Xie, N. X. Xu, Advanced Functional Materials, 13 (2003) 487.

[13]T. H. Hwang, D. S. Jung, J. S. Kim, B. G. Kim, J. W. Choi, Nano Letters, 13 (2013) 4532-4538.

[14]P. K. Babu, A. Lewera, J. H. Chung, R. Hunger, W. Jaegermann, N. Alonso-Vante, A. Wieckowski, E. Oldfield, Journal of the American Chemical Society, 129 (2007) 15140-15141.

[15]J. F. Moulder, W. F. Stickle, P. E. Sobol, K. D. Bomben, Handbook of X-ray photoelectron spectroscopy, ULVAC-PHI, Inc. Chigasaki, Japan 1995.

[16] X. G. Yu, J. J. Xie, Y. Li, H. J. Huang, C. Y. Lai, K. Wang, Journal of Power Sources, 146 (2005) 335-339.

[17]X. G. Yu, J. J. Xie, J. Yang, H. J. Huang, K. Wang, Z. S. Wen, Journal of Electroanalytical Chemistry, 573 (2004) 121-128.

[18]B. C. Duan, W. K. Wang, A. B. Wang, K. G. Yuan, Z. B. Yu, H. L. Zhao, J. Y. Qiu, Y. S. Yang, Journal of Materials Chemistry A, 1 (2013) 13261-13267.

[19]K. Helios, A. Pietraszko, W. Zierkiewicz, H. Wojtowicz, D. Michalska, Polyhedron, 30 (2011) 2466-2472.

[20]K. Grenader, M. Kind, L. Silies, A. Peters, J. W. Bats, M. Bolte, Journal of Molecular Structure, 1039 (2013) 61-70.

[21]X. W. Wang, Z, A, Zhang, Y. H. Qu, Y. Q. Lai, J. Li, Journal of Power Sources, 256 (2014) 361-368.

[22]J. Yang, J. Xie, X. Y, Zhou, Y. L. Zou, J. J. Tang, S. C. Wang, F. Chen, L. Y. Wang, The Journal of Physical Chemistry C, 118 (2014) 1800-1807.

9 CONCLUSIONS AND OUTLOOK

In this doctoral work, a series of nanostructured sulfur-based materials were synthesized and used for high-performance Li-S and Li-Se batteries, including TiO_2 coated three-dimensional hierarchically ordered porous sulfur composite, micro-macroporous carbon-sulfur composite derived from cotton, one-dimensional ordered mesoporous-carbon-fiber–sulphur composite synthesized via the electrospinning technique, a novel design for an integrated flexible sulfur cathode for Li-S batteries, as well as one-dimensional organic selenium-containing fibers for Li-Se batteries. The as-prepared cathode materials show excellent electrochemical performance (high specific capacity, good cycling and rate performance) due to the introduction of nanostructured carbon. The good electrochemical performance is attributed to enhanced electronic conductivity of electrodes, toleration of the volume expansion, and controllability of the polysulfide diffusion.

The effects of a TiO_2 coating layer on the electrochemical performance of 3D hierarchically ordered porous carbon-sulfur composite cathode were investigated. The 3D hierarchically ordered porous carbon was synthesized through an evaporation-induced coating and self-assembly method using foam as template. The surface TiO_2 coating layer on the carbon-sulfur composite could help to trap the dissolved polysulfides and enhance the strength of the entire electrode, which can lead to notably improved performance for the lithium-sulfur battery, especially over long cycling and at high rates. Furthermore, the 3D hierarchically ordered porous carbon slices can be mass produced in a simple way at low cost and could work as a

binder-free cathode without any current collector in lithium-sulfur batteries, which makes our S-based electrode highly promising for practical application in lithium-sulfur batteries.

Two kinds of nanostructured porous carbon, micro-macroporous carbon and one-dimensional ordered mesoporous carbon fiber, were used as the matrix for loading sulfur for lithium-sulfur batteries. The micro-macroporous carbon derived from cotton is prepared via a chemical activation method using potassium hydrate. The activated carbon exhibits a hierarchically porous microstructure and high specific surface area (989 m^2 g^{-1}). The micro-macroporous structure not only allows a large amount of sulfur (68%) to be infiltrated into the micropores of the host, but also has a strong trapping capability towards polysulfides. When evaluated as a cathode for lithium-sulfur batteries, the hierarchically porous carbon-sulfur composite electrode exhibits excellent cycling stability and good performance. The resulting composite electrode possesses a reversible capacity of 760 mAh g^{-1} after 200 cycles at current density of 0.2 C. Furthermore, one-dimensional ordered mesoporous carbon fibers have been synthesized via the electrospinning technique, using resol as the carbon source and triblock copolymer Pluronic F127 as the template. Sulfur is then encapsulated in these ordered mesoporous carbon fibers by a simple thermal treatment. The interwoven fibrous nanostructure has favourable mechanical stability and can provide an effective conductive network for sulfur and polysulfides during cycling. In addition, the ordered mesopores could effectively trap soluble polysulfide intermediates during charge-discharge processes. The resulting ordered

mesoporous-carbon-fiber-sulfur (OMCF-S) composite with 63% S exhibits high reversible capacity, good capacity retention, and enhanced rate capacity when used as cathode in rechargeable lithium-sulfur batteries. The resulting OMCF-S electrode maintains a stable discharge capacity of 690 mAh g^{-1} at 0.3 C, even after 300 cycles.

A novel type of integrated flexible sulfur cathode was successfully designed and prepared for the first time via the simple doctor blade technique. The cathode is composed of an integrated carbon/sulfur/carbon (CSC) sandwich structure on polypropylene separator. The integrated electrode not only exhibits excellent flexibility and high mechanical strength, but also exhibits excellent electrochemical performance. The top and bottom carbon layers of the sandwich-structured electrode not only work as double current collectors, which effectively improves the conductivity of the electrode, but also serve as good barriers to suppress the diffusion of polysulfides and buffer the volume expansion of the active materials, leading to suppression of the shuttle effect and low self-discharge behaviour. The CSC@separator cathode delivered a high reversible capacity of 730 mAh g^{-1} over 500 cycles, with capacity decay as small as 0.058% per cycle and a low self-discharge constant of 0.0293 per week.

One-dimensional organic selenium-containing fibers were prepared by heating polyacrylonitrile-selenium (PAN-Se) fibers at 600 ^{o}C and used as cathode material for lithium-selenium and sodium-selenium batteries. This organic selenium-based material has a unique chemical structure different from that of physically mixed selenium-carbon composite. In this material, the Se molecules are confined by

N-containing carbon ring structures in the form of energy-storing selenium side chains in the carbonized PAN (CPAN) matrix. This unique stable chemical structure with a conductive carbon skeleton connected to the selenium side chains and excellent mechanical stability can allow CPAN/Se composite cathodes to be charged and discharged in a low-cost carbonate-based electrolyte with excellent long cycling stability and quite good rate performance. The CPAN/Se electrodes could retain a reversible capacity of 600 mAh g^{-1} for 500 cycles in a lithium-selenium battery and 410 mAh g^{-1} for 300 cycles in a sodium-selenium battery.

Although significant improvement of lithium-sulfur batteries has been achieved on the laboratory in the past few years, there will still be a long way to go to realize the real application of lithium-sulfur batteries. The electrochemical performance of a lithium-sulfur battery is very sensitive to the size of the cell and aspects such as the sulfur content in the active material and the sulfur loading mass. In most previously published papers, the sulfur content in the composite was usually less than 60%, while the areal sulfur loading mass in our electrode is less than 2 mg cm^{-2}, which is far from reaching practical energy density. In the future, therefore, how to achieve a high sulfur loading and still retain the good electrochemical performance of the sulfur cathode is one of the most important research directions that could lead to a viable, practical lithium-sulfur battery. On the other hand, to date, there has been little research focus on industrially viable solutions to address the problems of lithium-sulfur batteries. The binder, as one of the most important components in lithium-sulfur batteries, plays a critical role in the electrode fabrication process, and it

also has a strong influence on the electrochemical performance of lithium-sulfur batteries. Therefore, if the most serious problems of lithium-sulfur batteries could be addressed through the choice of binder, the electrode preparation process and the whole battery set-up could still be kept simple, which would greatly promote the practical application of lithium-sulfur batteries. Finally, considering the safety problems of lithium-sulfur batteries, Li_2S cathode is more suitable than sulfur cathode for lithium-sulfur batteries, as it does not need metallic lithium as counter electrode. How to address the initial activation issue for micrometer-sized Li_2S is the key point for obtaining such lithium-sulfur batteries with superior electrochemical performance. The chemical synthesis method may be the best possible solution for realizing control of the particle size and morphology of the Li_2S active material.